UNIVERSITÀ DEGLI STUDI DI TORINO

PHD PROGRAMME

DEPARTMENT OF PHYSICS

PhD Programme in Physics – XXXVI cycle

# Development of nanodiamonds as radiosensitizing physical agents for brain tumor treatment

*Candidate:*

Veronica Varzi

*Supervisors:*

Prof. Federico Picollo, Dr. Simonetta Pazzaglia

*PhD Programme Coordinator:*

Prof. Paolo Olivero

Academic years 2020 – 2023

Veronica Varzi
e-mail 1: veronica.varzi@unito.it
e-mail 2: veronicavarzi@yahoo.it
phone: +39 347 7421919

*Be the best of whatever you are*

*If you can't be a pine on the top of the hill,*
*Be a scrub in the valley – but be*
*The best little scrub by the side of the rill;*
*Be a bush if you can't be a tree.*

*If you can't be a bush be a bit of the grass,*
*And some highway some happier make;*
*If you can't be a muskie then just be a bass–*
*But the liveliest bass in the lake!*

*We can't all be captains, we've got to be crew,*
*There's something for all of us here.*
*There's big work to do and there's lesser to do,*
*And the task we must do is the near.*

*If you can't be a highway then just be a trail,*
*If you can't be the sun be a star;*
*It isn't by size that you win or you fail–*
*Be the best of whatever you are.*

*Sii il meglio di qualunque cosa tu possa essere*

*Se non puoi essere un pino in cima alla collina,*
*sii una macchia nella valle, ma sii*
*la migliore, piccola macchia accanto al ruscello;*
*sii un cespuglio, se non puoi essere un albero.*

*Se non puoi essere un cespuglio, sii un filo d'erba,*
*e rendi più lieta la strada;*
*se non puoi essere un luccio, allora sii solo un pesce persico:*
*ma il persico più vivace del lago!*

*Non possiamo essere tutti capitani, dobbiamo essere anche un equipaggio,*
*c'è qualcosa per tutti noi qui,*
*ci sono grandi compiti da svolgere e ce ne sono anche di più piccoli,*
*e quello che devi svolgere tu è lì, vicino a te.*

*Se non puoi essere un'autostrada, sii solo un sentiero,*
*se non puoi essere il sole, sii una stella;*
*Non è grazie alle dimensioni che vincerai o perderai:*
*sii il meglio di qualunque cosa tu possa essere.*

*– Douglas Malloch –*

# Contents

# List of Figures

# List of Tables



# List of Acronyms

| | |
|---|---|
| APE | Amperometric Peak Analysis |
| ATCC | American Type Culture Collection |
| BP | Bandpass |
| BSA | Bovine serum albumin |
| CCD | Charge-coupled device |
| CVD | Chemical Vapor Deposition |
| DLS | Dynamic Light Scattering |
| DRIFT | Diffuse Reflectance Infrared Fourier-Transform |
| DSB | Double-strand break |
| ENEA | Italian National Agency for New Technologies, Energy and Sustainable Economic Development |
| EPR | Enhanced permeability and retention |
| FA | Fatty acids |
| FBS | Foetal bovine serum |
| FCC | Face-centred cubic |
| FSC | Forward scatter |
| GeV | Germanium-vacancy |
| HFRT | Hyper-fractionated regimens |
| HPHT | High Pressure High Temperature |

| | |
|---|---|
| HRP | Horseradish peroxidase |
| HTPA | 2-hydroxyterephthalic acid |
| H-NDs | Hydrogenated-nanodiamonds |
| IGRT | Image-guided RT |
| IQ | Intelligence Quotient |
| LINACs | Linear accelerators |
| MB | Medulloblastoma |
| MEM | Minimum Essential Medium |
| MFI | Median Fluorescence Intensity |
| MRI | Magnetic resonance imaging |
| MSY | Monocrystalline synthetic diamond |
| NDs | Nanodiamonds |
| NPs | Nanoparticles |
| NV | Nitrogen-vacancy |
| OX-NDs | Oxidized-nanodiamonds |
| PBS | Phosphate-buffered saline |
| PbV | Lead-vacancy |
| PCR | Polymerase chain reaction |
| PE | Plating efficiency |
| PVDF | Polyvinylidene fluoride |
| qPCR | Quantitative real-time PCR |
| RDX | Cyclotrimethyl-enetrinitramine |
| ROS | Reactive oxygen species |
| RT | Radiotherapy |
| SEM | Standard error of the mean |
| SiV | Silicon-vacancy |
| SnV | Tin-vacancy |
| SSB | Single-strand break |
| SSC | Side scatter |
| TBS | Tris-buffered saline |
| TEB | Biomedical Technologies |
| TNT | Trinitrotoluene |
| TPA | Terephthalic acid |
| ZPL | Zero Phonon Line |

# Preface

In the last decades, *nanomedicine* turned out as a promising research area and many micro- and nano-systems are under development aiming at biosensing, drug delivery, biolabeling and cancer treatment as radiosensitizers. In these frameworks, diamond is acquiring ever-increasing interest, due to its biocompatibility, a fundamental feature when dealing with biological systems, chemical inertness and possibility of controlling surface functionalization.

In particular, diamond nanocrystals (or nanodiamonds, NDs) are taken into great consideration in several fields due to their excellent chemical and physical features. From the biomedical-application point of view, NDs present low toxicity, together with applicability as fluorescent biomarkers, thanks to their optically active defects in the crystal lattice (e.g.: nitrogen-vacancy NV centers). Moreover, they allow simple surface modification and functionalization with specific biomolecules or drugs. For example, thermal treatments represent a powerful method to achieve the control of ND surface chemistry.

Among these thermal processes, hydrogenation is extremely important since hydrogenated-NDs (H-NDs) have recently emerged as promising radiosensitizing agents. Indeed, many nanoparticles are being increasingly studied to improve radiotherapy (RT) treatments and H-ND capability to enhance injuries on cancer cells, boosting the production of reactive oxygen species (ROS) and damaging in an irreversible way cellular DNA, was supposed. Special attention must also be given to oxidation treatments. Oxidized-NDs (OX-NDs) often constitutes the starting point for hydrogenation processes and investigating the effects of hydrogenation and oxidation on ND properties constitutes a key step towards their final application.

The main perspective of this work is the development and characterization of NDs as radiosensitizers. Due to its strong interdisciplinarity, this activity was carried out in the context of the Solid State Physics group of the University of Torino and in close collaboration with the Biomedical Technologies Laboratory of the Italian National Agency for New Technologies, Energy and Sustainable Economic Development (ENEA) Casaccia Research Centre in Roma.

More precisely, NDs differing for sizes and superficial modifications (H- and OX-NDs) were examined in terms of surface chemistry (Diffuse Reflectance Infrared Fourier-Transform spectroscopy) and their carbon phases and fluorescent NV centers were characterized (Raman and photoluminescence spectroscopies respectively), providing useful structural and optical information about the thermal processes performed. In addition, ND behaviour and dispersibility in solution was investigated (Dynamic Light Scattering analysis), to test their suitability for biological applications.

To study the ND radiosensitizing effect, some experiments irradiating ND solutions with X-ray photons (130 kVp) were implemented, observing the production of a specific ROS species, the hydroxyl radical (•OH), following water radiolysis. The analysis of these samples was carried out through spectrofluorimetric measurements, using a custom setup built up by the candidate, and a fluorescent probe for the detection of the •OH radicals, the terephthalic acid (TPA).

The evidences obtained with combined treatments of ND/TPA solutions with X-ray irradiation show that H-NDs increase the •OH quantity, with a dependence on ND size, while OX-NDs do not, highlighting the potentiality of H-NDs to improve RT.

Another objective of this study was to explore the influence of the chemical/physical properties of NDs on cellular radiosensitivity to combined treatments with radiation beams of different energies. DAOY, a human radioresistant medulloblastoma (MB) cell line was treated with differently

sized H- and OX-NDs, in various concentrations. To assess ND internalization and intracellular localization, fluorescence microscopy and micro-Raman maps were performed. Moreover, the ability of MB human tumor cells to internalise NDs was evaluated using flow cytometry with excitation and emission spectra characteristic of native NV centers present in NDs. Next, MB cells incubated NDs with different surface-terminations were irradiated with photons of different beam energies using an X-ray generator operated at 250 kVp or a $^{60}$Co γ-source (1.25 MeV). In order to build up survival curves through clonogenic cell-survival assay, increasing doses of photons (2 Gy, 5 Gy and 8 Gy) were delivered. Additionally, the candidate delved into the nature of ND-radiation biological interactions, examining the molecular mechanisms involved, such as DNA damage and apoptosis. The aim was to highlight how various chemical/physical features, including size, surface modifications, and concentration, influence the ND radiosensitizing properties and how, in turn, NDs can enhance the impact of RT on brain tumor cells.

Results show that ND characteristics are crucial in determining cell toxicity, with H-NDs decreasing either cellular viability when administered alone, or cell survival when combined with radiation, depending on ND size and concentration, while OX-NDs do not. Also, irradiation at high energy (γ-rays at 1.25 MeV), in combination with H-NDs, is more efficient in eliciting *in vitro* radiosensitisation when compared to irradiation at lower energy (X-rays at 250 kVp). Finally, the addressed molecular mechanisms of ND-induced radiosensitisation demonstrated that cell killing is mediated by the induction of Caspase-3-dependent apoptosis that is independent to DNA damage. Therefore, identifying the optimal combination of ND features and radiation energy has the potential to offer an encouraging therapeutic strategy for tackling radioresistant cancers using H-NDs in conjunction with high-energy radiation.

Specifically, the manuscript is organized as follows:

- Chapter 1 offers an introduction on the research field of the work, with some background information about the interaction of ionizing radiation with matter, causing damage to biological structures and exploited in RT to impair cancer cells. It discuss the need for radiosensitizing materials, describing the main chemical/physical properties of diamond and NDs, as well as the use of thermal treatments to modify ND surface moieties. The characteristics of H-NDs, determining their potentialities as radiosensitizers, are also depicted, with an overview on the leading goals of the research activity.
- Chapter 2 is dedicated to the description of the instrumentation employed both for modifying and characterizing the ND samples. Moreover, the experimental setup used for the measurement of ND impact on •OH radical production under X-ray irradiation, with the custom fluorometer, is shown. The measurement setups and facilities for the assessment of ND effects after *in vitro* irradiation are also illustrated.
- Chapter 3 includes an accurate report of the implemented processing techniques and presents the results obtained in the modification and characterization of ND samples. ND effects on •OH production and in *in vitro* experiments following irradiation are deeply explained.
- The Conclusions summarize the central findings of this work, together with an outline of possible advances, to be investigated in more detail in future research activity.
- The appendices show the outcomes of the activities that the candidate performed in parallel to the main thesis work (Appendix A: Nanodiamond quantum sensing revealing free radicals; Appendix B: Diamond biosensors for in vitro radiobiology; Appendix C: Combining diamond biosensors with Amperometric Peak Analysis (APE) code).

# 1 Introduction

Brain cancers represent a leading cause of death in Europe and are among the most difficult forms of cancer to treat. Above all, medulloblastoma (MB) is the most common malignant brain tumor in children, with a median age of 9 years, and a peak in incidence between the ages of 3 and 7. About 18% to 20% of childhood brain cancers are MB and the European annual incidence rate was 6.5 per million children [1]. Currently, multimodal treatments, consisting in the combination of the maximal safe surgical removal followed by chemo and radiation therapy, are the most effective strategy against MB, having significantly improved their outcome [2], but can also have devastating neurological consequences, with significant side effects in healthy tissues, including marked losses of Intelligence Quotient (IQ). In particular, radiotherapy (RT) is a medical treatment method that employs ionizing radiation to impair cancer cells by damaging their genetic material, i.e. DNA, and block their ability to divide and further proliferate. It is the main auxiliary treatment to specifically target and control the tumor volume and eventually kill cancer cells.

## 1.1 Radiotherapy, ionizing radiation and radiobiology

Nowadays, RT is generally prescribed as effective modality for curative or adjuvant purposes, to relieve patients from symptoms caused by cancer, depending on multiple factors, especially the tumor radiosensitivity [3, 4]. Roughly, half of all cancer patients undergo some form of RT during the course of their treatment [5].

The origins of RT date back to 1895 when the German physicist Wilhelm Röntgen discovered X-rays, which, within few months, were employed to treat a patient with breast cancer [3]. Since then, varied RT methodologies have been developed over the years, differing for the kind of ionizing radiation employed and to date, RT treatments are typically delivered through linear accelerators (LINACs) [6], like the one displayed in Figure 1.

*Figure 1. Example of medical LINAC employed for RT treatments.*

Conventional RT relies on photon radiation (X-rays and γ-rays) or electrons, whereas particle radiation including protons, α or β particles, carbon ions or neutron beams constitute the basis of hadrontherapy [7, 8, 9]. RT and hadrontherapy physical basis are founded on processes of interaction between ionizing radiation and matter.

Every kind of radiation, passing through a material and interacting with it, releases energy to the atomic structure of the medium itself. If the amount of energy is sufficient to produce the ionization of the medium, it can be defined ionizing radiation. Focusing on the radiation type used for the experiments in

the context of the research activity of this thesis, photon beams will be considered in the following for the discussion.

### 1.1.1 Interaction of photon radiation with matter

Most RT clinical applications involve the use of photons [10] and the electromagnetic radiation mainly used in the biomedical field are X- and γ-rays. X-rays are generally obtained by braking radiation (Bremsstrahlung) and are lower in energy (100 eV - 100 keV) than γ-rays (energies > 100 keV) [11]. The latter refers to photons emitted by atomic nuclei or resulting from the annihilation of particles [12].

The main photon interaction processes with matter strongly depend on the energy of the incident beam, as well as from the properties of the crossed medium, and in particular its atomic number ($Z$). In the energy range generally employed in RT, i.e., ~ 100 keV - 25 MeV [10], the most probable interaction mechanisms between photons and matter to be considered are two different ones (Figure 2): the photoelectric effect and the Compton effect.

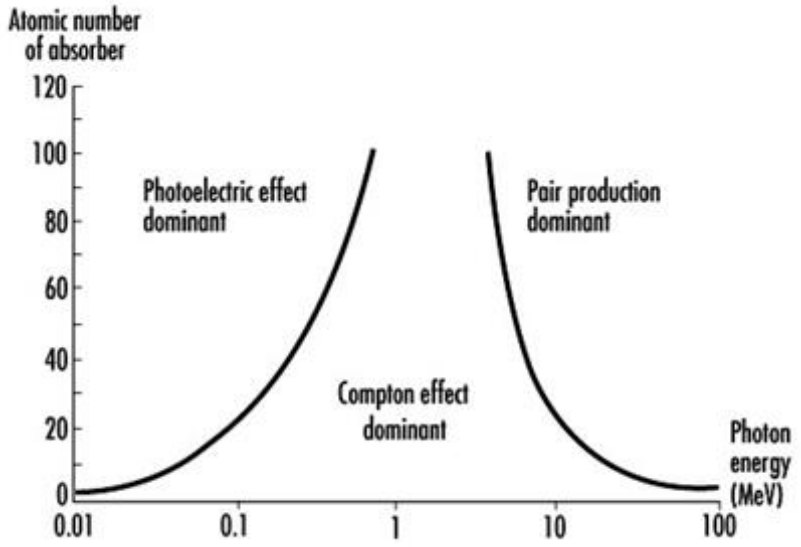


*Figure 2. Relative importance of the photon fundamental interaction processes. The solid lines show the atomic number (Z) of absorber and energy values hence the two types of effects are the same [13].*

- The photoelectric effect is the dominant interaction for low energy photons, in the keV range, while it becomes negligible from energies of 1 MeV. In this process, a photon leaves all its energy to a bound atomic electron in the K, L, … shell. Part of the transferred energy acts to overcome the binding energy of the electron ($E_b$) and releases it from the atom, while the residual photon energy contributes to the kinetic energy of the emitted electron ($E_k$), which is defined by:

$$E_k = E_\gamma - E_b$$

where $E_\gamma$ is the energy of the incident photon ($E_\gamma = hv$). The hole created by the dislodged orbital electron can be filled by an outer shell electron with the emission of characteristic X-rays or ejection of an Auger electron [14, 15]. The qualitative trend of the photoelectric cross section is described by:

$$\sigma_{ph}(E_\gamma) \propto \frac{Z^m}{(E_\gamma)^n}$$

where the exponent $m$ ranges from 4 ($E_\gamma$ below 100 keV) to 4.6 ($E_\gamma$ above 500 keV) and the exponent $n$ ranges from 3 ($E_\gamma$ < 100 keV) to 1 ($E_\gamma$ > 500 keV) [16].

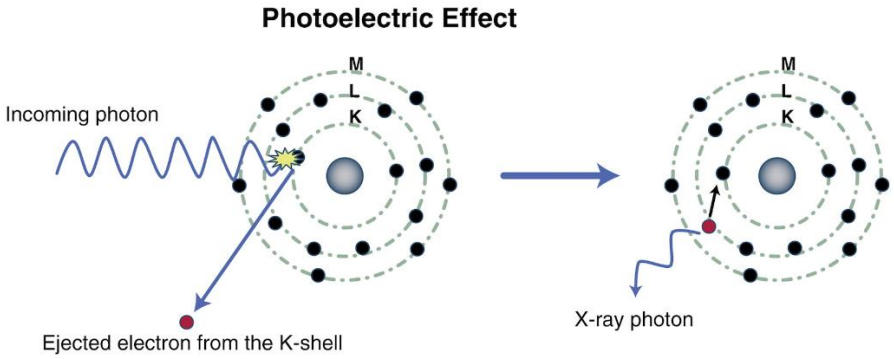


*Figure 3. Illustration of photoelectric effect and its consequences [17].*

- The Compton effect prevails for higher energy photons (MeV range) and consists in an elastic scattering process, with the partial energy transfer of the incident photon to an outer orbital electron. The electron and the scattered photon can then undergo further interactions, causing more ionizations, until their energy is dissipated [15]. Following the interaction, the kinetic energy of the electron is:

$$E_k = E_\gamma - E_\gamma{}'$$

where $E_\gamma{}'$ is the energy of the photon after the interaction. The trend of the Compton cross section is [18]:

$$\sigma_C \propto Z$$

Therefore, the probability of both photoelectric and Compton effect depend on the atomic number ($Z$) of the absorber [15, 19].

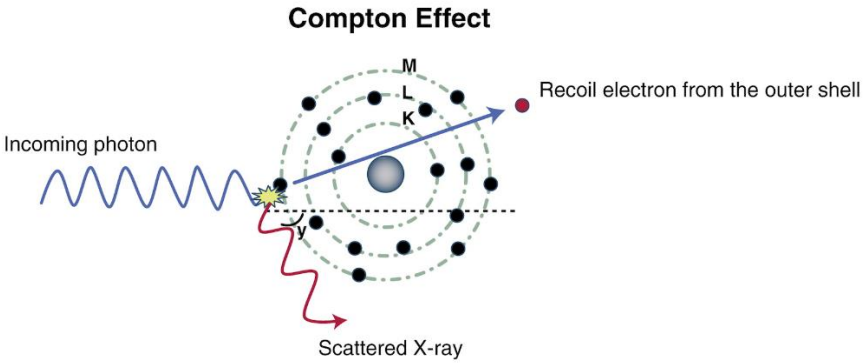


*Figure 4. Illustration of Compton effect [17].*

However, to fully define the interaction phenomena between ionizing radiation and living matter, it is necessary to consider not only the physical characteristics just listed, but also the biological ones. Precisely, the discipline that deals with the study of these aspects is radiobiology, better outlined in the next paragraph.

### 1.1.2 Radiation biological effects

RT biological basis are centred on the damage caused by ionizing radiation following interactions with living matter and in particular with cells. The average amount of energy released by ionizing radiation per unit mass of the interacting medium is the *absorbed dose* or *dose* ($D$), defined by the following equation:

$$D = \frac{d\varepsilon}{dm}$$

where $d\varepsilon$ is the mean energy imparted to matter of mass $dm$. $D$ is measured in $Joule\ per\ kilogram\ (J\ kg^{-1})$, usually referred to as $Gray\ (Gy)$ [20].

The physical, chemical and biological processes that occur after the ionizing radiation-cell interaction are extremely complex and differentiated, depending on the characteristics of radiation, the radiation dose, cell type and the phase of the cell cycle in which the single irradiated cell is found [21]. Following the interaction, radiation can provoke two fundamental types of damages: a direct or indirect biological effect [22], schematized in Figure 5.

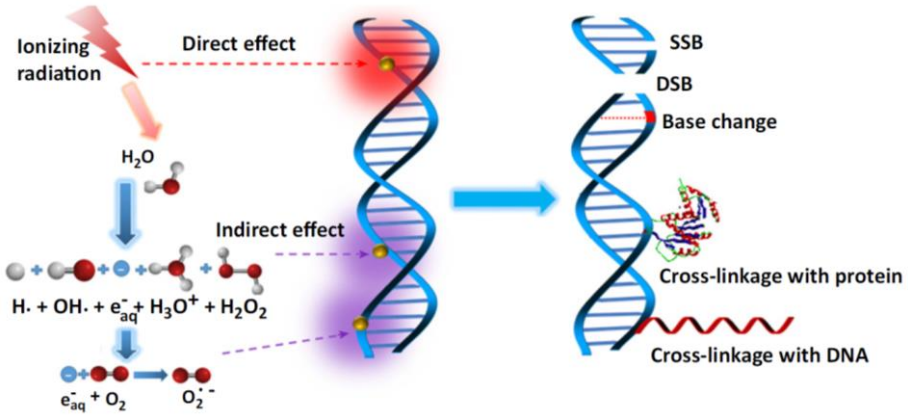


*Figure 5. Schematic representation of the action mechanism of ionizing radiation on DNA. Radiation can directly damage DNA (direct effect) or cleaves water molecules to generate reactive oxygen species (ROS), attacking DNA (indirect effect). Several types of DNA injuries can occur, such as single-strand break (SSB), double-strand break (DSB), nitrogen bases changes and cross-linkages with proteins or other DNA molecules [23].*

In the case of direct biological effect, radiation directly ionizes the macro-biological molecules, such as proteins, lipids and DNA, starting a chain of events that leads to a biological change in the cell metabolism. Instead, concerning the indirect effect, radiation interacts with other atoms or molecules present in the cellular environment, with the formation of new chemical species. This is the main case of the radiolysis of water molecules (constituting 70% - 80% of the cell volume) that trigger radical species production, frequently called free radicals. This term denotes an atom or group of atoms containing an unpaired electron, resulting in a strong chemical reactivity. Free radicals can interact with critical targets and produce chemical modifications and consequent harmful effects to the cells [10]. In more detail, in the indirect effect, the large part of free radicals involved in water radiolysis are the reactive oxygen species (ROS).

ROS have unpaired electrons that can injure biomolecules by chemical reactions, such as hydrogen extraction, addition, disproportionation, and electron capture. In particular, if highly concentrated, ROS can induce various deleterious effects, by inducing cellular stress, dysfunctions and ultimately altering cellular signalling or activating apoptotic pathways [24, 25, 26]. The main ROS are shown with their electronic structure in Figure 6.

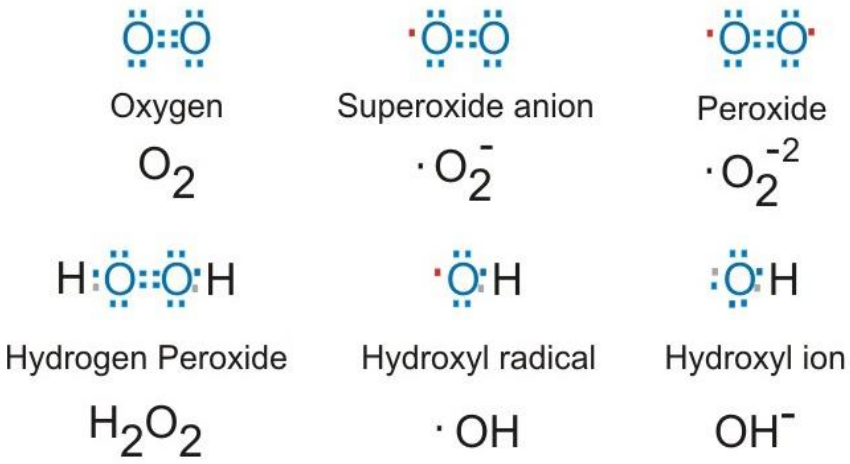


*Figure 6. Main types of ROS.*

From the biological point of view, the hydroxyl radical (•OH) is particularly relevant since it is extremely reactive and is considered the most damaging radical species [10], because it is a very dangerous compound to the organism, that cannot be eliminated by an enzymatic reaction. Approximately two thirds of the damages caused by the interaction between X-rays and mammalian cells, are caused by functional modifications of biologically fundamental macromolecules, caused by the •OH radical [22].

In both direct and indirect effect, various cellular components are damaged. The main one inside cells is DNA, the molecule that collects genetic information and allows protein synthesis [22]. If DNA modifications are not repaired appropriately by specific cellular mechanisms, they can cause multiple changes in cellular functionality or even lead to cell death [27]. Structural damages to DNA can be single-strand breaks (SSBs) or double-strand breaks (DSBs), nitrogen base damage and cross-linking DNA-protein or DNA-DNA (formation of covalent bonds with a protein or with another DNA molecule). These lesions may result in the termination of cell division and proliferation, or even induce necrosis or apoptosis [10, 23].

Concerning clinical application of RT, its efficacy is closely related to the dose of radiation: a higher dose means more adverse effects on tumor tissues, but also more possible lesions on the surrounding healthy tissues. In fact, RT is not a selective antitumor treatment and radiation is harmful to cancer and healthy cells alike, since direct and indirect biological mechanisms act on both without distinction.

In the RT treatments prescribed for the cure of MB, the conventional doses delivered to the craniospinal axis and to the posterior fossa are 54 Gy - 56 Gy. Using such doses detrimental side effects in healthy tissues in proximity of the treated volume are inevitable and a high proportion of MB survivors have significant long-term consequences, including marked losses of IQ and endocrine dysfunction [28]. In addition, risks of RT include the incomplete eradication of tumors and cancer recurrence. In this context, RT still needs

caution. The main challenge for radiation oncologists, medical physicists and radiobiologists is to enhance RT therapeutic efficacy, delivering the maximum dose to tumor cells and minimizing the exposure of the healthy tissues in proximity of the treated volume.

In MB treatment, many attempts have been made to control tumor growth, while trying to reduce the radiation-related neurocognitive effects, especially devastating in paediatric patients. For example, brachytherapy [29, 30], intensity-modulated RT [31, 32, 33], image-guided RT (IGRT) [34, 35], and stereotactic RT [36, 37] are employed. Besides, fractionated regimens serve to strengthen the therapeutic effects [38, 39, 40]. Indeed, advances in RT involve hyper-fractionated regimens (HFRT), consisting of smaller doses per fraction, with fractions administered at least twice each day. Using HFRT, the late-reacting tissues (assumed for the central nervous system) are predominantly spared compared to effects in early reacting tissues (such as mucosa, bone marrow) and tumors [41]. Recent strategies in paediatric oncology included also the use of 3D conformal RT as well as proton therapy to minimize late effects in MB patients, with clinically relevant differences compared to photon radiation treatments [42, 43]. However, although proton therapy has led to a decrease in treatments sequelae, due to its preferable dose deposition course (Bragg peak) and better tumor targeting, it still remains a demanding and quite expensive irradiation technique, in a preliminary phase of development and not easily accessible.

One alternative think proposed to overcome these obstacles is to deliver a lower radiation dose to the tumor, minimizing the injuries on normal cells. A strategy that aims this goal is the introduction of radiosensitizing agents, i.e., molecules, or more in general materials, capable to amplify the radiosensitivity of tumor cells. This approach can represent an encouraging line to achieve the main optimization of RT treatment, working both on making cancer cells more sensitive to radiations and preventing long-term morbidity by reducing the radiation dose on normal tissues [23]. These

radiosensitizers are usually constituted by macromolecules or nanomaterials [19, 23] and for the purposes of this work the discussion will be focused on the latter, more deeply described in the next paragraph.

## 1.2 Nano-radiosensitizers

The radiosensitizing materials can work selectively, when combined with radiation, as an encouraging approach to improve RT efficacy, allowing a lower dose delivery to the tumor targets, sparing the surrounding tissue. With the significant and continuous technological innovation, more and more materials have been defined as nano-radiosensitizers and a new impacting development direction for radiation oncology is the *nanomedicine*, which has become an important field of research of modern medical treatment and that is briefly introduced in paragraph 1.2.1.

Radiosensitizers can be classified into three major categories according to their different structures. They includes small molecules, macromolecules and nanomaterials [23]. Focusing the attention to the latter group, for the benefit of the subsequent discussion, nanomaterials have at least one dimension in the nanoscale, i.e., the size range from 1 nm to 100 nm [44, 45]. Based on the size of *x*, *y* and *z* dimensions, nanomaterials are classified as follows [46].

- Zero-dimensional: all three dimensions have nanoscale size. Nanoparticles and nanospheres belong to this group.
- One-dimensional: two dimensions are in the nanoscale range, whereas the remaining one is not. This class encompasses nanorods, nanotubes and nanowires.
- Two-dimensional: they expand in two dimensions, with the third one maintaining a nanoscale size. Nanofilms, nanolayers, and nano-coatings are related to this group.

- Three-dimensional or bulk nanomaterials: they conserve nanoscale size in their building blocks, while are not confined to the nanoscale in any dimension. They include bundles of nanowires or nanotubes, multi-nanolayers.

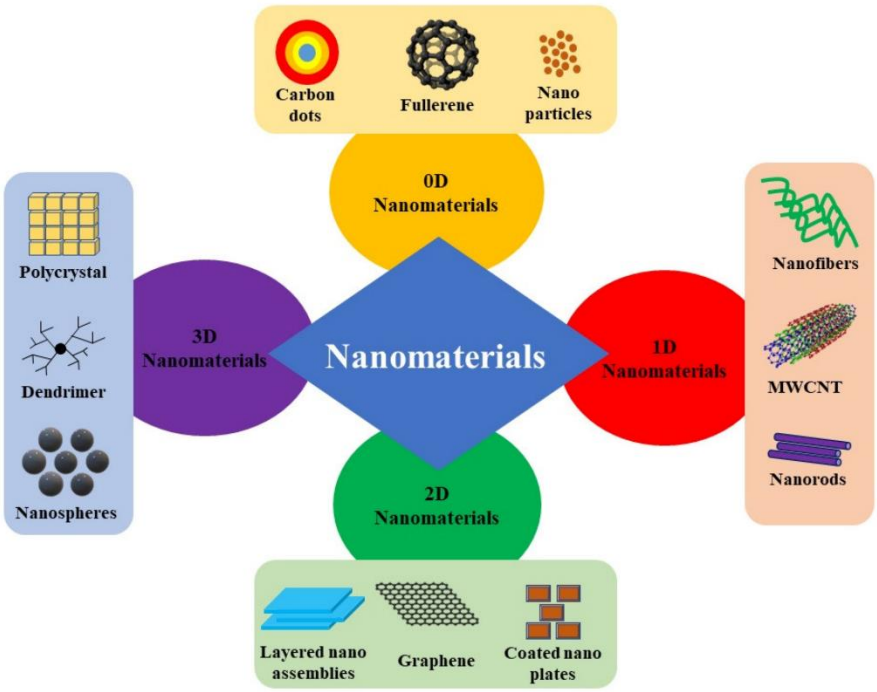


*Figure 7. Classification of nanomaterials according to their dimensionality [47].*

### 1.2.1 Nanomedicine

Nanomedicine is an ever-growing research area that deals with the medical application of nanotechnology and the exploitation of nanostructured materials [48]. Over the years, nanomedicine was extremely proactive in the biomedical field due to the typical size of the cells at the basis of living beings (1 μm - 10 μm, i.e. 2 - 3 orders of magnitude larger than the typical dimensions of nanomaterials). Indeed, this discipline allows investigating and acting at cellular level, without significantly disrupting the biological system.

The applications of healthcare span across various fields including drug delivery [49, 50], bioimaging [51, 52], tissue engineering [53], biosensors [54], surgery, cancer diagnosis and therapy [55]. Interestingly, the strong interdisciplinary nature of nanomedicine requires the integration of multiple scientific areas, such as physics, chemistry, biology, materials science, computer science and engineering. In this context, an increasing number of nanodrugs are under clinical translation, representing an opportunity to achieve sophisticated targeting strategies and multifunctionality. Indeed, nanoscale materials provide unique chemical and physical properties and are well suited to various biomedical applications, as for example radiosensitizing purposes [56, 57].

Among nanomaterials, the most investigated nanostructures are nanoparticles (NPs). For example, using different types of NPs such as metal-NPs [58, 59, 60], semiconductor quantum dots [61, 62, 63], and polymers [64, 65, 66], several studies have already demonstrated NP potential in clinical diagnostics and treatments [67, 68, 69, 70, 71, 72].

At the state of art, there are many NPs used in medicine, by virtue of their peculiar chemical and physical properties, in particular, their size ranging from a few nanometers up to 100 nm - 200 nm and their easier deliver to the tumor environment. Figure 8 shows a variety of NPs usable in nanomedicine:

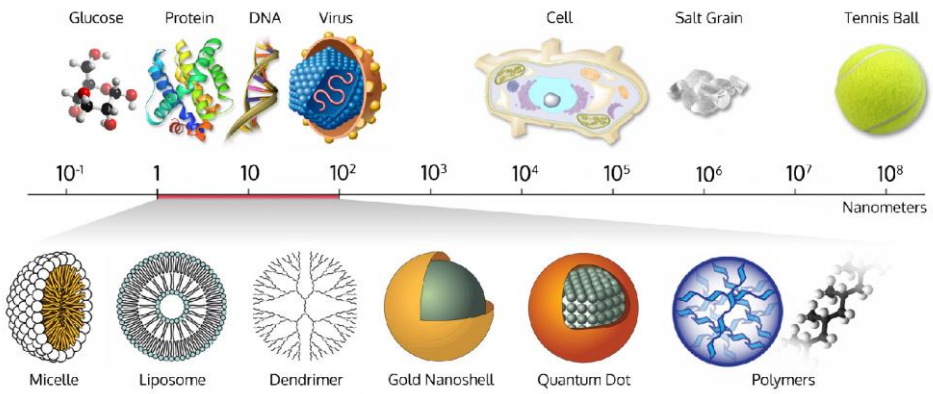


*Figure 8. Size, scale and variety of NPs potentially used in nanomedicine compared to the dimensions of biological systems [73].*

According to their purpose, NPs can be engineered to meet specific requirements (selectivity, size, shape, biocompatibility, etc.). Moreover, in oncology, the advantage of nano-sized therapeutic agents is their prolonged circulation period in the bloodstream, which allow a more efficient reaching of the target. Once inside the cancer cell, NPs accumulate within the tumor, thanks to the enhanced permeability and retention (EPR) effect [56]. In particular, an innovative, effective and, at the same time, safe approach for improving RT treatment consists of the radiosensitisation of cancer cells by means of NPs.

Over the last decades, many research programs dealt with *in vitro* and *in vivo* applications of NPs as radiosensitizers [74]. The goal of combining NPs with RT is to enhance the differential effect between healthy and tumor tissues. Due to the centrality of the topic in the context of this thesis, the next section is dedicated to the employment of NPs as nano-radiosensitizers.

### 1.2.2 Nanoparticles as radiosensitizers

In recent decades, the radiosensitizing effects of numerous NP types have been well characterized and there has been a large increase in the number of applications of NPs with the scope to optimise RT treatments. The underlying principle is to induce highly deleterious DNA lesions in cancer cells [75], following the interaction of ionizing radiation with NPs, with consequent boosting of the direct and indirect effects [19, 23] (Figure 9).

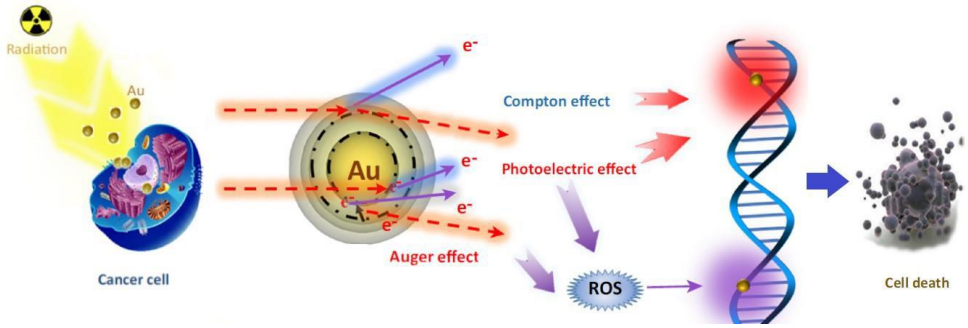


*Figure 9. Hypothesis of the radiosensitizing mechanism of NPs (e.g.: Au). Secondary electrons from photoelectric and Compton effect lead to DNA damage via direct and indirect processes [23].*

More in detail, the incident photon beam interacts with the constituent atoms of NPs embedded in biological tissue. The physical processes involved in the interactions of photons with matter (described in 1.1.1) can then result in the copious release of secondary particles in nanoscale volumes, following primary ionization and excitation events [76]. Provided they are emitted in a dense medium (NPs or biosystem), these particles with energies ranging from few eV (Auger electrons) to MeV (delta electrons) may successively ionise surrounding biomolecules as well as neighbouring nanoparticles. NPs can thus intensify the production of secondary electrons and free radicals, like ROS, which are highly reactive chemical species and this cascade can result in the enhancement of the radiation-induced impairment [74].

In the context of RT, mainly high atomic number ($Z$) NPs have attracted interest for their capacity to increase radiation damage effects and in particular metal-NPs, including above all gold, but also silver and platinum [19, 77]. Indeed, the introduction of high-$Z$ NPs into a tumor offers the peculiar possibility of amplifying ionization events in the medium, primarily thanks to the dependence of the cross-section from $Z$ (see section 1.1.1). Furthermore, the local dose enhancement via photoelectric effect or Compton scattering [19, 23] can promote the formation of ROS, potentially responsible for highly deleterious DNA filament lesions. These indirect damages can in turn cause cell death and enhance RT effects [74, 75].

However, even if several *in vitro* and *in vivo* experiments provided evidence for the effectiveness of radio-enhancement by metal-NPs [19] and the vast majority of studies to date have focused on gold-NPs, some studies also showed their unsuitable for clinical use because of their cytotoxicity and the reduction of cell viability [78]. To cite few of the most representative, Goodman *et al.* observed the toxicity of gold-NPs functionalized with cationic and anionic side chains [79], while Stefan *et al.* registered an increase of the liver-to-body ratio and a decrease of brain-to-body ratio in rats injected with chitosan-capped gold-NPs, suggesting possible liver toxicity and brain damage [80]. Therefore, while the vast majority of studies have focused on metal- and most of all gold-NPs of different sizes, shapes and surface coatings, the research of NPs that exhibit safe behaviour after cellular uptake is of paramount importance.

An increasing number of works are exploring opportunities offered by other NPs, like gadolinium-, platinum-, iron oxide-, hafnium- and carbon-based ones [19]. For example, molecular scale studies highlighted the radiosensitizing properties of platinum-NPs [81, 82]. Whereas, radio-enhancement by hafnium oxide-NPs has been demonstrated by Maggiorella *et al.* [83]: *in vitro* studies were performed with human fibrosarcoma HT1080 cells used as models to investigate the radiosensitizing effects of these NPs combined with γ-rays.

Lastly, among the most promising alternative strategies to high-*Z* metal-NPs, several *in vitro* [84] and *in vivo* [85, 86] studies have shown that carbon-NPs are non-cytotoxic and well tolerated [87]. Specifically, among the possible materials employed to further improve the efficacy of RT, diamond nanocrystals or nanodiamonds (NDs) were highlighted as a new class of carbon-NPs really promising in assisting RT *in vitro* [75]. For example, Grall *et al.* [87] explored the capacity of these versatile and promising nanotools to enhance radiation effects (γ-rays from $^{137}Cs$) and ROS production in different radioresistant cancer cell lines.

## 1.3 Nanodiamonds

Among the wide variety of materials under investigation for nanomedicine purposes, artificial diamond is emerging as one of the most appealing. Many studies highlighted its excellent biocompatibility [84, 88], which is an essential feature to interface with biological systems. In addition, its chemical inertness avoids interactions with the culture medium and the presence of photoluminescent defects (see paragraph 1.3.4) allow its traceability in the cellular environment, making diamond appreciable also for quantum sensing purposes [89, 90, 91, 92, 93, 94]. NDs present also highly tailorable and fully accessible surface functionalisation capabilities and can be produced cost-effectively in large quantities, with dimensions spanning from single digit nanometers (4 nm - 5 nm) to several hundred nanometers (300 nm), which are suitable for nanoscale applications.

Based on these appealing physical, chemical and optical properties, in the last years the Solid State Physics research group of the University of Torino, among which this thesis work was carried out, started to investigate NDs for applications in the biomedical field. Due to the centrality in this thesis, the properties of NDs and of diamond in general are described in the next paragraphs.

### 1.3.1 Physical and chemical properties of diamond

Diamond (from Greek αδαμας, adamas: "indestructible") is one of the allotropic forms of carbon. In the periodic table, this element belongs to the second period, group IV, being a non-metal with ground-state electronic configuration [He] $2s^2 2p^2$. The wide variety of carbon allotropes (among which amorphous carbon, graphite, and diamond) differ in the way atoms bond together and arrange themselves into a structure by adopting different hybrid configurations.

In diamond, each carbon atom present $sp^3$ hybridized orbitals and is bounded with strong covalent bonds to the four adjacent atom placed at the corners of a regular tetrahedron (Figure 10). Diamond crystalline structure is highly isotropic and organized in a cubic centered-face lattice (FCC) with a lattice constant equal to 3.57 Å [95]. Thanks to its atomic configuration, diamond possesses an extremely high value of gravimetric density $\rho = 3.54$ g $cm^{-3}$ [96].

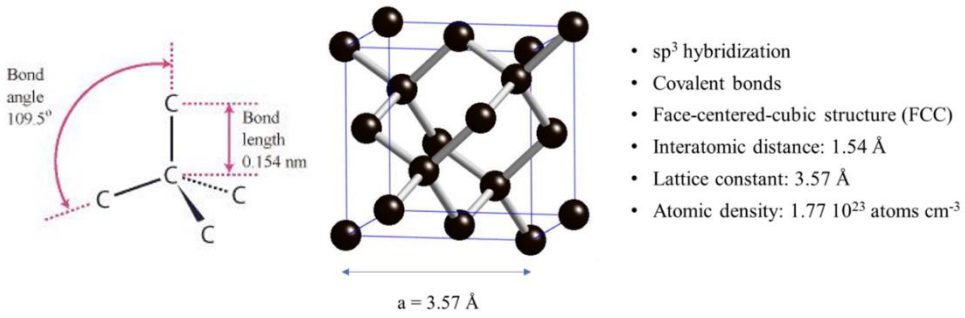


*Figure 10. Single-tetrahedron and face-centred cubic (FCC) lattice cell of diamond (the figure was adapted from [97] and [98] and is not in scale).*

Instead, concerning for example another allotropic form of carbon, graphite is based on carbon $sp^2$ hybridization. Its structure consists of stacked carbon layers, each of them composed of a hexagonal network of atoms connected by a covalent bond. The layers are maintained in position by weak Van der Waals forces [95] (Figure 11).

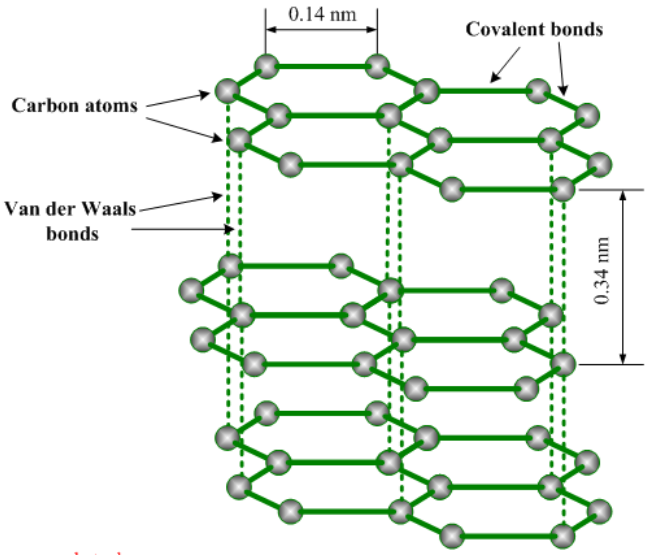


*Figure 11. Graphite structure [99].*

Focusing on diamond, it is a "metastable" form and is synthetized only at high pressures and temperatures (above 10 GPa and 2000 K). This peculiarity makes it kinetically stable even at room temperature and atmospheric pressure [95], as it is possible to observe in the carbon phase diagram, reported in Figure 12.

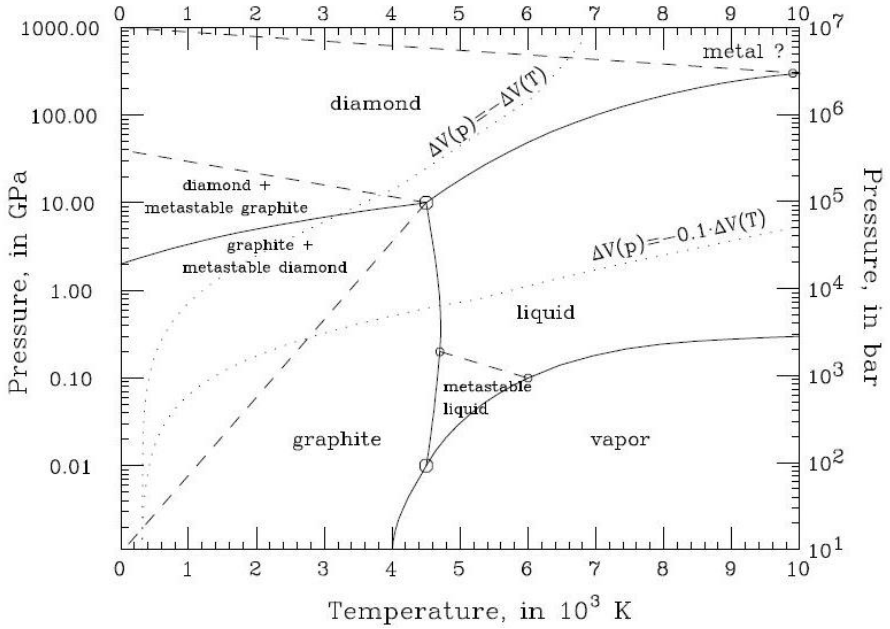


*Figure 12. Carbon phase diagram [100].*

The diamond interatomic cohesion energy is very strong (7.37 eV $atom^{-1}$) [95] and a large amount of energy is required to remove a carbon atom from the diamond lattice. This feature is at the basis of several extreme and outstanding macroscopic properties that give diamond many advantages compared with other materials, including:

- an extreme hardness value (10 on the Mohs scale [101]), the maximum found in nature;
- high Young's modulus equal to 1220 GPa [95];
- a really low linear thermal expansion coefficient ($0.8 \cdot 10^{-6}$ $K^{-1}$), whereas its thermal conductivity (2200 W $m^{-1}$ $K^{-1}$), is the greatest of any solid [95];
- a high refractive index, of about 2.42 over the visible spectrum. Moreover, it shows transparency over a broad spectral range of wavelengths, from the near ultraviolet to the far infrared [102];
- a wide band gap (energy gap $E_g$ = 5.47 eV [103]), rendering the un-doped material one of the best electrical insulators, with resistivity equal to $10^{16}$ Ω cm;
- high chemical inertia and excellent biocompatibility, key features when working with biological systems [88].

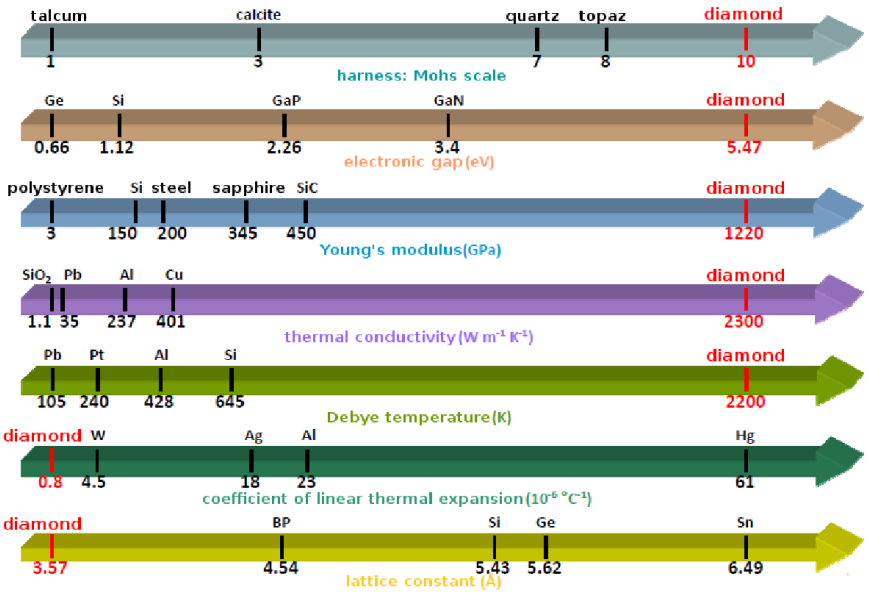


*Figure 13. Physical and chemical properties of various elements: diamond extreme peculiarities are highlighted in red.*

Moreover, diamond can accommodate a high number of defects in its lattice and nowadays more than 500 different color centers are known in diamond, many of which are artificially made through ion implantation processes [104].

### 1.3.2 Classification of diamond

Both natural and synthetic diamonds always contain impurities, with the most common being nitrogen and boron, the neighbours of carbon in the periodic table. Depending on the nature and the quantity of these impurities, diamond can be classified into four categories [95].

- Type Ia: characterized by a high and variable nitrogen content (100 ppm - 1000 ppm, as aggregates). It presents a strong optical absorption below 300 nm, hence appearing colourless. It is widely employed for applications that take advantage of the high hardness or in jewellery. Most of natural diamonds fall in this category (~ 98%), while only in rare cases they can be found in the other categories.

- Type Ib: nitrogen concentration between 100 ppm - 500 ppm (in the form of structurally isolated atoms). The light absorption window falls at longer wavelength with respect to type Ia, in the green and blue range (i.e., 400 nm), making it to appear yellowish.
- Type IIa: very low nitrogen concentration (less than 10 ppm), making up only the 2% of natural diamond and offering optical transparency with transmittance spanning from 225 nm to 2000 nm.
- Type IIb: nitrogen concentrations even lower than type IIa. In this frame, the presence of boron impurities become relevant, providing p-type semiconductor behavior.

In the context of this thesis, the project work always employed artificially synthesized NDs of type Ib. Compared to natural diamonds, characterized by prohibitive costs and variability and scarcity of samples (as better explained in section 1.3.3), they present accessible costs with the preservation of the physical properties.

### 1.3.3 Synthesis of nanodiamonds

The term “nanodiamond” usually refers to diamond crystals in the nanoscale range. Diamond can be either of natural or synthetic origin. Natural diamond represents one of the most sought-after gemstones and is created under extreme conditions due to geological processes at more than 150 km in the mantle of the earth [96]. However, due to the scarcity, poorly standardizable characteristics and the considerable cost of natural diamond, it is unsuitable for scientific and industrial applications. Therefore, in the last century different artificial synthesis techniques have been developed to allow systematic reproducibility under controlled conditions. The most widespread methods to produce artificial NDs are summarized below.

- Detonation: NDs are synthesized in sealed chambers filled with an inert gas or ice coolant, by inducing a controlled explosion of carbon-containing compounds, including trinitrotoluene (TNT) and

cyclotrimethyl-enetrinitramine (RDX) mixtures. The high pressures and temperatures reached on the detonation wavefront permits the synthesis of NDs [105]. This gives rise to particles having a considerable amount of graphitic carbon on the surface and containing a high number of impurities and defects.

- Monocrystalline diamond fragmentation synthesized using High Pressure High Temperature (HPHT) method [106]: in this process graphite is subjected to the conditions of natural diamond formation (around 10 GPa of pressure and average temperatures of 2000 K - 3000 K), determining its conversion to diamond, which is the stable energy-favorite allotropic form of carbon in this regimen [96]. These are more pure and less defective particles compared to detonation NDs [107].
- Chemical Vapor Deposition (CVD), also known as Low Pressure Low Temperature synthesis: diamond is grown through the slow deposition of atomic layers on a low-quality single-crystal diamond substrate at pressure of 2500 Pa and a quite reduced temperature of about 930 °C. The process occurs in a controlled atmosphere containing hydrocarbons, typically ethylene or methane, which provides the carbon atoms for the deposition, while other gases, such as nitrogen and boron, can be introduced to create specific color centers. The main advantage of this technique is the possibility of accurately controlling the size and the concentration of impurities with short time of growth [96, 108].

As a side effect, due to the high stresses that occur during the synthesis processes, NDs present an onion-like structure [107] (Figure 14).

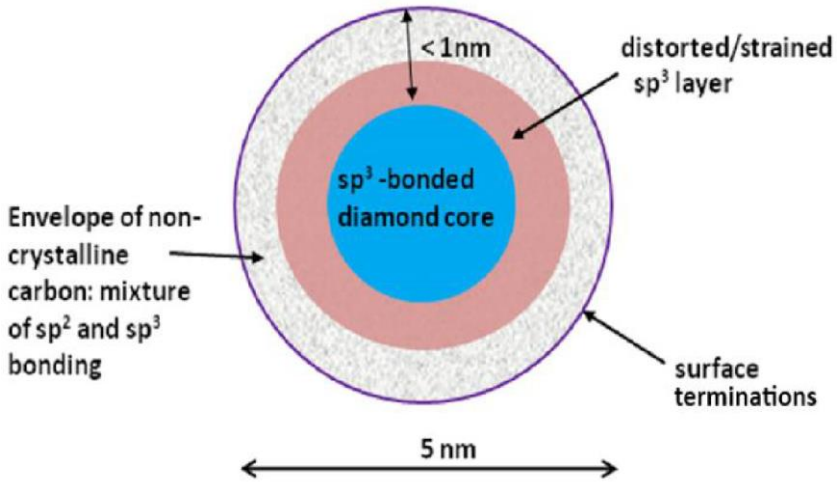


*Figure 14. Simplified core-shell architecture of a ND [109].*

In particular, they are characterized by:

- a diamond core ($sp^3$ hybridization), at the basis of the luminescence properties in presence of color centers;
- a thin middle layer (typically up to ~ 1 nm) of distorted $sp^3$ phases and amorphous carbon;
- an outer non-crystalline shell of $sp^3$ and $sp^2$ carbon atoms, distributed in an anisotropic way, with various surface termination of hydrogen and oxygen [110].

NDs benefits from the biocompatibility of the bulk material and its intrinsic luminescence [111, 112, 113], thanks to the presence of optically active defects, the color centers [86]. They give NDs photoluminescence properties that make them excellent candidates as biomarkers for *in vitro* experiments [92, 107, 114, 115, 116].

### 1.3.4 Nitrogen-Vacancy center

The origin of ND fluorescence lies in the complexes formed by defects and impurities in the diamond crystal. The diamond lattice, in fact, can accommodate several types of these defects, consisting of:

- interstitial atoms, in the presence of additional atoms in the crystal lattice;
- substitutional atoms, when a carbon atom is replaced by different atomic species;
- vacancies, in the absence of a carbon atom from its lattice position.

These defects are naturally present in diamond or can be created during the growth process or by ion implantation techniques. The presence of such defects introduces additional electronic levels into the energy gap, that may be close to the valence or the conduction bands, determining a semiconductor behavior, or deep, resulting in localized electronic states. The latter usually occurs in the form of a fundamental state and one or more excited states, resulting in the possibility of radiative transitions in the visible light range. The electronic transitions between such localized states can give rise to the photoluminescence phenomenon called fluorescence (schematically depicted in Figure 15), when light is re-emitted at a longer wavelength, typically in the visible range, on return to the ground state. In this case, the defects are called "color centers" [117].

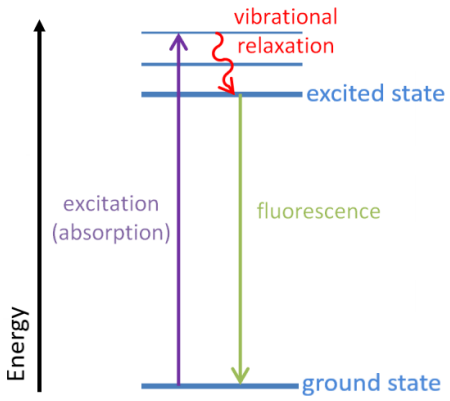


*Figure 15. Illustration of the fluorescence phenomenon [117].*

Color centers can be excited via an appropriate laser source with sufficient photons energy. Up to date, a large amount of color centers have been discovered in diamond, e.g.: silicon-vacancy (SiV) [118], germanium-

vacancy (GeV) [119], tin-vacancy (SnV) [120], and lead-vacancy (PbV) [121]. However, for the purposes of this thesis, the attention will be focused on the most documented among them, the nitrogen-vacancy (NV) center [122].

The NV center consists of a substitutional nitrogen atom nearby to a vacancy defect [123] (Figure 16).

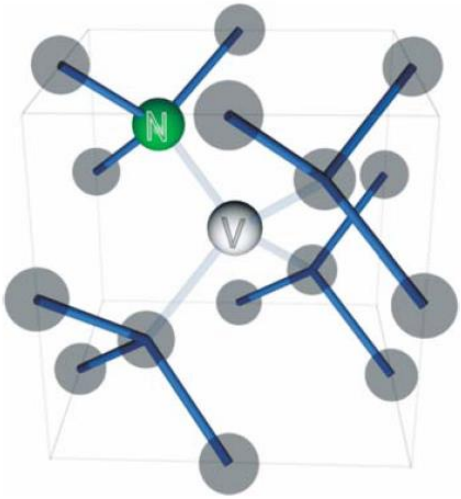


*Figure 16. Structure of the NV center [117].*

Due to its size, similar to that of carbon, the N atom fits easily into the lattice, representing the most common substitutional impurity in diamond crystals.

NV center in diamond occurs in two optically active states [124]:

- Neutral $NV^0$, a 5-electron (spin S = 1/2) system, four of which come from the dative bonds of the carbon atoms adjacent to the vacancy and one from the fifth valence nitrogen electron. It is characterized by a Zero Phonon Line (ZPL) emission spectrally located at 575 nm.

- Negative $NV^-$, with a negative charge due to the presence of a sixth electron trapped by the vacancy in the defect (spin S = 1) and a ZPL spectrally located at 638 nm.

This highly photo-stable fluorescent defect is strongly resistant to bleaching and quenching phenomena, which ensures the traceability of NDs without further functionalization with organic dyes. Therefore, this appealing property has attracted increasing interest for bioimaging purposes and has proven ND effectiveness for a wide range of diagnosis techniques [115, 125, 126, 127].

Fluorescence of NV centers can be observed under green laser excitation (532 nm). Overall, this defect has a wide red emission spectrum from 550 nm to 800 nm, long fluorescence lifetime (~ 20 ns) and high fluorescence quantum yield [128]. Moreover, the peculiar electronic level structure of the $NV^-$ center can be perturbed by magnetic field and thanks to the relaxometry technique it is possible to perform nanoscale magnetic resonance imaging (MRI) measurements, which provide appealing perspectives also for the investigation of biological samples, with extreme spatial resolution and sensitivity. More details concerning this technique and preliminary measurements conducted on NDs during a research period at the University Medical Center of Groningen (The Netherlands) are reported in Appendix A.

### 1.3.5 ND suitability for claims in the biomedical field

For various reasons, including the lack of industrial interest in nanotechnology at the time, the application of NDs remained unknown until two decades ago. Yu *et al.* published the first report on ND application for fluorescence imaging with a demonstration of their biocompatibility in cells in 2005 [84]. Subsequently, numerous studies demonstrated the wide-ranging potential of using NDs in different cells and uses. Indeed, as carbon nanomaterials, NDs inherit the outstanding properties of bulk diamonds, like

low toxicity [129, 130], an essential property for cell-survival, inertness and chemical stability.

Nowadays, the extraordinary properties of diamond make it attractive for scientific and technological applications, like drug delivery [131, 132, 133, 134], tissue engineering [135], bioimaging [136, 137], biosensor [138], and as radiosensitizer in RT treatments, offering benefits in comparison with conventional materials, such as metals. With regard to the latter feature, NDs can emit and produce secondary electrons or radicals upon stimulation by ionizing radiation, thus promoting DNA damaging, as will be better explained later in the discussion.

To mention some other possible applications, in photoacoustic microscopy, the ND great optical absorbance can render them suitable contrast agents to enhance signal sensitivity [133]. This parameter is also crucial to perform MRI and a controlled creation of paramagnetic NV defects could make NDs outstanding contrast agents for MRI based on T1 relaxation time (see Appendix A). Additionally, NDs can be used as carriers to enhance the biocompatibility of classic T1 based contrast agents [136]. Owing to their optical properties, NDs are naturally good probes for Raman imaging as they display a strong peak at 1332 $cm^{-1}$, which is far from living cell signals (between 2800 $cm^{-1}$ and 3200 $cm^{-1}$), allowing an easy monitoring without signal perturbation. Moreover, NDs present the possibility of facile surface functionalization with specific covalent bonds to allow the attachment of a broad variety of molecules and drugs [139, 140, 141, 142, 143, 144, 145]. ND surface moieties can also be easily and efficiently modified to achieve the desired specific physical and chemical characteristics, for example, using high-temperature thermal treatments carried out in a controlled atmosphere [146]. Due to the central role that the control of ND surface chemistry plays in the context of this thesis, the next section focuses on the description of the surface thermal modifications employed in this work.

## 1.4 Nanodiamond surface thermal treatments

NDs, like NPs in general, display a high surface-to-volume ratio, which results in a heavy influence of their overall properties by their surface structure and atoms [147]. Untreated ND surface (after the synthesis) presents miscellaneous functional groups (paragraph 1.3.3), depending on the production procedure employed. The main ones include oxygen-containing species, such as carbonyls, carboxyls, ethers, acid anhydrides and alcohol functions. Homogenize ND surface is a key step to further attach other molecules or simply more easily control their behaviour in solution or following irradiation.

Surface group modifications of NDs can be achieved with a wide range of wet chemistry approaches, acid treatments, exposure to microwave plasma or thermal treatments that lead to precise functionalisation, according to the desired result. This is fundamental in determining material characteristics and, consequently, in defining its applications.

Different thermal treatments in controlled atmosphere can be conducted to modify ND surface and the main ones employed during this thesis work are described in the next paragraphs.

### 1.4.1 Thermal annealing

The annealing treatment is a thermal process carried out at about 800 °C or more, in an inert atmosphere (argon/nitrogen flow or in vacuum) [148] that has the objective to standardize ND surface, by eliminating the outer functional groups, while graphitizing superficial amorphous carbon components, without undermining the diamond material [149] (Figure 17).

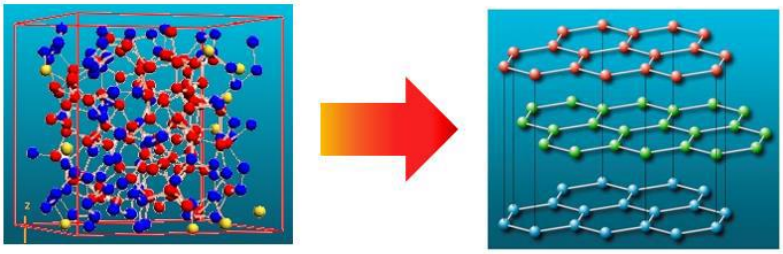

*Figure 17. Effects of annealing thermal process on diamond: it allows the graphitization of amorphous carbon components, organizing bonds in the $sp^2$ phase.*

This is true for both diamond bulk and NDs. No transition takes place for the diamond phase, whose conversion into graphite requires temperatures above 1100 °C - 1200 °C [150].

### 1.4.2 Thermal oxidation and hydrogenation

After the annealing process, thermal treatments aimed at improving $sp^2$ component on ND surface are predominantly oxidative [151, 152, 153, 154].

Oxidation processes are usually performed at temperatures between 400 °C and 550 °C in oxidant atmosphere (air or oxygen flow). Oxygen exposure at such temperatures lead to the selective and progressive removal of surface graphitic layers, decreasing the shielding and quenching effect on the luminescence produced in the diamond core [151]. In concomitance, this etching treatment forms many oxygen-containing groups (mainly carboxyl and carbonyl) on the surface [155] (Figure 18).

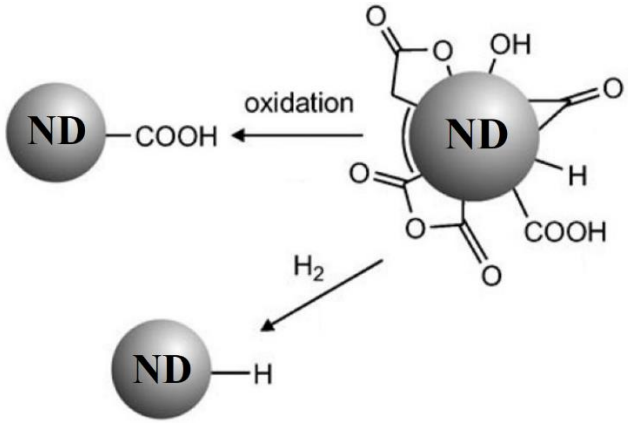


*Figure 18. Effects of thermal processes to modify ND surface: surface termination following oxidation or hydrogenation thermal treatments [156].*

These surface chemical species render oxidized-NDs (OX-NDs) highly hydrophilic and generally dissociate when dispersed in water, inducing a strong negative charge on the surface, which results in a highly negative zeta potential. The consequent electrostatic repulsion between particles prevents their agglomeration [155, 157].

In turn, oxidation can represent the starting substrate for additional treatments, e.g., chemical functionalization, or hydrogenation [149].

Hydrogenation of ND surface can be achieved through a thermal process in hydrogen gas at temperatures higher than 600 °C [158], aiming at create C-H bonds. Hydrogenation produces concurrent etching of non-diamond carbon and elimination of oxygenated groups, which makes the surface more hydrophobic [159, 160]. Therefore, hydrogenated-NDs (H-NDs) present hydrophobic nature [161].

Another effect of hydrogen terminations is to confer NDs a negative electron affinity (χ). χ is defined as the energy difference between the vacuum level ($E_{vac}$) and the conduction band minimum ($E_C$)

$$\chi = E_{vac} - E_C$$

and is equal to -1.3 eV for hydrogenated diamond [162].

The effect of these hydrogen terminations can be explained in terms of a simple electrostatic model, taking into account carbon and hydrogen electronegativity (X). In general, heteropolar bonds, arising from surface-terminating atoms, carry a dipole moment, whose sign and magnitude depend on the difference in X between these surface atoms and the carbon atoms of the diamond lattice. Let $p$ be the component of the dipole moment of a surface-terminating bond perpendicular to the surface, counted positive with positive partial charge pulled towards the vacuum side and negative pulled towards the semiconductor side. A layer of such dipoles, with areal density $n$, causes an electrostatic potential step ($\Delta V$) perpendicular to the surface over a distance of the order of the surface bond lengths. The change in electron affinity caused by the surface dipoles ($\Delta\chi$) is proportional to $\Delta V$, according to the expression:

$$\Delta\chi = -e\Delta V = \frac{-epn}{\varepsilon_0}$$

where $e$ and $\varepsilon_0$ are respectively the elementary charge and the vacuum permeability [163]. Since hydrogen X is lower than that of carbon ($X_H = 2.20$, while $X_C = 2.50$ in Pauling's scale) [164], the C-H bond is polarized with a positive charge $\delta^+$ on the H atom. Hence, the dipole moment component of the C-H bonds perpendicular to the surface is positive ($p = 0.08$ eÅ) and, as a result, $\chi$ is diminished, becoming negative [163].

In contrast, due to the high electronegativity of O ($X_O = 3.44$), oxydated diamond presents a positive $\chi$, with a value of + 1.7 eV.

Hydrogen terminations also considerably decrease ionization energy I (defined as the difference between $E_{vac}$ and the top of the valence band $E_v$), to 4.2 eV (Figure 19).

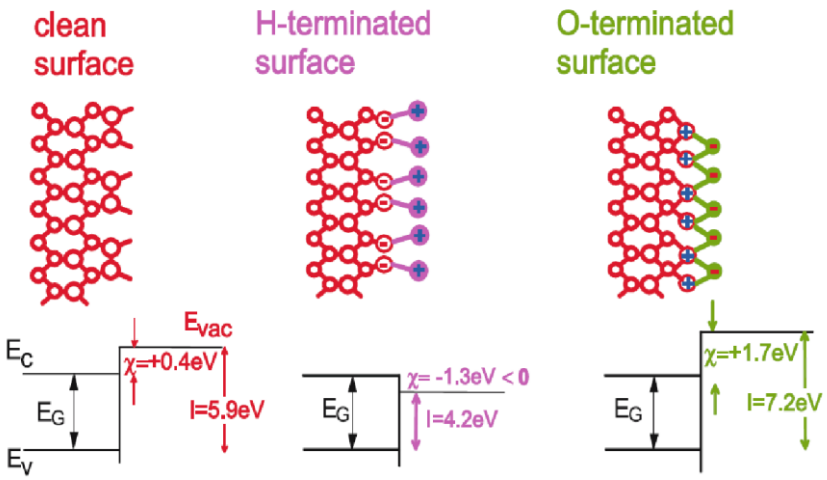


*Figure 19. Scheme of the modification of electron affinity χ and ionization energy I of diamond surfaces by hydrogen and oxygen terminations and band diagrams for the clean and the fully H/O-terminated diamond surfaces [163].*

Consequently, hydrogenated diamond can transfer electrons from $E_v$ to physiosorbed surface adsorbates, particularly water, provided that their χ exceeds (or at least comes close to) this value. The phenomenon results in the formation of a subsurface layer of accumulation of holes, leading to a significant surface conductivity [163]. This effect was first recognized in 2000 by Maier *et al.*, who developed an electrochemical surface transfer doping model [165], schematically illustrated in Figure 20.

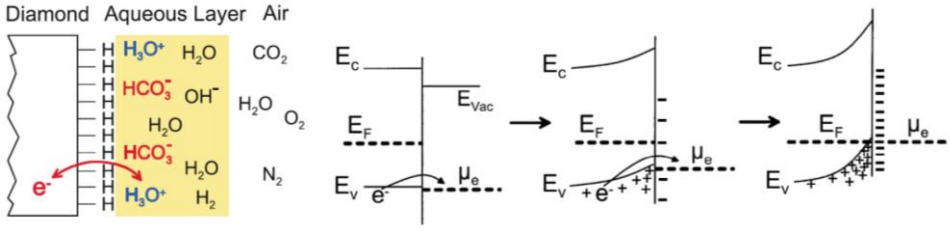


*Figure 20. Transfer doping of hydrogenated diamond surfaces by water, that originates surface conductivity [163, 165]. The space-charge separation brings to a confinement of the holes to the surface by an upward band bending potential.*

They proposed that a thin water layer formed over the whole surfaces after atmosphere exposure acts as an electron acceptor system for hydrogenated diamond and leaves holes as mobile charge carriers, allowing the observed surface conductivity. The electron exchange from diamond to the water layer is driven by the difference in the chemical potential of electrons in the liquid phase ($\mu_e$) and in diamond (Fermi level, $E_F$) and causes the reduction of hydroxonium ions to $H_2$ and $H_2O$. Electron transfer is regulated by the following redox reaction:

$$2H_3O^+ + 2e^- \leftrightarrow 2H_2O + H_2$$

and continues as long as $\mu_e$ is below $E_F$, until equilibrium is reached. At equilibrium, $\mu_e$ and $E_F$ are equal at the interface.

Similarly with bulk diamond, the above-mentioned properties are transferable to NDs and among surface terminations of NDs, hydrogen one is known to give specific properties to these NPs, which enable their use as radiosensitizers.

### 1.4.3 Application of H-NDs as radiosensitizers

As mentioned above, terminating the ND surface with hydrogen atoms, they exhibit a surface negative electron affinity $\chi$, together with a positive charge, in aqueous solutions [87]. These H-NDs can thus promote the emission and transfer of secondary electrons to water molecules under irradiation [162, 164, 166]. Therefore, H-NDs can act as an efficient source of ROS in addition to radicals generated by ionizing radiation alone. This results in the local amplification of indirect biological damage and in the enhancement of RT-induced effects on cancer cells [87, 167, 168]. For this reason, in the last decade, H-NDs are attracting increasing attention in the context of RT radiosensitization notably thanks to their availability and versatility, even if it is still unclear whether the damages can be sufficient for explaining the increase in radiation-induced cell death in the presence of NDs [75].

However, although the studies on ND-mediated radiosensitization are sparse, there are excellent indications that these NPs represent an interesting subject of examination, due to their potential efficacy in the hydrogenated form [87] and their potentialities have been evidenced in diverse works [56, 75]. For example, in their study, Petit *et al.* observed a clear raise of the ROS generation in kidney human cancer cell line Caki-1 when combining H-NDs and γ-rays [167]. Grall *et al.* showed that a co-exposure to H-NDs and γ photons induced more cell death, enhancing the anti-tumor effect of RT in Caki-1 and ZR75.1 human mammary carcinoma cells. They correlated the phenomenon with a higher ROS concentration, prompting sustained DNA DSBs [87]. Kurzyp *et al.* revealed an increase of the 40% of •OH production under X-ray irradiation in the presence of H-NDs, compared to radiation alone [168].

Hence, despite further investigations are required to better understand and fully explore the use of NDs in this research field, all these findings confirm that H-NDs have promise in improving RT treatments.

## 1.5 Objectives of the research activity

The research activity concerned the study, optimization and application of the radiosensitizing capability of NDs with different chemical/physical characteristics (surface modifications, sizes, and concentration) in the radiotherapeutic treatment of oncological pathologies, and in particular of brain tumors.

The first part of the work included the processing and characterization of NDs modified by means of thermal treatments for their application as radiosensitizers. As underlined in the previous section, each surface modification (annealing, oxidation, and hydrogenation) offers specific physical and chemical properties, whose characterization was carried out by combining multiple measurement techniques. In particular, the activity of the

candidate focused on the analysis of the physicochemical properties of processed NDs through Raman and photoluminescence spectroscopy, Diffuse Reflectance Infrared Fourier-Transform spectroscopy and Dynamic Light Scattering analysis.

Once ND samples were characterized, they were used in experiments of induced-radiolysis, aiming at the estimation of the ROS production (in particular •OH radicals) in aqueous solutions following irradiation. The water solutions, containing NDs and a fluorescent probe (the terephtalic acid) were irradiated by an X-ray source (130 kVp) and examined through spectrofluorimetry analysis. The experimental setup for such analysis was assembled and tested by the candidate.

Subsequently, the processed ND samples were investigated for interalization in a radioresistant human MB cell line (DAOY HTB-186 cells) at the Laboratory of Biomedical Technologies (TEB) of the Casaccia Research Centre (Roma) of the Italian National Agency for New Technologies, Energy and Sustainable Economic Development (ENEA).

As initially mentioned, MB is the most common malignant brain tumor in children and RT is the most important adjuvant treatment for MB. The conventional doses of RT delivered to the craniospinal axis and to the posterior fossa are 54 Gy - 56 Gy. Using such doses, a high proportion of MB survivors have significant long-term consequences, including marked losses of IQ and endocrine dysfunction [28]. Controlling tumour growth while trying to reduce the radiation dose to avoid long-term neurocognitive effects is a challenge, especially in young children.

During the collaboration with the ENEA TEB laboratory, different characterization techniques were employed for the internalization studies, such as fluorescence microscopy, Raman spectroscopy and flow cytometry.

Finally, the candidate conducted *in vitro* analysis on DAOY cell cultures to explore the effects of radiation treatments combined with NDs using

different photon sources: an X-ray generator operating at 250 kVp and a 1.25 MeV γ-source. Clonogenic assays were used to evaluate the consequences of combined treatments on cell survival and some hypothesis were formulated to identify the biological parameters involved in the radiosensitizing effects of H-NDs.

# 2 Experimental setup

In this chapter, the instruments and the setups used and built up during the research activity are presented. The experimental methods employed are also explained in detail.

## 2.1 Nanodiamond samples

Three nanodiamond (ND) batches were employed, all obtained by milling High Pressure High Temperature (HPHT) type-Ib single crystals (nominal nitrogen concentration between 10 ppm and 100 ppm), namely:

- Pureon (Lengwil, Switzerland) monocrystalline synthetic diamond (MSY) with average particle diameter equal to 18 nm (referred as 18 nm NDs);
- Pureon MSY NDs with a median diameter of 55 nm (55 nm NDs);
- Micron+ NDs purchased from the manufacturer ElementSix™ (Harwell Oxford, UK) and with a median size of 240 nm (240 nm NDs).

## 2.2 Thermal treatment system

Before sample investigation, the ND surface was modified by thermal treatments in a tubular furnace [169]. ND powders were loaded into inert alumina crucible boats to allow ND insertion inside the furnace ThermoConcept ROT 60/300/12 (Figure 21), where the thermal processes were performed [170].

*Figure 21. ThermoConcept ROT 60/300/12 tubular furnace.*

Time and temperature of the treatments can be set thanks to the furnace control system, by programming different thermal ramps according to the desired thermal protocol. A controlled atmosphere (inert gases, air, oxygen, …) can be maintained during the whole process. The parameters (time and temperature) of the processing steps carried out on a specific batch of NDs will be better displayed in some schemes reported in section 3.1 of chapter 3, while here only the working of the processes is described.

All ND samples were subjected to an annealing treatment. The samples were maintained in inert nitrogen laminar flow inside the tube, to standardize the untreated ND surface, eliminating the heterogeneous functionalities. At the same time, this thermal process aims at reorganizing the disordered $sp^2/sp^3$ phases [146] and graphitizing the amorphous carbon components on the surface without damaging the diamond phase [149]. The setting of an optimal annealing temperature is of fundamental importance. On one hand, the nitrogen environment prevents the chemical etching of diamond that would occur above 500 °C in presence of oxygen [171]. However, despite the oxygen-free atmosphere, a temperature below 900 °C is necessary to prevent the ND samples from graphitization [172] and the conversion to carbon

onions [149]. Therefore, to avoid structural and chemical degradation, the annealing treatment was carried out at temperatures of 800 °C for 2 h. These processes made NDs suitable for the following processing steps, while also forming new nitrogen-vacancy (NV) centers, thanks to the high-temperature-induced pairing of nitrogen impurities and native vacancies.

After the annealing treatment, to selectively remove the superficial $sp^2$ carbon, the next step involved thermal oxidation (etching) processes, aimed at purifying NDs from the residual graphitic phases. Promoting the formation of surface oxygen-containing functionalities [151], these treatment were carried out in air at temperatures between 475 °C and 500 °C, keeping below the diamond air degradation temperature, for times ranging from 12 h to 36 h to produce the oxidized-NDs (OX-NDs).

Eventually, oxidation might be the starting point of hydrogenation processes, as it allows a more efficient creation of C–H covalent bonds on the outer ND surface, obtaining the hydrogenated-NDs (H-NDs). Whereas during oxidation the samples were exposed to the air-contained oxygen (oxidizing atmosphere), in hydrogenation NDs were maintained in hydrogen laminar flow, at temperatures between 750 °C and 850 °C for 2 h, 3 h or 6 h. Hydrogen was produced from water electrolysis with a Parker Domnick Hunter 60H Hydrogen Generator (Figure 22), guaranteeing a gas purity > 99.999% and 0 bar - 7 bar output pressure.


*Figure 22. Parker Domnick Hunter 60H Hydrogen Generator.*

## 2.3 ND chemical/physical characterization

After thermal processing, a systematic characterization of differently sized ND samples is crucial for defining the thermal treatments effects on ND properties. In addition, this constitutes a key step to subsequently identify the best features that emphasize ND radiosensitizing skills towards their final application for tumor treatment.

### 2.3.1 Diffuse Reflectance Infrared Fourier-Transform (DRIFT) spectroscopy

DRIFT spectroscopy involves infrared wavelengths to irradiate the sample, which converts the absorbed radiation into vibrational energy. This technique records the absorbed frequencies, characteristic for each specific chemical bond, providing unique information on the influence of the material superficial chemistry, for example on its behaviour in solution. Moreover, it

allows the identification of the types of molecules and surface functional groups in a simple and nondestructive manner [173].

To assess the efficacy of oxidation and hydrogenation treatments and to examine ND hydrophilicity, DRIFT spectra were collected in diffuse reflectance mode commonly employed to investigate rough surfaces and powders, using a Bruker Vector 22 FTIR spectrometer (Department of Chemistry, University of Torino, Figure 23).

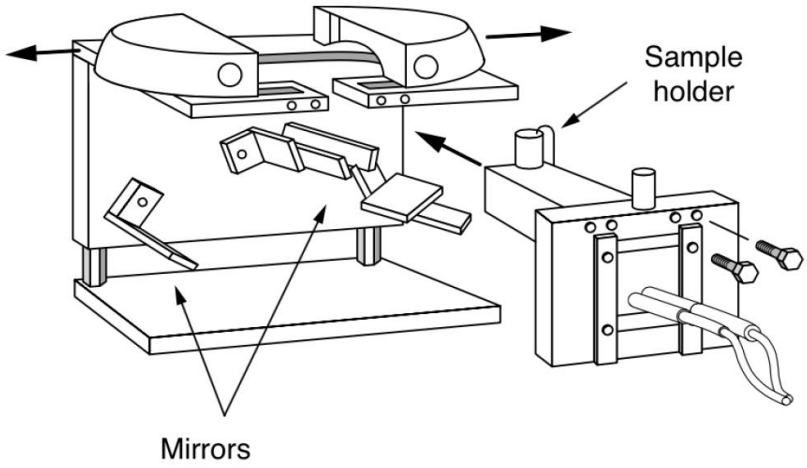


*Figure 23. Scheme of the Bruker Vector 22 FTIR spectrometer.*

A mirrors series focuses the infrared beam on the sample surface, resulting in both specular reflectance (which directly reflects off the surface, with equal angles of incidence and reflectance) and diffuse reflectance (which penetrates into the sample, originating multiple reflections in all angles between the surfaces of the individual particles that compose it). A second mirror system transfers both radiations to a mercury-cadmium-telluride detector operating at low temperatures (liquid nitrogen cooling). The setup allows the acquisition of each spectrum under dry air ambient condition (i.e., relative humidity ~ 10%) and the samples were characterized by averaging 64

acquisitions at a spectral resolution of 2 $cm^{-1}$. The reflectance data were then transformed in pseudo-absorbance values ($A$):

$$A = -\log R$$

where $R$ is the measured reflectance.

### 2.3.2 Micro-Raman spectrometer

In this work, to evaluate ND quality and assess both the structural modifications induced by thermal treatments and the luminescence properties of the samples, Raman and photoluminescence spectroscopies were performed using the same instrument. In particular, a Horiba-Jobin-Yvon HR800 microspectrometer (Horiba Italia S.r.l., Torino, Italy) available at the Scansetti Interdepartmental Centre of the University of Torino (Figure 24) was used.

*Figure 24. Micro-Raman spectrometer Horiba-Jobin-Yvon HR800 at the Scansetti Centre (University of Torino).*

The instrument, controllable through LabSpec software, is equipped with a continuous Nd-YAG 532 nm excitation laser and a charge-coupled device (CCD) detector, incorporating a Peltier cooling system (-70 °C). The laser power intensity incident on the sample position was set to 1.69 mW, allowing

the quick collection of spectra and avoiding the self-heating phenomena that typically affect nanoparticle (NP) analysis [139]. The system includes an Olympus BX41 optical microscope, whose 20× objective allowed the laser beam focusing into a desired point and focal plane, enabling to probe a sample area of 10 × 10 $\mu m^2$ at a confocal depth of ~ 3 μm. The 600 lines $mm^{-1}$ diffraction grating provided a 3 $cm^{-1}$ spectral resolution in Raman shift. During the measurements, the integration time was set to 20 s and 3 repeated acquisitions were averaged to improve the signal statistics. For data collection, the NDs were dispersed in isopropanol and deposited on a silicon wafer substrate.

In the following, some details on the two spectroscopic techniques available from the analysis with this instrument (Raman and photoluminescence spectroscopies) are described.

## Raman spectroscopy

Raman spectroscopy was employed to assess the structural information of NDs, investigating their "chemical fingerprints" and their content in terms of diamond, graphitic and amorphous carbon phases. Indeed, this method is useful to monitor possible structural modifications induced by thermal treatments. It is based on Raman effect, i.e., the inelastic scattering of light by matter [174]. For a crystal, this phenomenon arises from the interaction of the incident light with optical phonons (vibrational motions). The energy schemes reported in Figure 25 depict the main Raman scattering events.

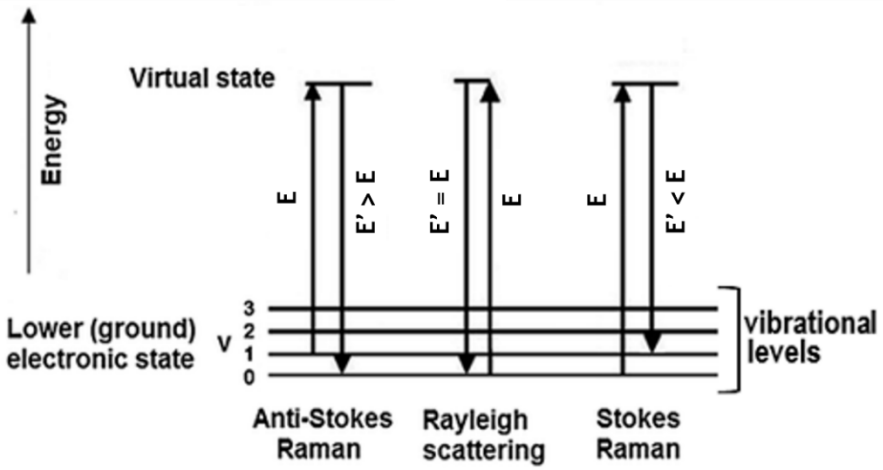


*Figure 25. Energy scheme representing Rayleight (elastic) scattering and Raman (inelastic) scattering (both Stokes and anti-Stokes processes are displayed) [175].*

If the incident photon energy ($E$) is lower than the differences between the levels, photons can be absorbed and re-emitted, assuming the creation of a virtual state of an electron-hole pair. Rayleigh scattering occurs when, during the existence of such virtual state, no phonons are created or destroyed. Conversely, if a phonon is created/destroyed, the photon re-emitted following the recombination of the electron-hole pair will have an energy ($E'$) lower/higher than that of excitation ($E' \neq E$), resulting in the so-called Stokes ($E' < E$) or the anti-Stokes ($E' > E$) Raman effect [176]. This energy shift, called Raman shift, is equal to the energy of the phonon exchanged and is specific to each type of lattice vibration. From this effect, structural information on the crystal can be obtained, allowing sample identification [177]. In particular, for single-crystal diamond the energy of the phonons, and therefore the Raman shift, expressed in wavenumber, is 1332 $cm^{-1}$ [104].

## Photoluminescence spectroscopy

Photoluminescence spectroscopy allowed to obtain optical information of NDs, investigating the fluorescence arising from NV centers. Indeed, the

interaction of the incident light with diamond and the radiative transitions in the visible light range can promote photoluminescence phenomenon of NV color centers, that ensures ND traceability without further functionalization with organic dyes.

Fluorescence of NV color centers can be excited via green laser source (532 nm), while their wide red emission spectrum goes from 550 nm to 800 nm, with long fluorescence lifetime (~ 20 ns) and high fluorescence quantum yield [128].

### 2.3.3 Dynamic Light Scattering (DLS)

The proper dispersability and stability of NDs in solution are also of paramount importance and DLS analysis was employed to study ND aggregation tendency and to obtain the size of the particles dispersed in a liquid. In DLS measurements, a laser beam is focused on the solved sample, contained in a vial, and an avalanche photodiode detector collects its scattered light. This generates an image called “speckle pattern” (Figure 26), resulting from constructive/destructive (bright spots/dark regions) interference phenomena of the scattered light after the beam interaction with the particles in the liquid.

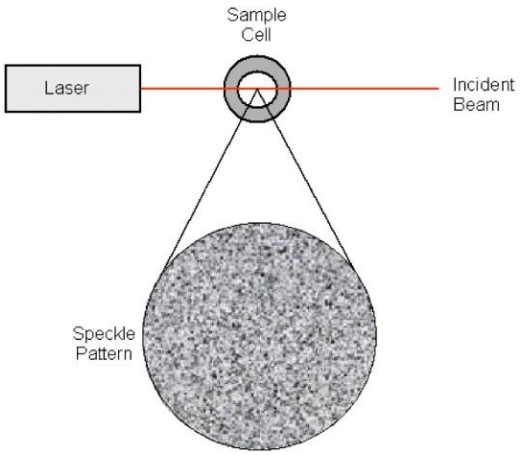


*Figure 26. Schematic representation of a speckle pattern in the DLS instrument [178].*

The light intensity of a speckle, fluctuating over time due to the particle random motions, is evaluated at successive time intervals and processed by a digital board, named correlator. The correlator constructs the correlation function of the scattering intensity $g(\tau)$ [178], given by:

$$g\ (\tau) = \frac{\langle I(t)I(t+\tau)\rangle}{\langle I(t)\rangle^2}$$

where $I(t)$ is the measured light intensity at time $t$ and $\tau$ is the time difference (or delay time) of the correlator [179]. For spherical Brownian particles (as NDs), the function

$$G(\tau) = g(\tau) - 1$$

decays exponentially. If the particles are large, $g(\tau)$ decays less rapidly, since the signal $I(t)$ changes slowly, whereas the opposite happens for small particles, moving quickly [178]. Therefore, the working principle exploits the Brownian motion: the particles in solution are constantly moving due to the thermal agitation of the liquid, with a velocity inversely proportional to their mass and, consequently, to their size. DLS directly measures a hydrodynamic quantity, namely the particle translational diffusion coefficient, related to particle size [180]. Faster variations are due to the passage of smaller NPs and vice versa for slower variations (Figure 27A).

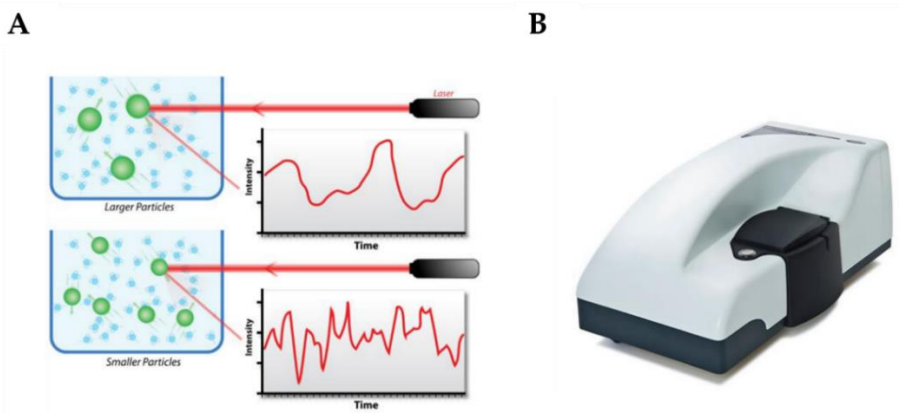


*Figure 27. (**A**) Hypothetical fluctuations of scattered light intensity signal over time in DLS analysis due to the motion of large and small particles in solution [181]. (**B**) Zetasizer Nano ZS.*

More precisely, the decay rate $\tau_c^{-1}$ of $G(\tau)$ is expressed by:

$$\tau_c^{-1} = 2Dq^2$$

where $D$ is the particle translational diffusion coefficient and $q$ is the scattering vector:

$$q = \frac{4\pi n}{\lambda_0} \, sin\left(\frac{\theta}{2}\right)$$

$n$, $\theta$ and $\lambda_0$ are the refractive index and the scattering angle of the liquid, and the laser excitation wavelength of the instrument, respectively.

$D$ depends on the particle hydrodynamic diameter $d_h$, defined as the diameter of a sphere having the same translational diffusion coefficient as the particle, according to the Stokes-Einstein equation:

$$d_h = \frac{kT}{3\pi\eta D}$$

in which $k$ is the Boltzmann's constant, $T$ is the absolute temperature and $\eta$ is the viscosity of the solvent [179]. It is worth noting that *D* depends also on particle surface structure and on the concentration and type of ions in the medium: the measured dimensions are hence affected by these factors [182].

For DLS analyses, a Malvern Instruments Zetasizer Nano ZS (Malvern, UK, Figure 27B) and Zetasizer software were employed. The instrument operated with a 4 mW power He-Ne laser source (633 nm, 173° scattering angle), by setting the refractive index of diamond (2.4). ND size analysis was conducted in phosphate-buffered saline (PBS) solutions, with a ND concentration of 10 μg $ml^{-1}$. Before every acquisition, the solutions were sonicated for 30 min. Then, ND suspensions were placed in a DTS0012 cuvette for the characterization.

## 2.4 Measurement of ND effects on hydroxyl radical production by water radiolysis

### 2.4.1 Spectrofluorimetry technique and instrumentation

During the study of reactive oxygen species (ROS) production in the presence of NDs, spectrofluorimetry (or simply fluorometry) was used. It is a quantitative versatile spectroscopic technique, aimed at determining the quantity of a fluorescent substance within a sample [183]. Indeed, this chemical analysis is based on the physical phenomenon of fluorescence. The spectrofluorometer is the main instrument used in fluorometry. A typical spectrofluorometer, contains a light source, a compartment to insert the samples, different configurations of optical filters, providing specific excitation and emission wavelengths, and finally a detector [184, 185].

The experimental setup employed to analyse the hydroxyl (•OH) radical production in this study, schematized in Figure 28, is a custom fluorometer, built up specifically for these measurements by the candidate, and designed to replicate, in a simpler and compact but still high-performance form, a commercial fluorometer.

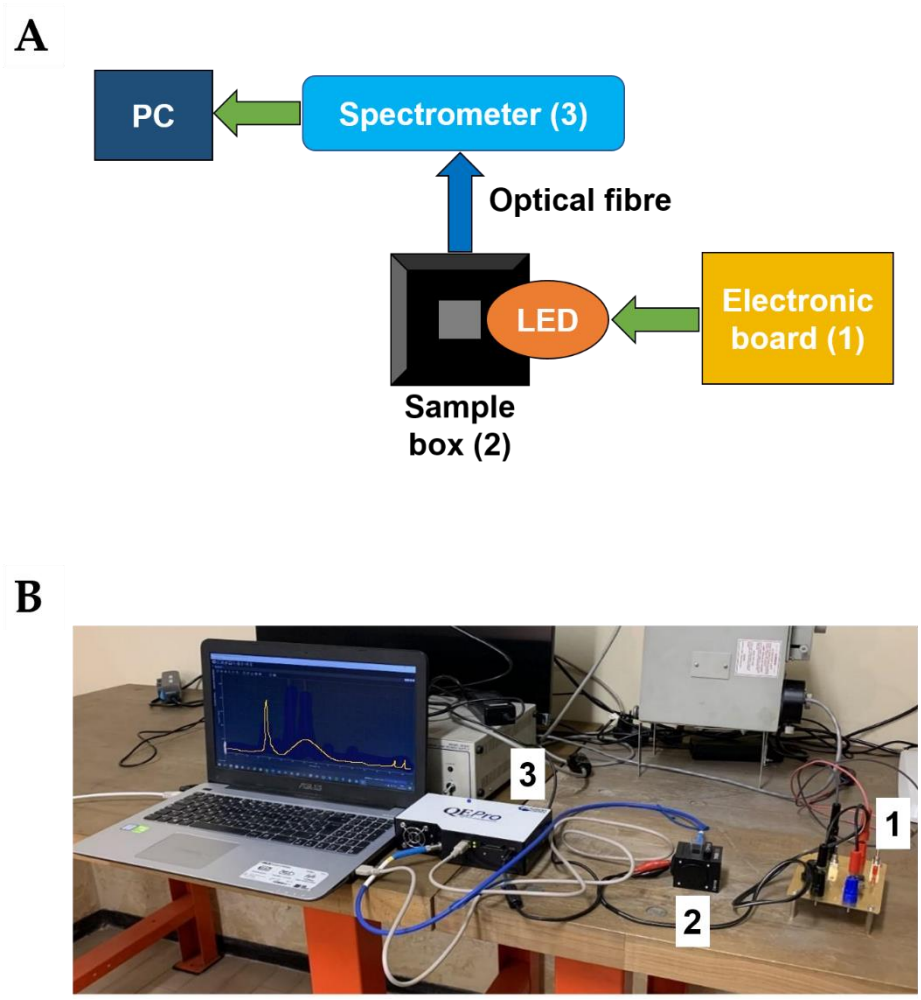


*Figure 28. (**A**) Diagram of the main components of the fluorometer used in this work, built up by the candidate. (**B**) Fluorometer setup: the 315 nm led excitation source was powered by an electronic board (1), the samples were placed into a quartz cuvette contained in a black box (2) and the spectrometer (3) allowed to collect the fluorescence spectra.*

The main characteristics and the devices constituting this apparatus are briefly described in the following.

- Light source: Thorlabs UV-visible led 315W, with a 315 nm emission wavelength, 30 mA forward current and 0.600 mW power (Figure 29A). It was specifically chosen for the terephthalic acid (TPA) probe, more deeply defined later in this paragraph.

- Electronic board, to power the led circuit. The led power supply current was set at 15 mA.
- Compartment to insert the samples: Thorlabs UV-led black box, to guarantee optimal measurements even for photosensitive materials. It can be closed in every direction and due to its colour and opacity, it can reduce the environmental light noise.
- Quartz cuvettes to contain the sample solutions, transparent to UV and visible light and polished on every side (Figure 29B).
- UV-led optical fibre, characterized with 0.50 NA and 200 nm in length, to collect visible light. The light optical paths of excitation and detection are along orthogonal axis (Figure 28A).
- Detector: Ocean Optics QEPro Spectrometer, equipped with a thermoelectrically cooled Hamamatsu S7031-1006 detector (15 °C - 20 °C below ambient temperature) and controllable by the OceanView software, that allow spectrum acquisition.

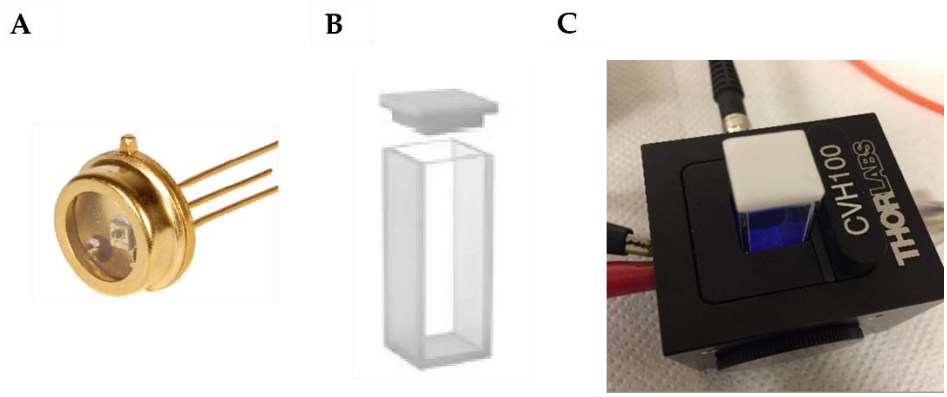


*Figure 29. (**A**) UV-visible led. (**B**) Quartz cuvette. (**C**) Cuvette inside the black box with irradiated TPA solution lighted with the led.*

To observe •OH in water systems, in addition to the fluorometry setup, a probe is necessary: Page *et al.* [186] suggested the use of the hydroxylation reaction of TPA. This is a non-fluorescent molecule, which following the interaction with the •OH radical yields a single hydroxylated product, i.e., the

fluorescent chromophore 2-hydroxyterephthalic acid (HTPA) [187] (Figure 30).

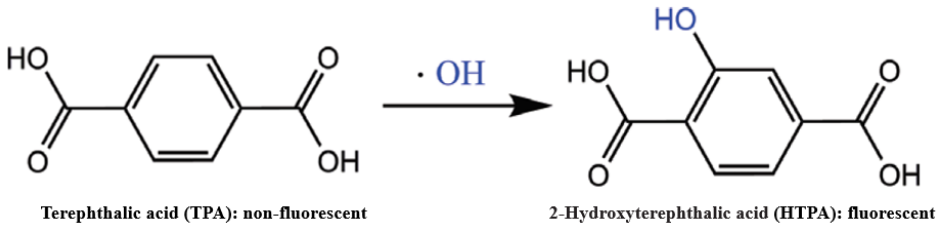


*Figure 30. Reaction of terephthalic acid (TPA) with hydroxyl radicals (•OH), rising to 2-hydroxyterephthalic acid (HTPA). Contrary to TPA, HTPA is fluorescent and it is useful to quantify •OH-radical production.*

TPA provides a high degree of selectivity, not requiring long irradiation times or high probe concentrations and HTPA is characterized by a bright stable fluorescence at a wavelength (λ) of almost 430 nm when excited with $\lambda \approx 315$ nm (Figure 31).

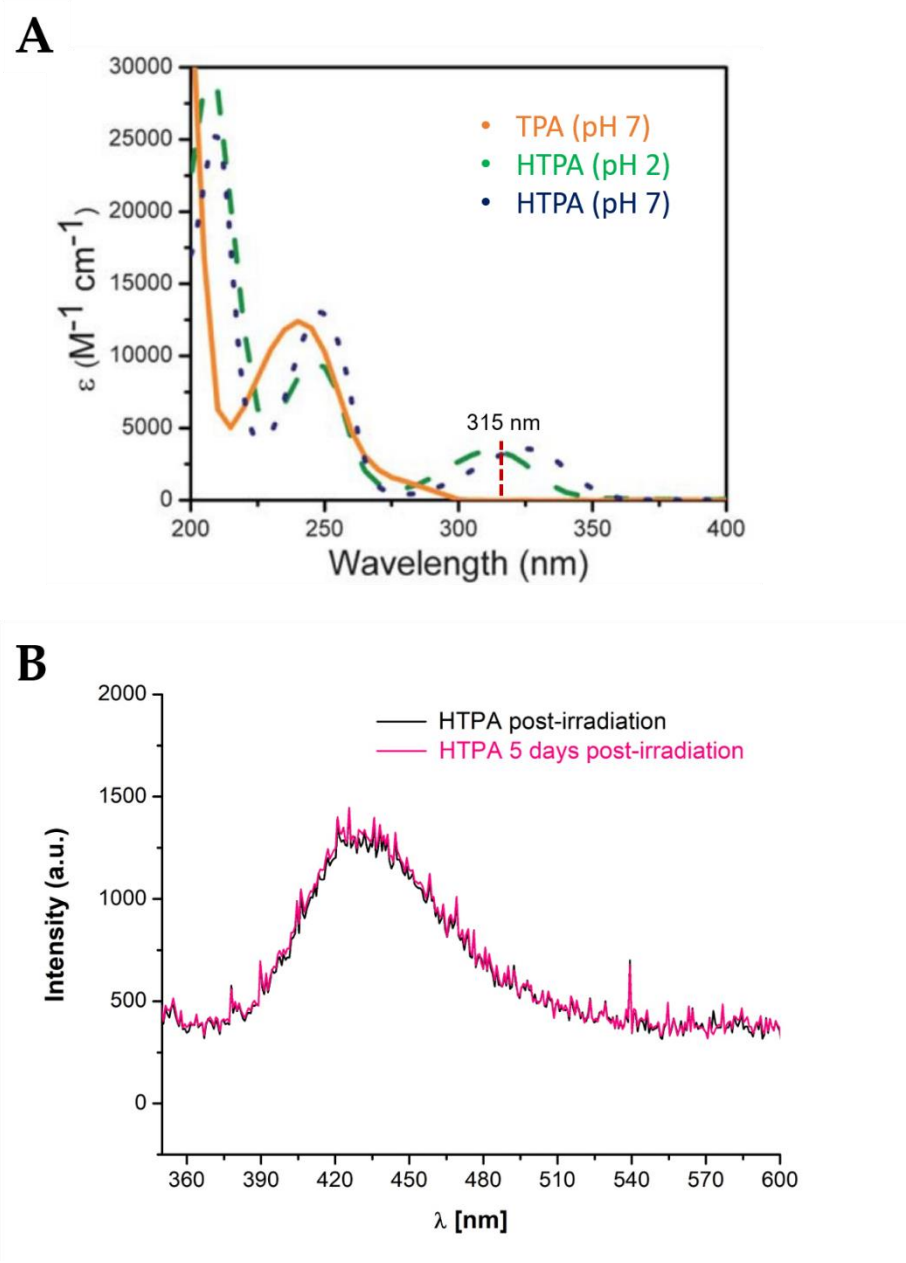


*Figure 31. (**A**) TPA and HTPA absorption spectra at different pH values [186]. (**B**) Post-irradiation spectra, presenting the HTPA peak with its stable fluorescence, detected for the same sample immediately (black curve) and 5 days (pink curve) post-irradiation.*

Therefore, HTPA fluorescence can be detected by spectroscopic measurements [188]. In this work, it has been exploited to quantitatively

determine the •OH radicals, produced following irradiation of the ND/TPA-containing samples, using the homemade fluorometer previously described.

To obtain suspensions with particle concentration of 10 μg $ml^{-1}$, NDs were dispersed in PBS-based solutions with a TPA concentration of 0.05 mM (TPA by Sigma-Aldrich). The samples were ultrasonically stirred for about 30 min before X-ray irradiation. The fluorescence spectra were collected, with an integration time of 30 s, by placing the samples into quartz cuvettes, inside the black box of the setup. As displayed in Figure 28, the led light was delivered directly to the sample, while the optical fibre was used to convey the radiation emitted from the solutions to the spectrometer. During the experiments, the fluorescence spectra were recorded both pre-irradiation, to have a reference signal (white spectra), and post-irradiation, to reveal the fluorescence from the •OH radical-generated HTPA. Two exemplary spectra are shown in Figure 32.

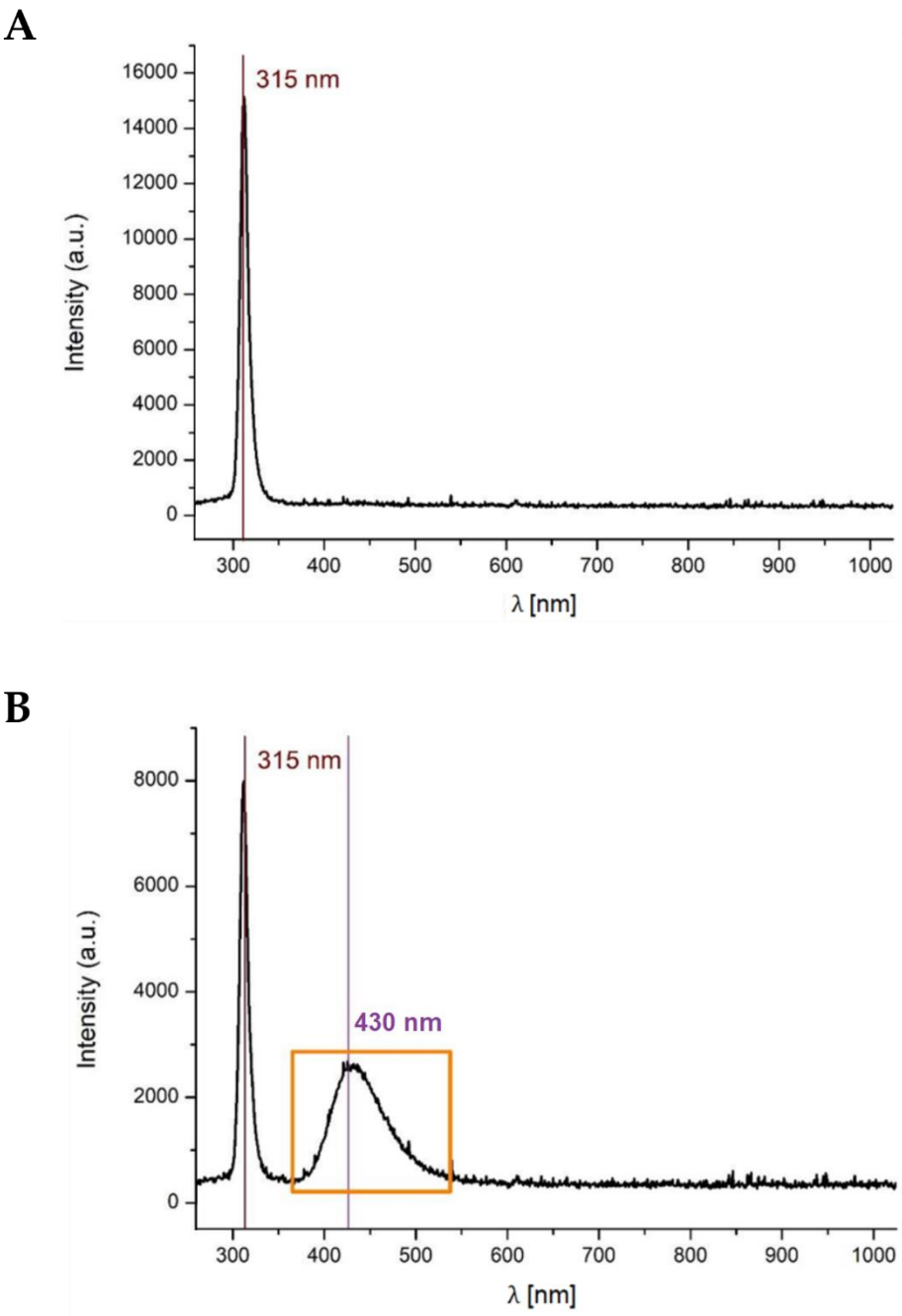


*Figure 32. Example of fluorescence spectra of TPA solutions. (**A**) Pre-irradiation spectrum (white spectrum), showing the peak of the exciting led at 315 nm. (**B**) Post-irradiation spectrum, presenting the peak of the exciting led at 315 nm and the HTPA peak, marked with an orange rectangle, with its maximum at ~430 nm.*

These plots show the fluorescence intensity as a function of λ and from the post-irradiation spectrum (Figure 32B) is easy to distinguish the HTPA peak

with its maximum around 430 nm. Moreover, all the spectra present the peak at 315 nm of the led employed to excite the solutions. To obtain the information about •OH radical production, the area under HTPA luminescence emission peaks was evaluated in a range between 390 nm and 560 nm. The integration value for each curve was converted in a radical concentration through the fit obtained from the HTPA calibration curve (paragraph 3.3.2). To normalize the data, the ratio with the •OH concentration mean value obtained for the only TPA-samples was considered, to compare the ND effects on the radical production.

### 2.4.2 Microfocus X-ray irradiation source

To irradiate the ND solutions with X-ray photons, a microfocus Hamamatsu L8121-03 source, operating at 130 kVp (peak kilovoltage), 400 μA was employed. It has a 200 μm thick beryllium output window, that was covered by an aluminium filter with 1 mm thickness, and a radiation cone angle of 43°. A wood support was used to keep the samples at 9.5 cm from the X-ray source (this configuration assured a complete and homogeneous irradiation, Figure 33).

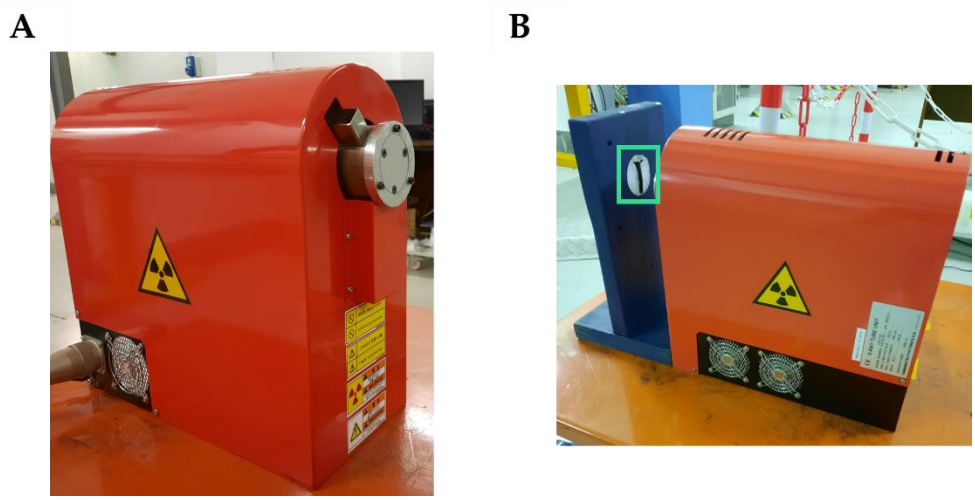


*Figure 33. (**A**) X-ray microfocus Hamamatsu L8121-03 source. (**B**) Irradiation configuration: positioning of the sample (black Eppendorf in the green box) with respect to the X-ray source.*

## 2.5 Measurement of ND effects following *in vitro* irradiation

### 2.5.1 Cell cultures and ND administration

Human medulloblastoma (MB) cell lines (DAOY HTB-186) were obtained from American Type Culture Collection (ATCC; Manassas, VA, USA). Cell lines were routinely maintained in the complete growth medium Eagle's Minimum Essential Medium (MEM) with 2 mM glutamine and 100 U penicillin/0.1 mg/ml streptomycin, supplemented with 10% foetal bovine serum. Cells were cultured in standard $CO_2$ incubators in an atmosphere of 2% oxygen, 5% carbon dioxide, and balanced nitrogen.

Prior to incubation in MB DAOY cells, NDs were resuspended in bidistilled water at 1.6 mg/ml, autoclaved at 121 °C for 15 min and sonicated for 30 min. Sonicated NDs were added into the cell culture dish, where the cells were previously plated to have the desired final concentration, specified for each experiment.

### 2.5.2 Visualization of ND cellular location and internalization

#### Fluorescence microscopy

DAOY cells were plated on 20 mm glass bottom cell culture dish (NEST) and treated for 13 h with NDs in MEM with 10% foetal bovine serum at 37 °C. ND-treated cells were fixed with 4% Paraformaldehyde *w/o* methanol in PBS for 10 min, permeabilized with 0.1% Triton X-100 in PBS for 3 min, blocked with 1% bovine serum albumin (BSA) for 30 min and stained with 1.65 µM Alexa Fluor™ 488 Phalloidin (Invitrogen, 518 nm, green emission) to selectively label F-actin, 1 µg/ml 4′,6-diamidin-2-fenilindolo (DAPI, 470 nm, blue emission) to visualize nuclei labelling DNA, and 1% BSA in

PBS for 20 min in the dark. Ultimately, cells were washed twice with PBS and mounted with Vectashield mounting medium for fluorescence (Vector Laboratories, Newark, CA, USA).

The cell cultures were imaged and analysed with an Axio Observer 7 semi-confocal inverted microscope (ZEISS, Oberkochen, Germany, Figure 34), using different filter sets: 96 HE, 489096-9100-000 (excitation Bandpass BP 390/40, beamsplitter FT 420, emission BP 450/40) for DAPI emission detection; 38, 1031-346 (excitation BP 470/40, beamsplitter FT 495, emission BP 525/50) for Alexa Fluor 488 emission detection; 00, 488000-0000-000 (excitation BP 530-585, beamsplitter FT 600, emission LP 615) for ND emission detection.

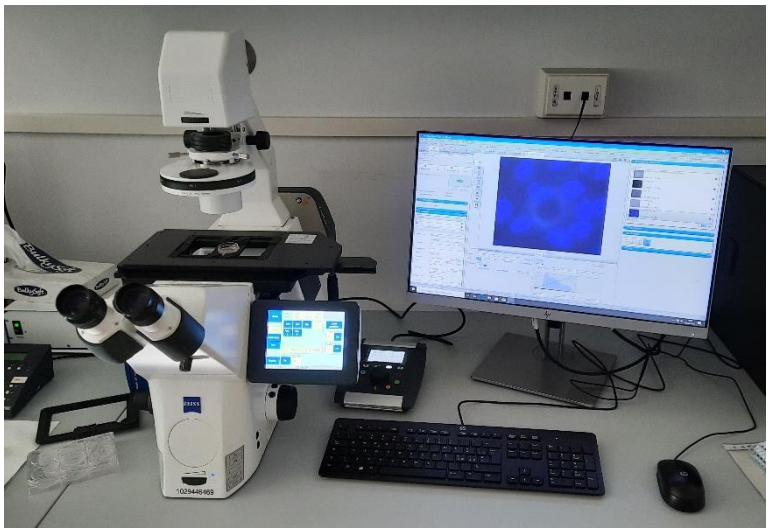

*Figure 34. Fluorescence microscopy setup.*

## Flow cytometry

Flow cytometry is a well-developed quantitative and qualitative analysis method used for counting and examining microscopic particles, i.e., entire cells, suspended in a stream of fluid [189]. In addition, it allows the analysis of cellular uptake for fluorescent NPs like quantum dots [190] or for particles

labelled by fluorescent dye [191]. Particularly, the usage of fluorescent NDs as cellular markers has been demonstrated using flow cytometry [192, 193].

In a flow cytometer, suspended cells and their contents flow individually through a volume illuminated by a light beam, usually laser light, where they scatter light and emit florescence. The emitted signal is collected, filtered and converted to digital values.

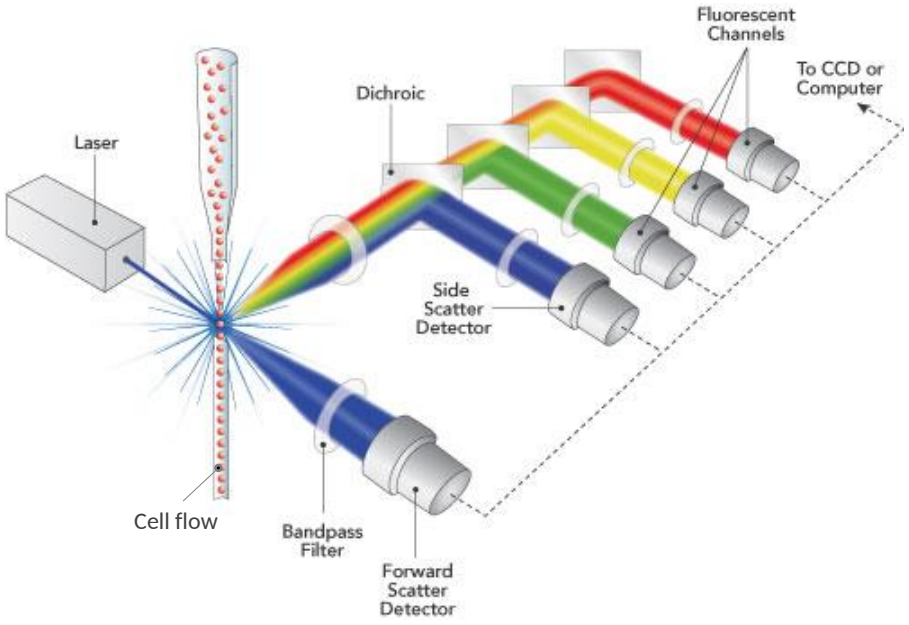


*Figure 35. Flow cytometer main elements and functioning [189].*

For the ND uptake analysis, MB cells, treated with different concentration of NDs (0 µg/ml, 20 µg/ml, 50 µg/ml, 100 µg/ml, 200 µg/ml, 400 µg/ml), were washed with PBS, harvested and fixed with 4% Paraformaldehyde in PBS for 10 min. The samples were analysed using a CytoFLEX flow cytometer (Beckman Coulter, Brea, CA, USA, Figure 36). The single-cell population was gated in a plot of forward scatter (FSC) vs. side scatter (SSC) after excluding cell debris and doublets and detected with a yellow-green 561 nm excitation laser and a 712/20 nm (red/infrared range) bandpass filter. Data were analysed using FCS Express 7 (De Novo Software, Pasadena, CA,

USA) and represented as the Median Fluorescence Intensity (MFI) normalized on the untreated controls.


*Figure 36. CytoFLEX flow cytometer.*

## Transmission Raman microscopy

Raman microscopy was used to detect the presence of NDs in the biological media and to obtain information on their distribution with respect to the cultured cells. Indeed, Raman mapping can produce direct information about the cellular ND localization. This technique provides the spatial distribution of the Raman signal, constituted by the Raman peaks that belong to specific compounds present in the sample under consideration. In particular, 2D Raman mapping was used to detect the unique and sharp Raman signature of the $sp^3$ diamond structure of NDs at 1332 $cm^{-1}$, and to obtain the positioning of NDs in cell cultures. The diamond Raman peak is an excellent marker since it gives unequivocal evidence of the presence of NDs based on their chemical and structural identification, differently from bright field and fluorescence techniques; therefore, this peak was used to study the internalization of 240 nm OX- and H-NDs in DAOY cells.

DAOY cells were plated on 20 mm glass-bottom cell culture dishes (NEST) and treated for 13 h with NDs. ND-treated cells were fixed with 4% Paraformaldehyde *w/o* methanol in PBS for 10 min, washed with PBS and left in PBS solution. The Raman setup employed for these measurements (available at the Fusion and Technology for Nuclear Safety and Security Department of the Italian National Agency for New Technologies, Energy and Sustainable Economic Development (ENEA) Casaccia Research Centre in Roma) is a homemade confocal system using 532 nm laser excitation (Figure 37). The laser beam is routed to the cells fixed in the cell culture dish via a microscope equipped with a 100× immersion objective and with a sample holder with computer-controlled positioning. The backscattered radiation is collected by the same objective. Then, the elastic component is removed by an edge filter and the surviving signal is fed to a 550 mm monochromator (Horiba-Jobin-Yvon TRIAX 550) matched with a liquid-nitrogen cooled CCD detector (Horiba-Jobin-Yvon CCD-3000) for dispersion and detection. Raman maps were collected using an acquisition time of 10 s and 3 averaged acquisitions per point with a position step of approximately 2 μm.

*Figure 37. Setup to obtain 2D Raman maps (Fusion and Technology for Nuclear Safety and Security Department of the ENEA Casaccia Research Centre).*

### 2.5.3 Cell irradiation

#### Gilardoni X-ray source

MB DAOY cells were irradiated with a Gilardoni CHF 320G X-ray generator (Figure 38) operated at 250 kVp, 15 mA, delivering doses of photons of 2 Gy, 5 Gy and 8 Gy, with a dose rate of 0.8 Gy/min. Six-well plates or 25 $cm^2$ flasks were irradiated in a horizontal position (radiation incident perpendicularly from above). DAOY cells were returned to the incubator at 37 °C immediately after exposure to radiation, before further processing.

*Figure 38. Gilardoni CHF 320G X-ray generator.*

### CALLIOPE γ-ray source

The γ-irradiations were conducted at the Calliope irradiation Facility [194], located in the ENEA Casaccia Research Centre (Figure 39). It consists of a pool-type irradiation plant equipped with a $^{60}$Co (mean energy 1.25 MeV) radio-isotopic source array in a high volume (7.0 m × 6.0 m × 3.9 m) shielded cell. The source rack is planar in shape, with 25 $^{60}$Co source rods (active area: 41 cm × 75 cm). MB DAOY cells were subjected to γ-radiation at a dose rate of 0.4 Gy/min with final absorbed doses of 2 Gy and 5 Gy, irradiating the well plates at a horizontal position. Even in this case, DAOY cells were returned to the incubator at 37 °C immediately after exposure to radiation and before further processing.

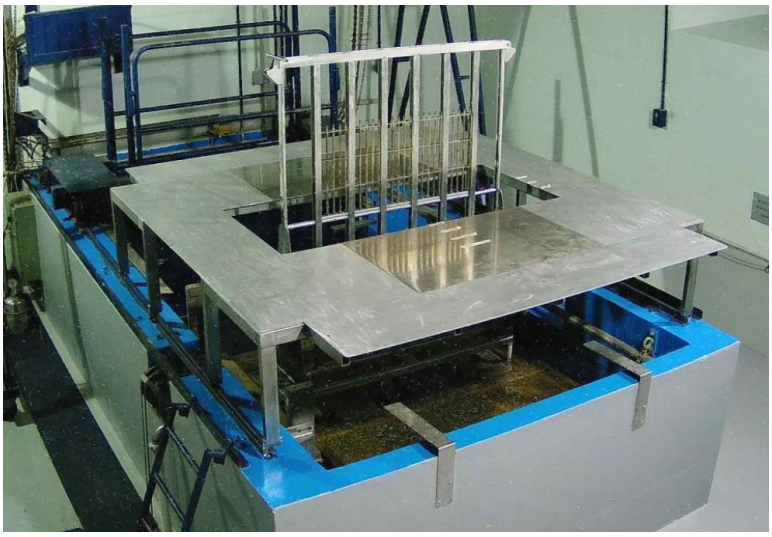

*Figure 39. Calliope irradiation Facility (ENEA Casaccia Research Centre).*

## 2.5.4 Clonogenic survival assay

Clonogenic assay is the gold-standard method for measuring the radiosensitivity of cancer cells. The day prior to initiating the MB cell treatment, a count of viable cells, using the trypan blue exclusion test, was

conducted. Subsequently, the DAOY cells were distributed into 6-well cell culture plates. Specifically, 100 viable cells were seeded per well for the sham group (unirradiated cells) and the 2 Gy irradiation group, 400 cells per well for the 5 Gy group, and 2000 cells per well for the 8 Gy group. Thirteen hours prior to irradiation, NDs were introduced into the culture medium. Just before subjecting the cells to irradiation, the medium was replaced with a fresh one devoid of NDs. Eight days after treatment, colonies were washed with PBS and fixed and stained with 1% crystal violet (Sigma-Aldrich, Wicklow, Ireland) solution/methanol (1:1). Colonies with >50 cells were counted; the ratio of the number of colonies to the number of cells seeded determined the plating efficiency (PE). The number of colonies that arise after treatment of cells, expressed in terms of PE, is called the surviving fraction.

### 2.5.5 DNA damage evaluation through flow cytometry analysis

For the γ-H2AX assay, DAOY cells were treated with combined treatment ND/γ-radiation as described above. Cells were washed with PBS, harvested and fixed with 70% ethanol solution at 30 min and 24 h after irradiation. Then, the cells were washed in Tris-buffered saline (TBS), pH 7.4, and suspended in 0.1% Triton X-100 in a 4% solution of foetal bovine serum (FBS) in TBS (TST) to suppress nonspecific Ab binding. At that point, DAOY cells were incubated for 2 h at room temperature with Phospho-Histone H2A.X (ser139) Rabbit Ab (Cell Signaling Technology, MA, USA) diluted 1:500 in TST and 45 min with F(ab')2-Goat anti-Rabbit IgG (H + L) Cross-Adsorbed Secondary Antibody, Alexa Fluor™ 488 (Invitrogen, Waltham, MA, USA), diluted 1:2000 in TST. Washes after each step were performed with a 2% solution of FBS in TBS. Finally, cells were suspended in 1 μg/ml of DAPI + 100 μg/ml DNase-free RNase A in TBS. Samples were analysed using a CytoFLEX flow cytometer (Beckman Coulter, Brea, CA, USA) with violet 405 nm and blue 488 nm excitation lasers and 450/45 (DAPI) and 525/40 (γ-H2AX) bandpass filters, respectively. Data were analysed using FCS Express

7 (De Novo Software). Cell population was gated in a plot of FSC vs. SSC to exclude cell debris and subpopulations were gated in a plot of SSC vs. 450/45 fluorescence intensity to identify cells in the G0/G1-, S- and G2/M- phases. For each cell cycle phase, the MFI at 525/40 was calculated separately and normalized, presenting the MFI per unit of DNA, by dividing the MFI of S- and G2/M-phase cells by 1.5 and 2.0, respectively. Data were represented as the MFI per unit of DNA normalized on the sham-irradiated untreated controls.

### 2.5.6 Bax and Caspase-3 analysis

#### Western blot

The western blot technique is often used in research to identify proteins. In this analysis, a mixture of proteins is separated based on molecular weight, and thus by type, through gel electrophoresis. The results are then transferred to a membrane producing a band for each protein, incubating the membrane with label antibodies specific to the protein of interest. The unbound antibody is washed off leaving only the bound antibody to the protein of interest, which is detected by developing the film. The intensity of the band corresponds to the amount of protein present, that can be quantified with respect to a defined standard [195].

In this work, MB cells were seeded in BioLite 25 $cm^2$ flasks (Thermo Scientific™, Wilmington, DE, USA) containing complete growth medium MEM and incubated 13 h with NDs. Before irradiation, the medium was discarded and the cells were washed with PBS, followed by the replacement of fresh medium. At 3 h post-irradiation, cells were rinsed with PBS and collected after trypsin digestion and centrifugation. The collected cells were treated with T-PER Tissue Protein Extraction Reagent (Pierce Biotechnology, Waltham, MA, USA) with protease inhibitors for protein collection and further quantification through Bio-Rad Protein Assay (Bio-Rad® Laboratories, Hercules, CA, USA). Proteins were separated on 10% pre-cast

gels (Mini-PROTEAN TGX Gels, Bio-Rad® Laboratories), transferred onto a 0.2 μm polyvinylidene fluoride (PVDF) membrane (Trans-Blot Turbo Transfer Pack, Bio-Rad® Laboratories) and blocked with 5% bovine serum for 1 h in Tris-buffered saline with 0.05% Tween®-20 (TBST). Membranes were incubated at 4 °C overnight with Anti-cleaved-Caspase 3 (ASP175) (5A1E) rabbit polyclonal antibody (Cell Signalling Technology®, Danvers, MA, USA) and Anti-Bax (ab7977) rabbit polyclonal antibody (Abcam, Cambridge, UK) in 3% bovine serum in TBST and for 1 h at room temperature with Anti-β-actin (#A5441) mouse monoclonal antibody (Sigma Aldrich, St. Louis, MO, USA) in 3% bovine serum in TBST. Subsequently, samples were further incubated with horseradish peroxidase (HRP)-conjugated anti-rabbit IgG and anti-mouse IgG for 1 h at room temperature. Specific proteins were visualized using ECL™ Prime Western Blotting Detection Reagent (RPN2232, Cytiva Marlborough, MA, USA) with iBright Imaging Systems and iBright Analysis software version 5.2.0.

## Real-time polymerase chain reaction (PCR)

The real-time PCR method is a variation of the PCR assay to allow monitoring of the PCR progress in actual time. PCR itself is a molecular process used to enzymatically synthesize copies in multiple amounts of a selected DNA region for various purposes. Currently, real-time PCR is one of the most powerful molecular approaches and is widely used in biological sciences and medicine because it is quantitative, accurate, sensitive, and rapid [196].

Here, MB cells were seeded in BioLite 25 $cm^2$ flasks containing complete growth medium MEM and incubated 13 h with NDs. Before irradiation, the medium was discarded and the cells were washed with PBS, followed by the replacement of fresh medium. At 3 h post-irradiation, cells were rinsed with PBS and collected after trypsin digestion and centrifugation. Total RNA was isolated from each sample using the mini RNeasy kit (QiaGen GmbH, Hilden,

Germany). RNA concentration and purity were determined by measuring absorbance using a NanoDrop 2000 Spectrophotometer (Thermo Fisher Scientific, Wilmington, DE, USA). A weight of 1 µg of total RNA was run on a 1% denaturing gel to verify RNA integrity. A weight of 1 µg of total RNA was reverse-transcribed using a IScriptTM cDNA Synthesis Kit (BioRad, Hercules, CA, USA). Real-time PCR was carried out using a BioRad CFX96 TouchTM Real-Time PCR Detection System using SsoAdvanced Universal SYBR Green super Mix (BioRad) and specific primers (see Table 2). The expression level of each mRNA was assessed using the ΔΔCT method, and Gadph was used as the housekeeping gene for normalization.

*Table 2. Specific forward and reverse primers for GAPDH and BAX.*

| **Primers** | |
|---|---|
| GAPDH forward | 5′-ATTCCACCCATGGCAAATTC-3′ |
| GAPDH reverse | 5′-GGGATTTCCATTGATGACA-3′ |
| BAX forward | 5′-TGGCAGCTGACATGTTTTCTGAC-3′ |
| BAX reverse | 5′-TCACCCAACCACCCTGGTCTT-3′ |

# 3 Results

This chapter is dedicated to the activity carried out by the candidate, concerning the characterization of nanodiamonds (NDs) with different chemical/physical properties (sizes, surface modifications, and ND concentration in solutions) and the study of their radiosensitizing capability.

Overall, three different batches of commercial NDs produced from the milling of High Pressure High Temperature (HPHT) type-Ib single crystals were investigated, namely:

- Pureon monocrystalline synthetic diamond (MSY) with average particle diameter equal to 18 nm (18 nm NDs);
- Pureon MSY NDs with average diameter around 55 nm (55 nm NDs);
- ElementSix™ Micron+ with average diameter around 240 nm (240 nm NDs).

The samples are shown in Figure 40: they appear as powders of light grey to black color.


*Figure 40. NDs used in the experimental activity, with different average diameters: (**A**) 18 nm (black powder); (**B**) 55 nm (dark grey powder); (**C**) 240 nm (light grey powder).*

The selected NDs allow investigating and comparing chemical/physical characteristics over a broad range of size distributions, providing an overview of the influence of ND dimensions on their radiosensitizing effects.

Thanks to the system detailed in section 2.2, ND samples underwent different annealing, oxidation and hydrogenation processes, whose sequences are detailed in the first section of this chapter.

## 3.1 Thermal treatment schemes

The schemes illustrated in Figure 41 summarize all the thermal processes performed on a given batch of NDs (18 nm, 55 nm and 240 nm NDs). The names given to the ND samples employed in the experiments are also shown in each scheme.

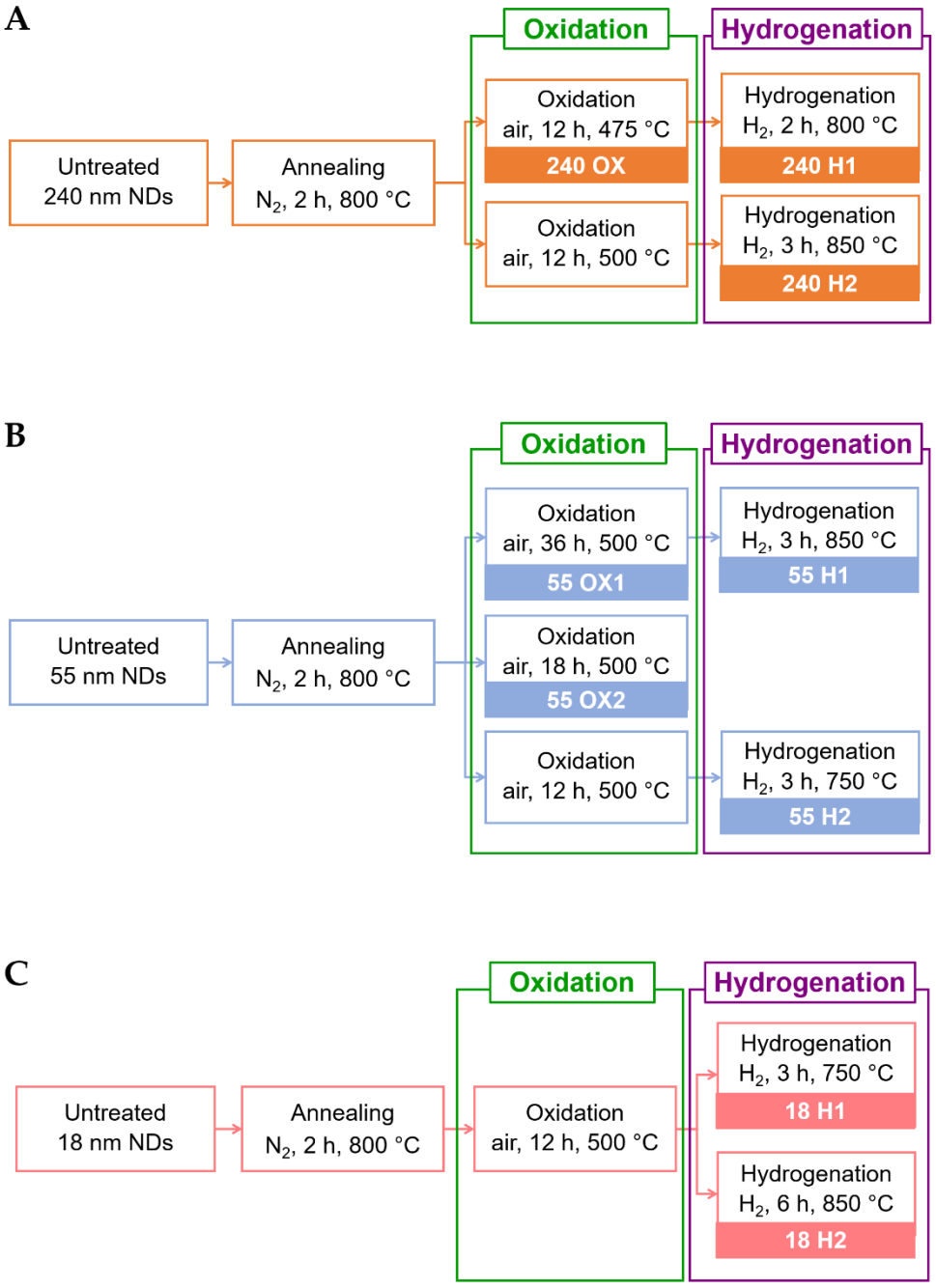


*Figure 41. Summary schemes for the different processing steps of the thermal treatments conducted on NDs, with the name labels chosen to indicate each batch of NDs employed for the experiments. (**A**) Thermal treatments carried out on 240 nm NDs. (**B**) Thermal treatments conducted on 55 nm NDs. (**C**) Thermal treatments performed on 18 nm NDs. The names of the processes are reported inside the white rectangles, whereas the arrows indicate their sequence. The labels given to ND samples are inside the colored rectangles.*

NDs were investigated in their different versions using several characterization techniques and the obtained results are described in the following section.

## 3.2 ND characterization

The different batches of NDs were studied and compared in terms of their chemical/physical properties, to determine the modifications induced by thermal treatments. The results of Diffuse Reflectance Infrared Fourier-Transform (DRIFT) spectroscopy (paragraph 3.2.1), Raman and photoluminescence spectroscopies (paragraph 3.2.2), and Dynamic Light Scattering (DLS) analysis (paragraph 3.2.3) are presented here, while chapter 2 already reported a detailed description of the instrumentation used for the characterization and the analysis methods.

### 3.2.1 DRIFT spectroscopy

DRIFT analysis was carried out to suitably identify the functional groups on ND surface, further confirming the thermal treatment efficacy in the formation of oxygenated groups (oxidized- or OX-NDs) and hydrogen terminations (hydrogenated- or H-NDs). Indeed, the surface chemical characterization of NDs has crucial importance, providing useful indications to better understand ND behavior in water and biological solutions.

Figure 42 reports the DRIFT spectroscopy results for the modified NDs (for details on the treatments, see the schemes in Figure 41).

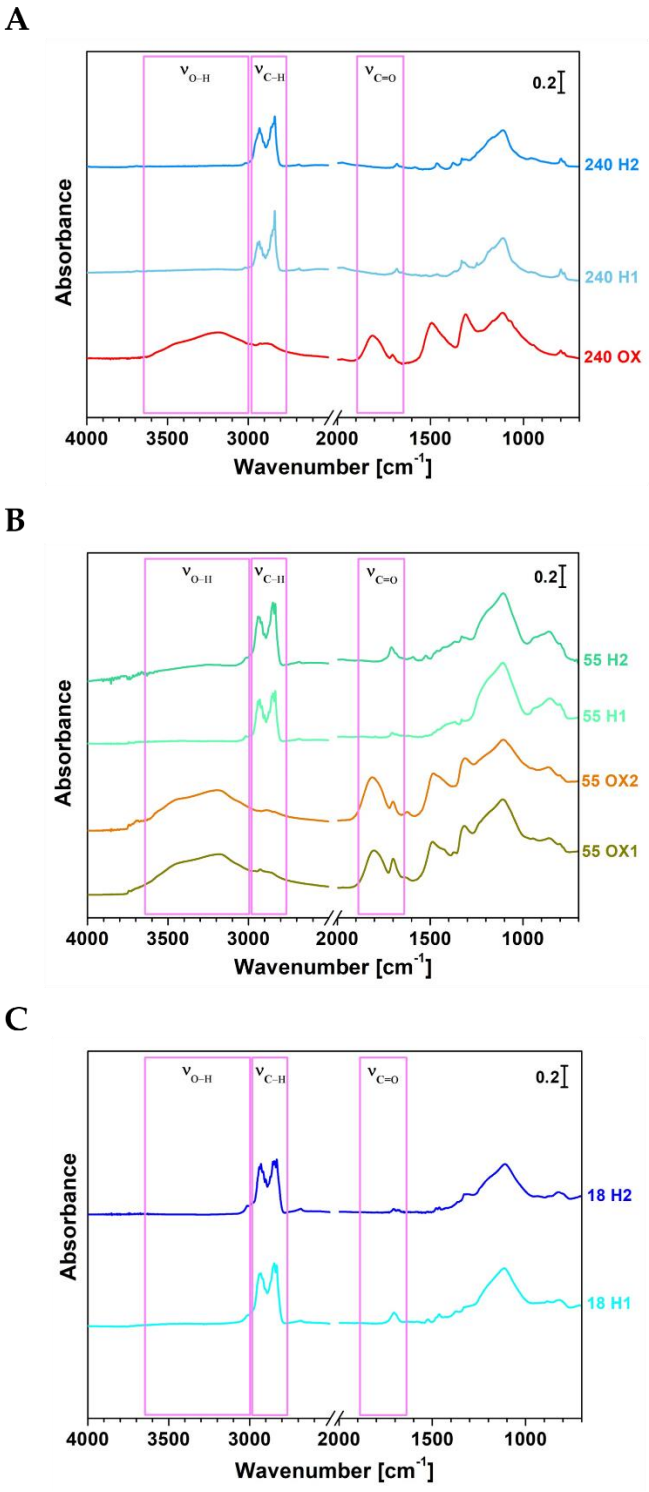


*Figure 42. DRIFT spectra of the thermally treated OX- and H-NDs (spectra acquired in controlled atmosphere at room temperature). (**A**) 240 nm ND spectra. (**B**) 55 nm ND spectra. (**C**) 18 nm ND spectra. The labels given to the samples are the same reported in the schemes of Figure 41. The regions of O–H ($\nu_{O-H}$), C–H ($\nu_{C-H}$) and C=O ($\nu_{C=O}$) stretching are marked with pink rectangles.*

The spectra of OX-NDs reveal significant signals associated with the presence of oxygen-containing functionalities on ND surface (such as hydroxyls, carboxylic acids, esters, etc.). They all exhibit bands within the 1850 $cm^{-1}$ - 1650 $cm^{-1}$ spectral region, corresponding to C=O stretching ($\nu_{C=O}$), and a broad band in the 3650 $cm^{-1}$ - 3000 $cm^{-1}$ range, indicative of O–H stretching modes ($\nu_{O–H}$) [197, 198, 199]. Moreover, the surface groups introduced following the oxidation thermal treatment are responsible for the appearance of spectral features in the 1500 $cm^{-1}$ - 1300 $cm^{-1}$ region, typical of ketones and epoxides vibrations [197, 200]. By this results, the DRIFT analysis experimental evidence not only confirm the success of the oxidation processes, but also underscore the high hydrophilicity of OX-NDs [147, 160, 169], as the $\nu_{O–H}$ stretching band is also influenced by the presence of surface-adsorbed water [197, 198]. Indeed, as already discussed, surface chemistry has a relevant influence on the hydrophilicity profile of nanoparticles (NPs) and this property can be evaluated by considering the intensity of the $\nu_{O–H}$ modes, which are generally more intense in the cases of OX-samples. In addition, the high water affinity of the oxygenated chemical species decorating the OX-ND surface facilitates their solubility and reduces their aggregation.

In contrast, the spectra of H-NDs exhibit prominent features in the 2990 $cm^{-1}$ - 2800 $cm^{-1}$ range, associated with a strong C–H stretching ($\nu_{C–H}$) [197, 198]. These spectra lack the $\nu_{O–H}$ signal and show a progressive decrease or disappearance of carbonyl-related fingerprints, as the strength of the hydrogenation treatment increases (longer thermal treatment duration or higher temperature). Additionally, the suppression of a part of the spectral features in the range below 1500 $cm^{-1}$ is observable. Therefore, the H-ND DRIFT spectra also confirm the efficacy of the hydrogenation treatment in forming hydrogen terminations, while simultaneously removing oxygenated functional groups, turning the surface from hydrophilic to hydrophobic [147, 160, 198]. Actually, the lower H-ND water-affinity is highlighted by the

absence of relevant features in the 3650 $cm^{-1}$ - 3000 $cm^{-1}$ spectral range and by the parallel drastically decreased intensity of the $\nu_{C=O}$ band.

In the case of 18 nm NDs, the attention was focused on the hydrogenation treatment, fundamental in the context of this thesis, and the characterization spectra of both the samples (18 nm H1- and 18 nm H2-NDs) will be shown in the following discussion. Nevertheless, these spectral data confirm that the treatment at higher temperature (18 H2) is more effective compared to the one at 750 °C (18 H1) in removing completely oxygen-containing terminations from ND surface. This is noticeable from the almost complete disappearance of the band linked to carbonyl group-containing moieties at ~ 1700 $cm^{-1}$ [197] in 18 H2 spectrum. Hence, 18 H2-NDs are more hydrophobic.

Concerning 55 nm and 240 nm NDs, due to the similarity of the DRIFT spectra of the samples with comparable final thermal treatment, in the next paragraphs the characterization results of a single type of ND (one for oxidation process and one for hydrogenation treatment) will be shown for each ND dimension. It is noteworthy that the intensity of the bands associated with the $\nu_{O-H}$ and $\nu_{C=O}$ stretching in the OX-NDs, and with the $\nu_{C-H}$ stretching in the H-NDs, is nearly identical when comparing spectra based on treatment type (oxidation or hydrogenation), while examining ND groups with equivalent average diameters. Sample name labels will always be specified according to those in Figure 41, allowing unambiguous identification.

### 3.2.2 Raman and photoluminescence spectroscopy

Figure 43 shows photoluminescence spectra from all the ND dimensions. They all exhibit a broad band spanning the range between 600 nm and 780 nm, associated with the phonon sideband of nitrogen-vacancy (NV) centers. In some cases (mainly for OX-NDs), weak features at $\lambda$ = 575 nm and $\lambda$ = 638 nm are also observable and can be attributed, respectively, to the zero-phonon line (ZPL) signals of $NV^0$ and $NV^-$ centers [123] (see paragraph 1.3.4).

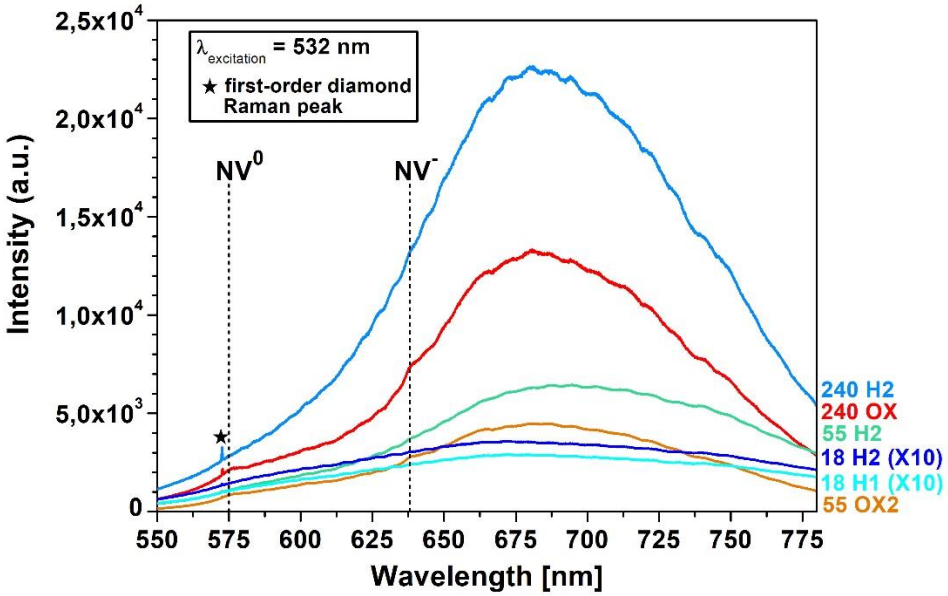


*Figure 43. Photoluminescence spectra of the OX- and H-NDs. $NV^0$ and $NV^-$ ZPLs are marked with black dashed lines. A black star evidences the Raman first-order peak of diamond, appearing at ~572.5 nm. Measurements were conducted on compacted ND powders; objective 20×; filter D1 [169]. The spectra labelled as "18 H1" and "18 H2" (referred to the 18 nm NDs, see Figure 41) were multiplied by 10 to render them visible on the same scale as the other ones [201].*

Notably, ND fluorescence detected through photoluminescence spectroscopy reveal that the spectrum intensity is directly correlated to ND size. Specifically, the photoluminescence intensity in 240 nm NDs, characterized by a larger diamond core, with a higher number of NV centers, exceed that of 55 nm NDs by approximately one order of magnitude and is greater of about two orders of magnitude compared to that characterizing 18 nm NDs. The observed phenomenon is also associated with a more relevant presence of surface graphite on smaller NDs, in accordance with the findings by Smith *et al.* [202]. They demonstrated that surface graphitic content has a quenching effect on the luminescence of NV centers. Therefore, the reduced photoluminescence of smaller NDs may be both attributed to their smaller diamond core size and to the potentially higher presence of graphitic phases on their surface.

It is also worth highlighting that the spectral feature at ~ 572.5 nm, appearing for all the samples, is not the result of a photoluminescence effect. Instead, it is the first-order Raman peak of diamond, corresponding to the Raman shift value of 1332 $cm^{-1}$ [104]. This peak can be more easily appreciated in the ND Raman spectra, reported in Figure 44, and evidences that the thermal processes in air and hydrogen atmosphere did not undermine ND diamond core.

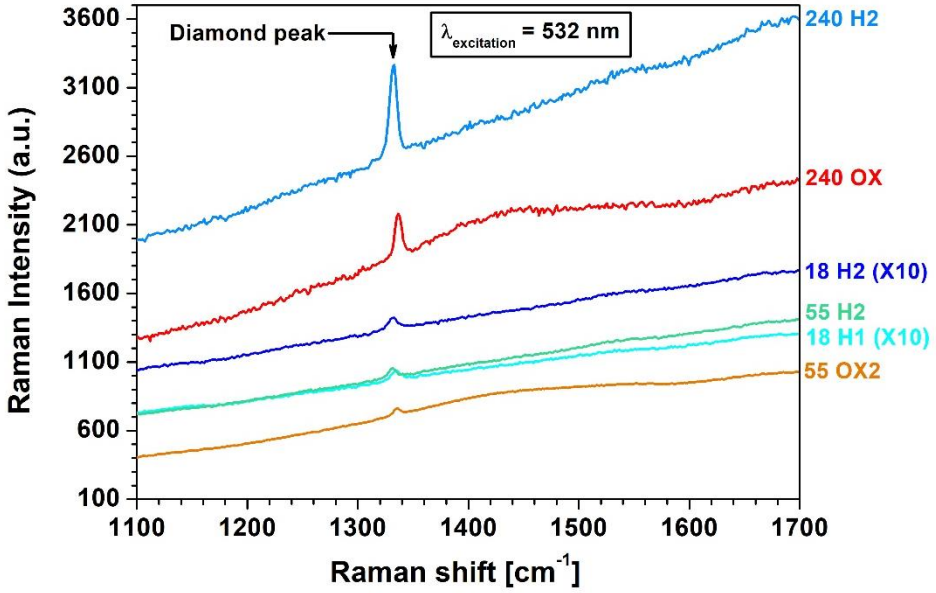


*Figure 44. Zoom of the main Raman features of the OX- and H-NDs. The black arrow evidences the position of the Raman first-order peak of diamond, appearing at ~ 572.5 nm. The spectra labelled as "18 H1" and "18 H2" (referred to the 18 nm NDs) were multiplied by 10 to render them visible on the same scale as the other ones [201].*

## 3.2.3 DLS analysis

The dispersion level of ND suspensions at 10 μg $ml^{-1}$ in phosphate-buffered saline (PBS) solutions were evaluated by means of DLS analysis.

Figure 45 shows the ND size distributions by number. In general, the higher water affinity of the oxygenated chemical species decorating the

surface of the OX-NDs facilitates their solubility and reduces their aggregation. These observations can be explained with the marked hydrophilic character of OX-ND surface, evidenced in the DRIFT spectra of Figure 42.

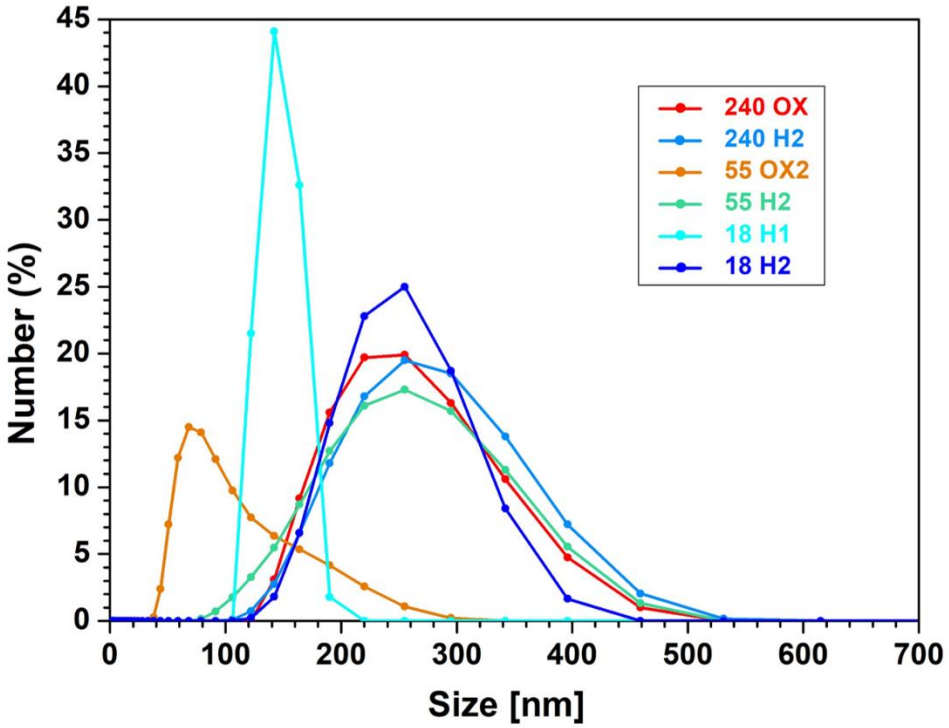


*Figure 45. DLS size distribution of ND samples by number (ND concentration = 10 μg ml$^{-1}$).*

On the other hand, due to aggregation phenomena, H-NDs present higher size values, suggesting poor dispersibility and pronounced agglomeration tendency. This is interpreted based on the higher H-ND hydrophobicity, as confirmed by DRIFT analysis. Interestingly, the aggregation trend appears inversely proportional to the average diameter of the particles. Indeed, while the 240 nm OX- and H2-NDs are characterized by similar size distributions, the 55 nm and 18 nm H-samples present a severe aggregation level, particularly pronounced in the smaller NDs. The aggregation also depends on the intensity of the hydrogenation treatment. This is not unexpected, because

of the wider interaction surface of 18 nm samples. Therefore, DLS measurements emphasized the hydrophilicity of OX-NDs, compared to H-ND hydrophobicity.

After ND characterization, the experiments aimed at investigating H-NDs as radiosensitizers are described in the next sections of this thesis.

## 3.3 ND effects on hydroxyl radical production in PBS solutions following irradiation

In the first chapter, the potential application of H-NDs for the enhancement of free radical generation in radiotherapy (RT) was discussed. Here, the measurements of the production of hydroxyl radical (•OH) following the photon irradiation of ND solutions are illustrated.

As detailed in section 2.4, NDs were added into terephthalic acid (TPA) PBS-based solutions, irradiated and analysed by spectrofluorimetry analysis. Conceptually, following the reaction with the •OH radicals generated by water-radiolysis, TPA converts to a fluorescent product: the 2-hydroxyterephthalic acid (HTPA). HTPA emits at wavelength $\lambda \sim 430$ nm, when excited with $\lambda \sim 310$ nm. Accordingly to literature [168, 203], an increase in the fluorescence signal is expected in presence of irradiated H-ND solutions, with H-NDs boosting the •OH radical production, in turn resulting in a higher quantity of produced HTPA.

However, before discussing the data with NDs, some preliminary experiments were completed to define a protocol for •OH radical detection in solutions.

### 3.3.1 Preliminary measurements with TPA solutions

Firstly, the evaluation of the •OH radicals created at different irradiation times (i.e., different doses) was performed with the experimental setup described in paragraph 2.4.1 and developed by the candidate. In particular, 0.2 mM TPA solutions were irradiated through the microfocus X-ray source (paragraph 2.4.2), varying the irradiation time from 1 min to 10 min. Figure 46 shows a linear increase of the mean area of the HTPA peak ($A_{mean}$) as a function of the irradiation time (see section 2.4 in chapter 2 for details on the fluorescence spectra analysis).

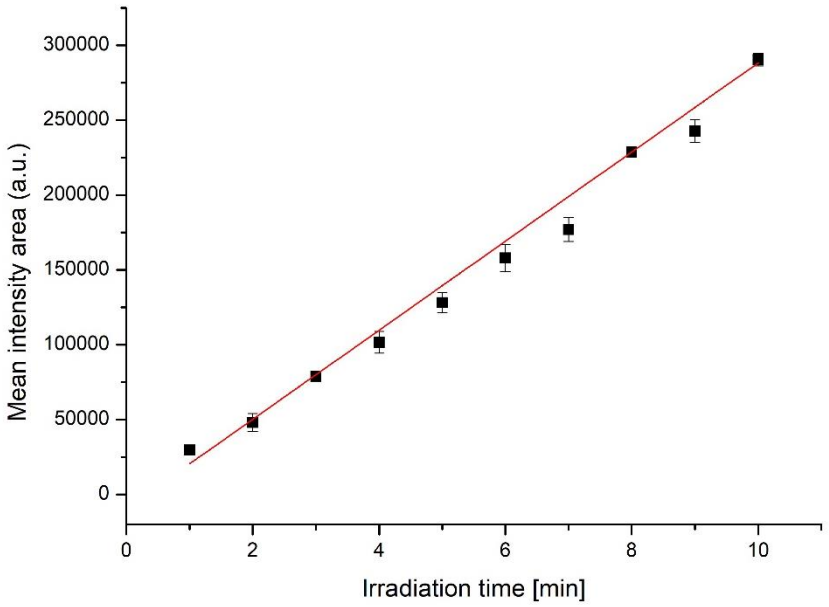


*Figure 46. Mean area of the HTPA peak at different irradiation times for 0.2 mM TPA solutions. Values are represented as mean ± SEM (standard error of the mean). The dataset follows a linear trend highlighted by the fitting curve in red:* $A_{mean} = (-9000 \pm 2000) + (29800 \pm 300)\ t$*, where* $t$ *is the irradiation time.*

For the subsequent experiments, a standard irradiation time of 6 min was chosen, as the shortest irradiation duration that simultaneously allowed a good ratio between the intensity of the recorded signal and the electrical noise.

### 3.3.2 HTPA calibration curve

After defining the parameters for irradiating the TPA probe, it was necessary to comprehend how many •OH radicals could be detected in solutions of known TPA concentration, by matching an •OH quantity to the HTPA fluorescence intensity obtained following irradiation. To asses this calibration associated to the TPA/HTPA conversion, HTPA powder was solved in PBS and fluorescence spectra of these solutions were acquired, varying HTPA concentration from 0.05 µM to 0.6 µM. This concentration range was chosen to cover the interval of the HTPA peak intensities usually detected after irradiation. The evaluation of the •OH radicals was done powering the UV-visible led with a current of $I$ = 15 mA (current adopted during the experiments with NDs) and the dataset is reported in Figure 47.

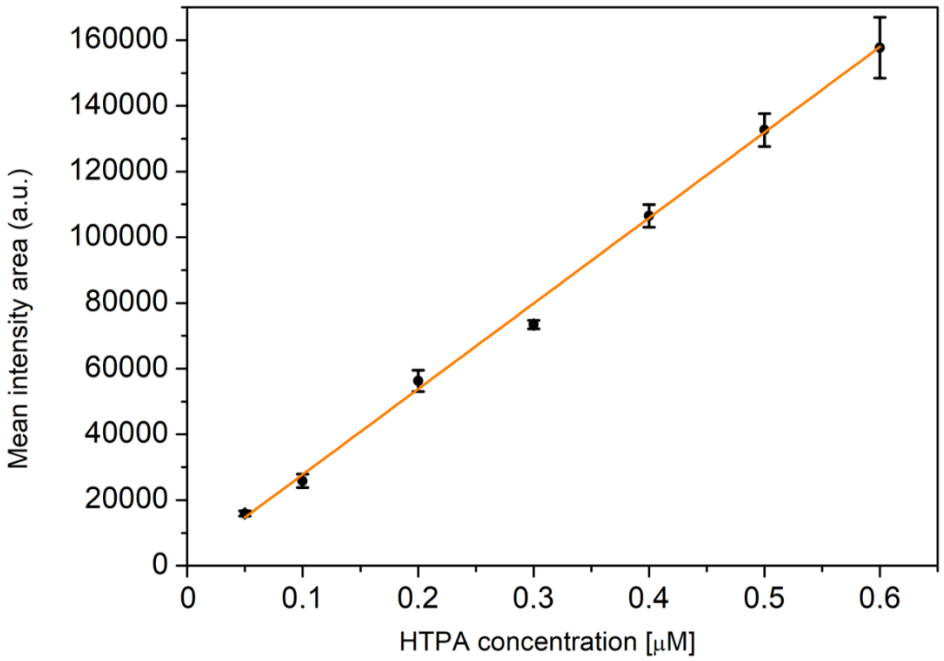


*Figure 47. HTPA calibration curve: evaluation of the $A_{mean}$ of the fluorescence peak, varying HTPA concentration in the solution. Values are represented as mean ± SEM. Data are interpolated with a linear fit: $A_{mean} = (2000 \pm 2000) + (260000 \pm 5000)\, C$, where $C$ is the HTPA concentration.*

By increasing HTPA concentration inside the PBS solution, the $A_{mean}$ value grows linearly. In particular, the number of •OH radicals can be established using the linear fit equation:

$$A_{mean} = (2000 \pm 2000) + (260000 \pm 5000)\, C$$

where $C$ is the HTPA concentration in the solution. Assuming that all •OH radicals formed during irradiation are reacting with TPA, it is possible to evaluate the number of •OH radicals by using the equation above and measuring the area of the fluorescence peak of HTPA.

After these preliminary measurements, NDs were added to TPA solutions to study their effects on •OH production following photon beam irradiation. To test the interplay of ND chemical/physical properties in radiolysis experiments the microfocus X-ray source located at the Physics Department of the University of Torino (already mentioned in this section and in paragraph 2.4.2 of the previous chapter), operated at 130 kVp, was employed. The results are described in the next paragraph.

### 3.3.3 •OH radical production in ND/TPA solutions after X-ray irradiation

In this first measurements with NPs, the 55 nm and 240 nm NDs in the OX- and H1-forms were analysed (thermal treatments described in Figure 41A and B). In particular, the candidate considered the largest ND sizes among those available, already well characterised for their use in preceding works [147, 169], and conducted experiments on H-NDs, comparing their effect with respect to OX-NDs and solutions without NDs (TPA in Figure 48; for details on the data analysis refer to section 2.4 in the previous chapter).

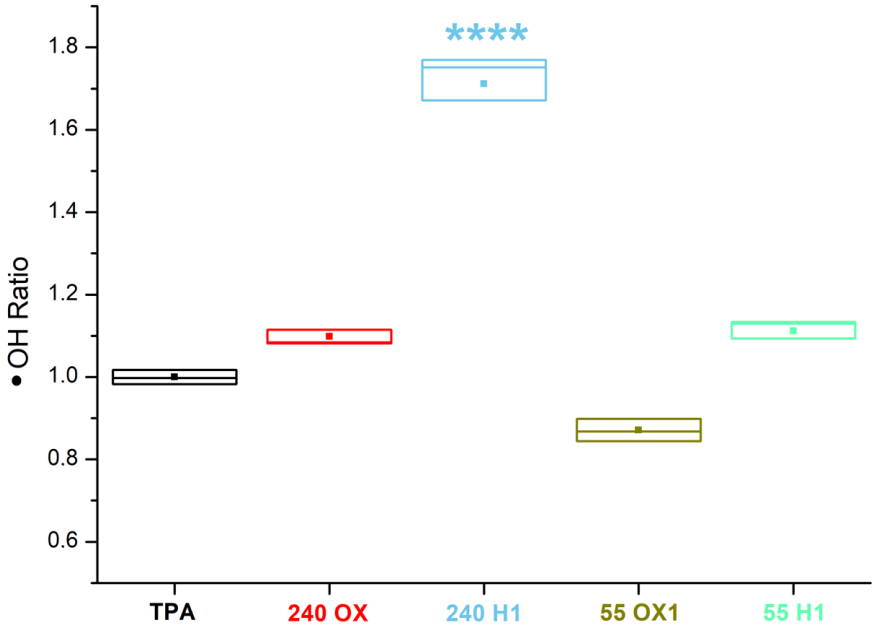


*Figure 48. •OH radical concentration in the ND/TPA solutions (TPA concentration = 0.05 mM, ND concentration = 10 µg/ml) after 130 kVp X-ray irradiation. Data are normalized to the mean of the samples containing only the TPA probe. The standard error on the mean determines each box. Inside each box, the solid squares and the horizontal lines represent the mean and median values, respectively. All experiments were performed on at least 9 replicates. One-Way ANOVA tests with the Tukey's multiple comparison tests were performed between the different samples and TPA. The* p-*values ≤ 0.05 (*) and ≤ 0.01 (**) were considered as statistically significant;* p-*values ≤ 0.001 (***) and ≤ 0.0001 (****) were considered as highly statistically significant.*

The first finding was that 240 H1-ND solutions, compared to only-TPA ones, show a statistically significant increase in the number of radicals after 130 kVp X-ray irradiation. On the other hand, 55 H1-NDs only present a trend towards an increase in radical concentration that, in these conditions, is not significant. Considering OX-NDs, they present no effect (240 OX) or induce a mild reduction in the •OH radical concentration (55 OX1), that however is not statistically significant.

Therefore, two alternative hypotheses, not necessarily unrelated, could be proposed to explain the OX-ND opposite behaviour with respect to H-NDs, with the latter enhancing the radiation-induced •OH production. On one hand, the electrons are emitted by the H-NDs and are sufficiently energetic to

generate secondary radiolysis, or the H-ND overproduction is based on interfacial processes. In the former case, the difference between H-NDs and OX-NDs can be ascribed to their different surface chemistries (hydrogen terminations for H-NDs versus oxidized terminations for OX-NDs). Following excitation by radiation, the negative electron affinity of H-NDs could promote the transfer doping of electrons from the valence band to the redox species in the solution. The second hypothesis is linked to the key role that water molecules at the nanoparticle interface could play in the production of radicals. Indeed, for NDs, considering the mass energy absorption coefficients of carbon and water, we do not expect a drastic increase in the energy deposition in correspondence with these NDs. However, it has been documented that, following ND water dispersion, water molecules adsorb more strongly on H-NDs with respect to OX-NDs, due to the presence of a hole accumulation layer on the former, leading to a higher amount of water on H-NDs despite their hydrophobicity [169, 204]. Furthermore, by combining infrared, Raman and X-ray absorption spectroscopies, Petit et al. revealed different structures of water molecules surrounding the NDs, varying the surface chemistry [205]. In particular, the hydrogen-bonding network of water was found to be different in aqueous dispersions of H-NDs compared to OX-NDs, leading to long-range disorder of the water molecules and electron transfer in the shell of H-ND hydration. Thus, a difference in water disposition could also be responsible for the different behaviours of H-NDs and OX-NDs under irradiation [203].

Consecutively, further investigating the promising results highlighted by H-NDs, their radiosensitizing effects were analysed *in vitro*, taking care of another important variable: the irradiation energy.

## 3.4 ND effects following *in vitro* irradiation

After the study of the effects on •OH radicals in solution, the candidate tested the potential efficacy of NDs of different sizes and surface modifications in radiosensitizing a human radioresistant medulloblastoma (MB) cell line (DAOY HTB-186). As mentioned in chapter 1, it has been proven that the use of radiosensitizing nanoscale materials can improve the radiation sensitivity of cancer cells and reduce RT adverse consequences. Also here, NDs are examined as radiosensitizers in combination with photon irradiation at different energies.

However, a characterization of ND behavior in the DAOY cellular environment was indispensable, and, first of all, the cellular uptake and distribution of NDs in DAOY cells was investigated. All the *in vitro* measurements were performed at the Laboratory of Biomedical Technologies of the Casaccia Research Centre (Roma) of the Italian National Agency for New Technologies, Energy and Sustainable Economic Development (ENEA).

### 3.4.1 ND internalization and cellular distribution

#### Fluorescence microscopy

In the last decades, due to their bright fluorescence and high photostability with sufficiently long lifetime, NDs emerged as efficient markers for cellular imaging and to date there are a number of publications showing the exploitation of ND fluorescence for imaging, mostly in the cells [84, 85, 115, 125, 126].

In this thesis work, the cellular uptake of H- and OX-NDs of different median diameters was investigated, exploiting the fluorescence properties of their NV centers. Indeed, both of these ND variants emit red fluorescence in

the region between 550 nm and 800 nm upon excitation at wavelengths in the green region (around 532 nm) [115]. In particular, the fluorescence imaging technique was employed to qualitatively analyse the localization and internalization of NDs in the MB DAOY cells. The same NDs with average size of 18 nm, 55 nm and 240 nm, specified in the schemes of Figure 41, were used.

Figure 49 shows fluorescence images of DAOY cells, with an overlay of NDs (red), cell nuclei (DNA, blue) and cell cytoskeleton (F-actin, green) emission signals. The representative images of the distribution of OX- and H-NDs are compared to the ND-untreated control (CTR).

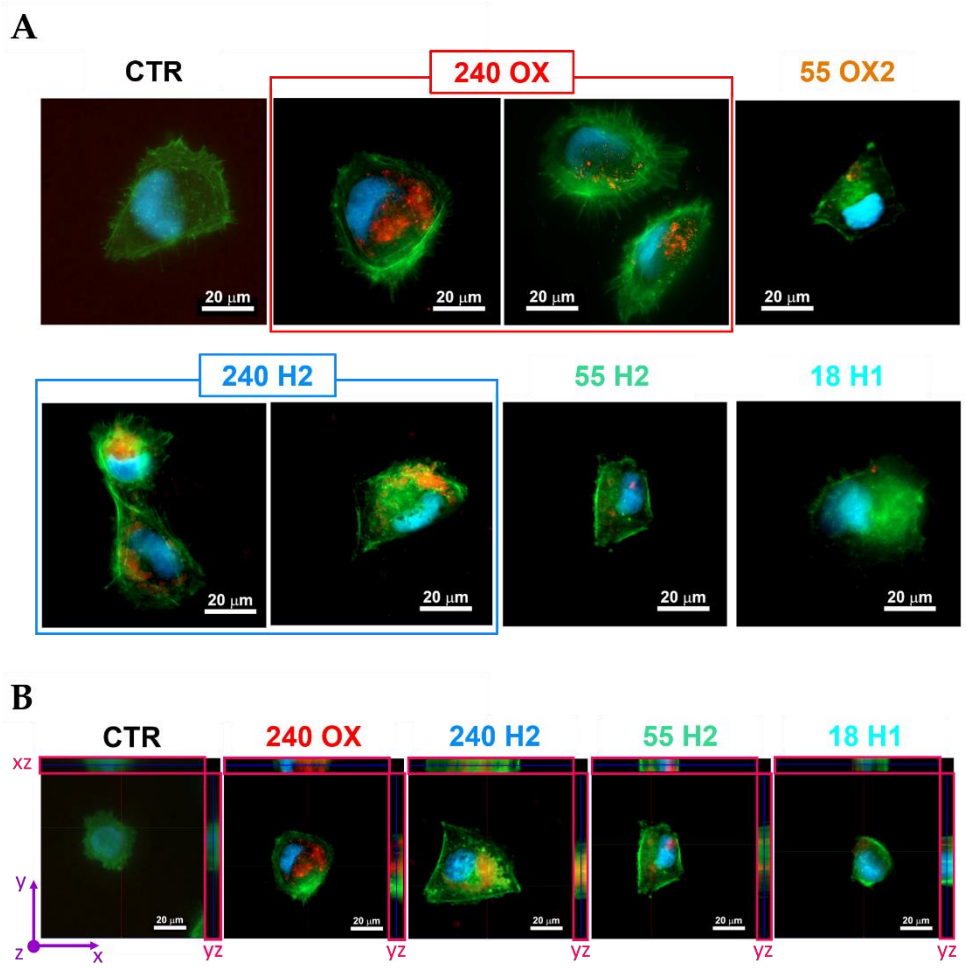


*Figure 49. Qualitative analysis of the ND uptake by DAOY cells through fluorescence microscopy (adapted from [201]). (**A**) Comparison of DAOY cells after 13 h incubation at 37 °C, respectively, without NDs (CTR) and with 240 nm OX-NDs, 55 nm OX2-NDs, 240 nm H2-NDs, 55 nm H2-NDs and 18 nm H1-NDs (for sample labels see Figure 41), at a particle concentration of 20 µg ml$^{-1}$. The images show the fluorescence signal of NDs in red overlapped with the stained nuclei in blue (DAPI DNA staining) and cell cytoplasm in green (Phalloidin staining). The scale bar is 20 µm. (**B**) Cross-sectional fluorescence images of some treated and untreated (CTR) DAOY cells for ND intracellular localization. These images show the cells in the xy plane, as indicated by the Cartesian axes in purple (with the z axis directed coming out of the sheet), while the sections of the xz and yz planes are collected in the centre of the cell and boxed in pink, respectively (section thickness = 7.98 µm, divided in 15 slices).*

In line with the observations made by Fu *et al.* [206], both OX- and H-NDs are primarily localized in the perinuclear cytoplasmic region. However, a difference emerged when comparing their intracellular distributions. OX-

NDs exhibited an even dispersion throughout the cytoplasm, while H-NDs displayed a tendency to cluster, particularly noticeable in images of cells treated with 240 nm NDs that are more readily detectable through fluorescence. The lower ND signal for 55 nm and 18 nm NDs is due to fluorescence intensity dependence on the ND size and not on differences in ND uptake. The differing intracellular localization between H-NDs and OX-NDs can be attributed to the hydrophobic nature of H-NDs, making them more prone to adherence to cell membranes and generally to aggregation, as experimentally verified by the DLS analysis (paragraph 3.2.3). Conversely, OX-NDs, with their hydrophilic surface and carboxylic groups, tend to disperse throughout the cytoplasm. The distinct behaviours of H-NDs and OX-NDs in the biological context may also suggest a higher degree of interaction of H-NDs with the plasma membrane and various organelles. Furthermore, always in line with DLS analysis, larger NDs displayed a reduced level of aggregation when compared to their smaller counterparts, such as the 18 nm NDs. This observation aligns with the understanding that aggregates typically form due to stronger Van der Waals interactions, which are more pronounced when the nanomaterial size is smaller [207].

Additionally, the internalization of ND variants was confirmed by a series of vertical cross-sectional fluorescence images of ND-treated cells (Figure 49B).

### Flow cytometry

Flow cytometry was employed to evaluate both the influence of ND concentration on their internalization and the dependence of ND uptake on the incubation time. Figure 50 shows that the intensity of the ND fluorescence signals increases proportionally to their concentration, reaching the maximum at the highest concentration (400 µg/ml).

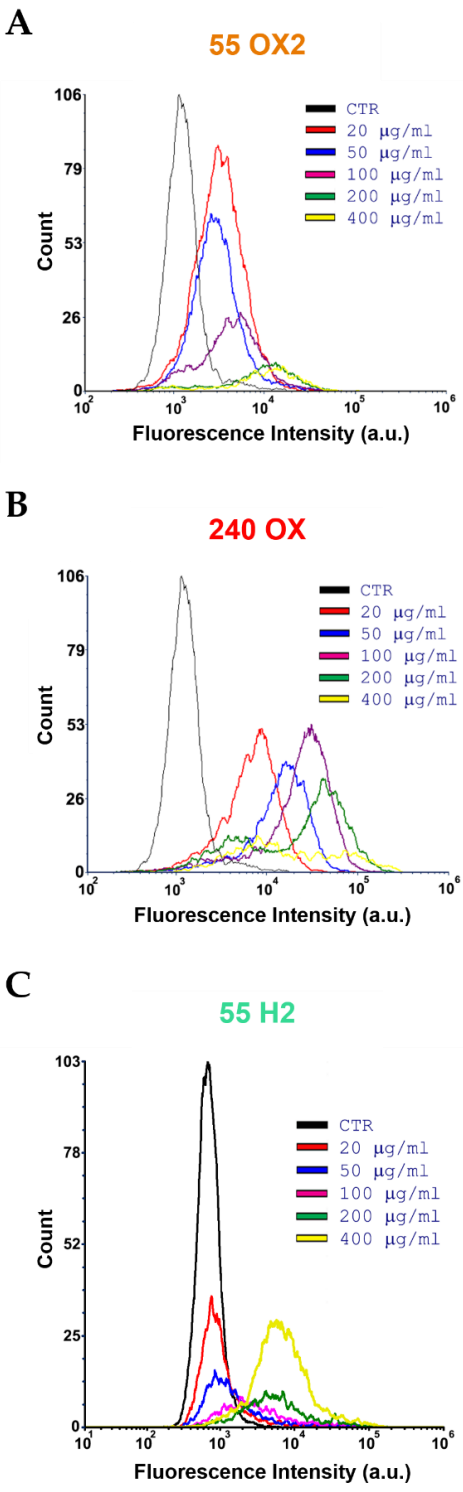


*Figure 50. Analysis of the cellular uptake of NDs by DAOY cells through flow cytometry (10000 cells analysed, adapted from [201]): MB cells treated with different concentrations of (**A**) 55 nm OX2-NDs, (**B**) 240 nm OX-NDs and (**C**) 55 nm H2-NDs. Relative fluorescence intensity in the 712/20 channel is reported in the x-axis while the y-axis reports the number of events (count).*

The uptake kinetic showed good internalization as well as retention in MB cells, as presented in Figure 51 and in line with the kinetic properties of other NPs [208, 209]. Indeed, the internalization process increased with the incubation time with a saturation point at 9 h post-administration, when the uptake reached a plateau.

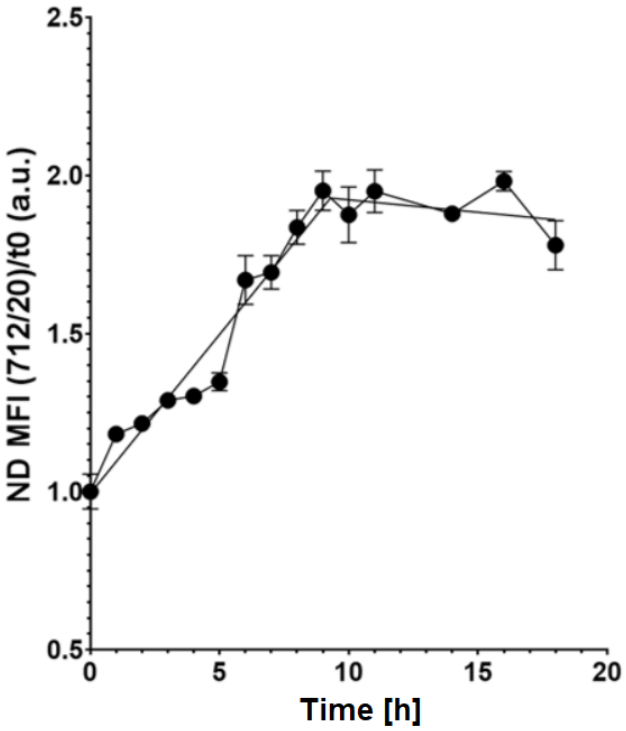


*Figure 51. Analysis of the cellular uptake of NDs by DAOY cells through flow cytometry: uptake curve for 20 µg/ml 240 nm H2-NDs represented as the ND Median Fluorescence Intensity (MFI) detected with a 712/20 nm bandpass filter and normalized to the untreated controls. Values are represented as mean ± SEM (adapted from [201]).*

Hence, 13 h was selected as an appropriate incubation time for the subsequent experiments.

## Raman microscopy

In addition to fluorescence imaging, the results obtained using Raman mapping provided valuable information about the distribution of NDs in

DAOY cell cultures (Figure 52 and Figure 53). The diamond Raman peak was indeed utilized to investigate the internalization of 240 nm OX-NDs and H2-NDs in DAOY cells. For this purpose, NDs were incubated at a concentration of 20 µg/ml for 13 h, and two representative bright-field images of DAOY cells with OX- and H-NDs were captured (Figure 52A and Figure 53A).

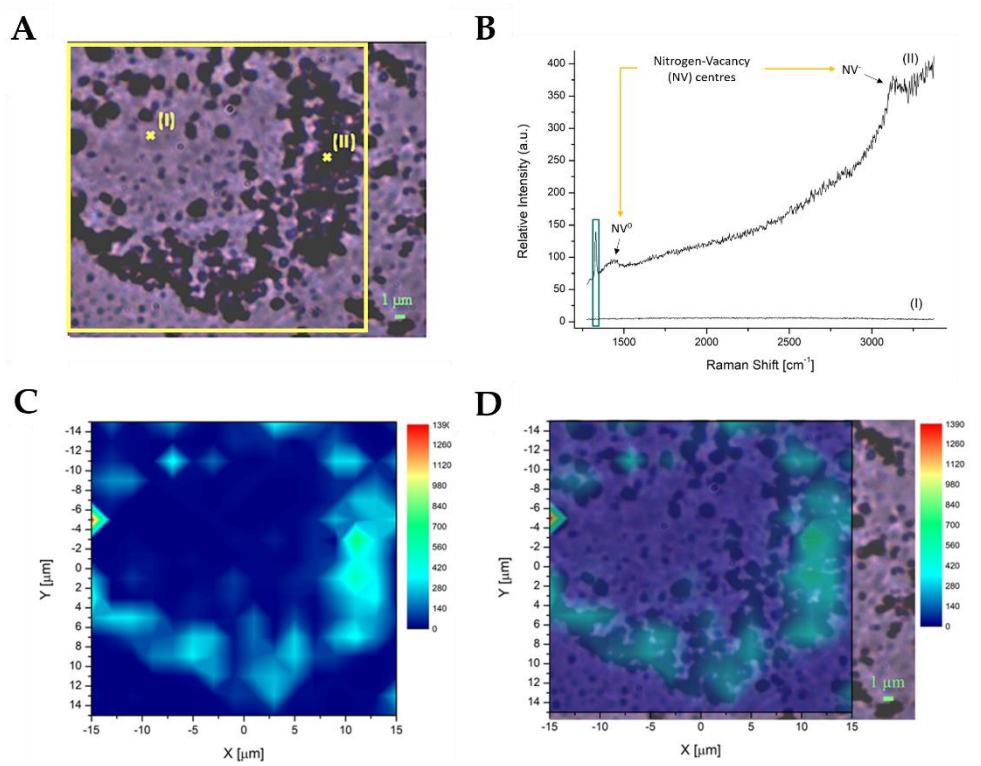


*Figure 52. OX-ND localization in DAOY cell cultures using Raman mapping (adapted from [201]). (**A**) Bright-field image of a cell incubated with 20 µg ml$^{-1}$ of 240 OX-NDs. The yellow square represents the area considered for mapping (scale bar 1 µm). (**B**) Raman spectra measured in point (I) and (II) in (**A**), showing the typical first-order diamond Raman peak around 1332 cm$^{-1}$ in point (II). The area delimited by the green rectangle represents the Raman shift interval between 1312 cm$^{-1}$ and 1345 cm$^{-1}$, considered to define the baseline to be subtracted from the data in order to avoid the luminescence background. The same interval was employed to evaluate the peak integral and for the reconstruction of the map reported in (**C**). (**C**) 16 × 16 Raman map (resolution < 2 µm) of the intensity distribution of the diamond Raman peak. The area covered by the map corresponds to the yellow square outlined in (**A**). (**D**) Merged image of (**A**,**C**).*

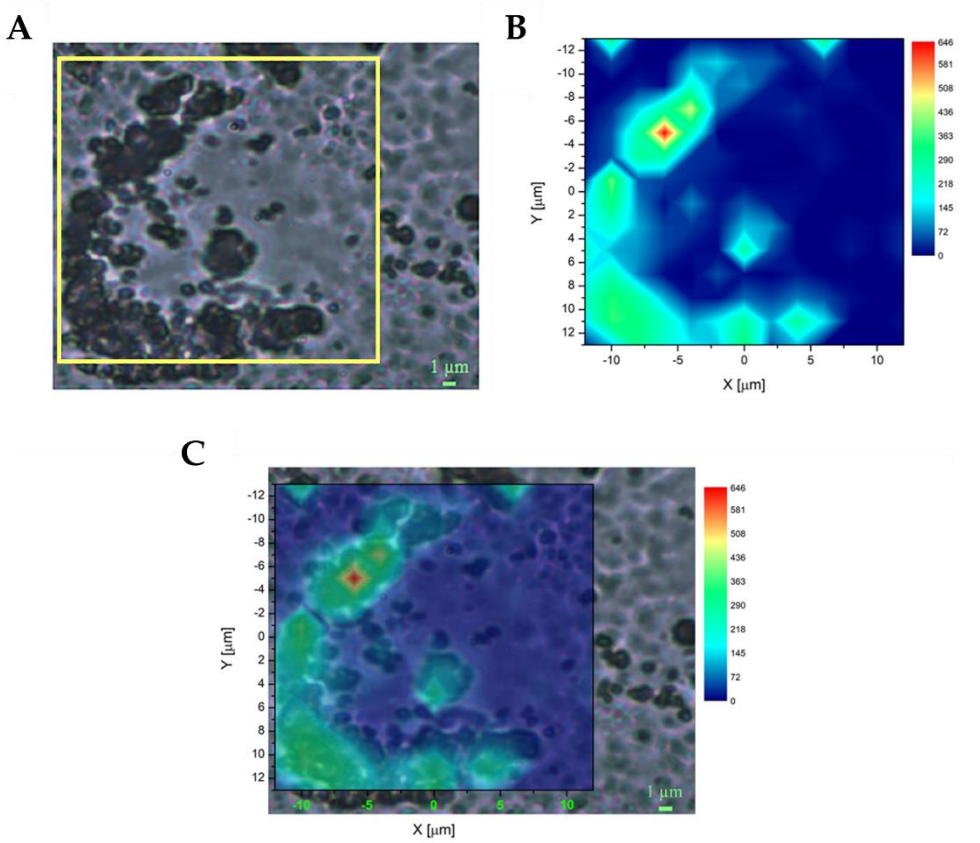


*Figure 53. H-ND localization in DAOY cell cultures using Raman mapping [201]. (**A**) Bright-field image of a cell incubated with 20 µg ml$^{-1}$ of 240 H2-NDs. The yellow square represents the area considered for mapping (scale bar 1 µm). (**B**) 13 × 14 Raman map (resolution < 2 µm) of the intensity distribution of the diamond Raman peak, evaluated as the area of the peak in the region of the Raman shift between 1309 cm$^{-1}$ and 1335 cm$^{-1}$. The area covered by the map corresponds to the yellow square outlined in (**A**). (**C**) Merged image of (**A**,**B**).*

The 2D Raman maps were obtained by measuring the Raman spectra of the samples on a grid of points with spacing around 2 µm, carrying out several acquisitions and then considering the average spectrum. In Figure 52A, two representative mapped points (I and II) are indicated with a cross and the corresponding Raman spectra are shown in Figure 52B. In point (I), an area without NDs is represented, while in point (II), the presence of NDs can be clearly detected by the Raman peak (highlighted with a green rectangle). After the point-by-point acquisition of the Raman spectra, their integral in the region containing the ND signature, i.e., between 1309 cm$^{-1}$ and 1345 cm$^{-1}$,

was considered. The ND peak area was obtained by subtracting the luminescence background of the spectra, defined through a baseline between the end-points of the considered Raman shift interval. The outcomes of these operations are shown in Figure 52C and Figure 53B, for the DAOY cells with OX- and H-NDs, respectively. Once the map is obtained, the localization of the NDs is identified from the merged images (bright-field image + Raman map) shown in Figure 52D and Figure 53C.

Comparing the maps for OX- and H-ND samples, stronger diamond signal intensities were detectable for the OX-type (Figure 52C and Figure 53B). Moreover, consistently with the fluorescence imaging information, H-NDs formed larger clusters due to their greater tendency to aggregate in water-based solutions with respect to OX-NDs. The ND cellular localization is non-uniform but concentrated in specific regions and Raman mapping confirmed the presence of a large quantity of NDs inside the DAOY cell cytoplasm, both for OX-NDs and H-NDs.

Therefore, the ND internalization has been confirmed by both fluorescence and Raman microscopy. Both H-NDs and OX-NDs localized mainly in the perinuclear area, with some difference in smaller H-NDs that tended to form aggregates and stick on cell membranes due to their hydrophobic nature.

After confirming the uptake of NDs in DAOY cells, the next step was to examine the NDs as radiosensitizers and the dependency of this effect on their characteristics such as surface modification, dimensions, and concentration.

### 3.4.2 Clonogenic survival after combined treatment of NDs and X-rays

To evaluate whether NDs could sensitize tumor cells to radiation-induced cell killing, a combined ND and X-ray (250 kVp) treatment was tested on the cell survival of a DAOY cell line (described in paragraph 2.5.1). To this aim, the cells were treated with various concentrations of NDs (10, 20, 40 µg/ml) of different sizes (18 nm, 55 nm, 240 nm) and surface terminations (OX- and

H-NDs; Figure 41) and then irradiated with different doses of X-rays (0 Gy, also named sham-irradiated, 2 Gy, 5 Gy and 8 Gy).

The first finding was that H-NDs alone reduce the viability of DAOY, revealing a basal cytotoxicity inversely proportional to their size, as opposed to OX-NDs, which show a trend toward increasing the survival fraction. In detail, H-NDs of all sizes significantly decrease cell survival at a concentration of 20 µg/ml (Figure 54), while a minor effect is seen at 10 µg/ml.

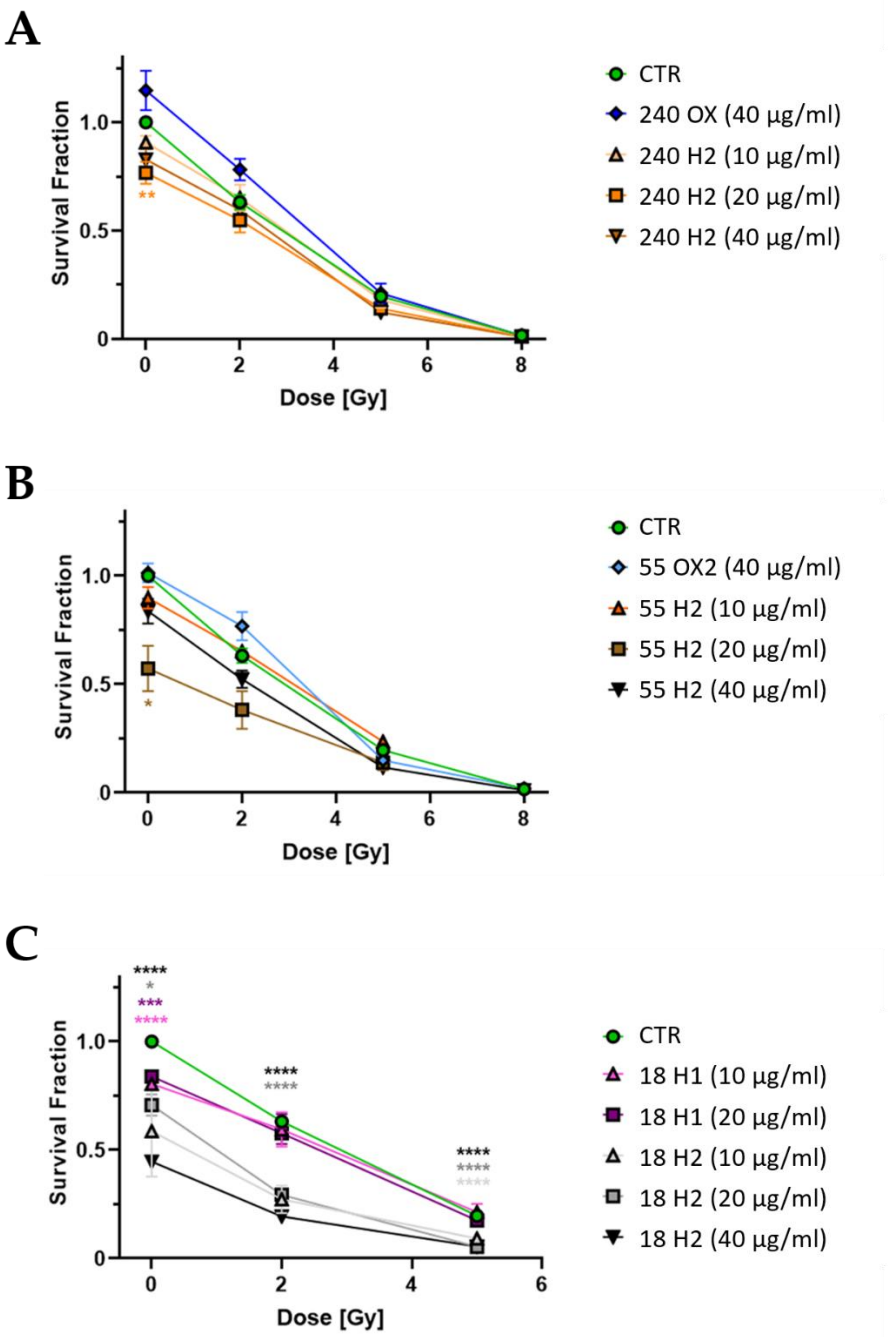


*Figure 54. Clonogenic survival assays of DAOY cells exposed to NDs and X-rays (refer to Figure 41 for ND sample specifications, adapted from [201]). (**A**) 240 nm NDs, (**B**) 55 nm NDs, and (**C**) 18 nm NDs. Mean survival relative to parental untreated cells and standard error of the mean are shown. All experiments were performed on at least 10 replicates. Two-Way ANOVA tests with the Greenhouse-Geisser correction and Tukey's multiple comparison tests were performed vs. the CTR for each dose. The* p-*values ≤ 0.05 (*) and ≤ 0.01 (**) were considered as statistically significant;* p-*values ≤ 0.001 (***) and ≤ 0.0001 (****) were considered as highly statistically significant.*

Moreover, the smallest 18 nm H-NDs are the most toxic, probably due to their greater tendency to aggregate, which decrease their biocompatibility, with a dependence on the different H-treatment. The higher efficacy of the H-treatment carried out on 18 H2-NDs (6 h, 850 °C), resulting in a complete elimination of oxygenated surface moieties, is responsible for their increased hydrophobic behaviour. Indeed, 18 H2-NDs produce a stronger decrease in cell survival compared to 18 H1-NDs (hydrogenation 3 h, 750 °C).

Cytotoxicity is also influenced by the concentration of NDs, and in line with reduced ND aggregation, less toxicity is observed at the lowest H-ND concentration (10 μg/ml). Nevertheless, these results do not reveal a straightforward correlation between ND concentration and cytotoxicity, which aligns with several studies that reported conflicting outcomes [130, 210].

Notably, the administration of combined treatment with H-NDs and 250 kVp X-ray irradiation do not produce a synergic effect (Figure 54A,B), and also OX-NDs do not show a radiosensitizing behaviour. Only 18 H2-NDs produce a significant decrease in the survival fraction at 2 Gy and 5 Gy (Figure 54C), probably due to the cumulative effect of the radiation treatment to the basal toxicity. The high cell killing induced at 8 Gy prevented the assessment of the efficacy of the combined treatment, and this dose was not replicated in the following experiments.

### 3.4.3 Clonogenic survival after combined treatment of NDs and γ-rays

To test the dependency of the radiosensitizing effects of NDs on radiation energy, the previous experiment was replicated, applying 1.25 MeV γ-rays from a $^{60}$Co source (Calliope Facility, ENEA, paragraph 2.5.3) and selecting a subset of H-NDs showing lower basal toxicity (240 nm, 55 nm and 18 nm H1 at 10 μg/ml). The clonogenic cell survival confirms the higher basal toxicity for 18 H1-NDs seen in the experiments with the X-rays (Figure 55A).

In this case, the combined treatment with 1.25 MeV γ-rays produces a significant decrease in the survival fraction at 5 Gy only for the 240 H2-NDs, compared to the ND-untreated 5 Gy irradiated control (Figure 55A,B), enhancing radiation-induced cell killing.

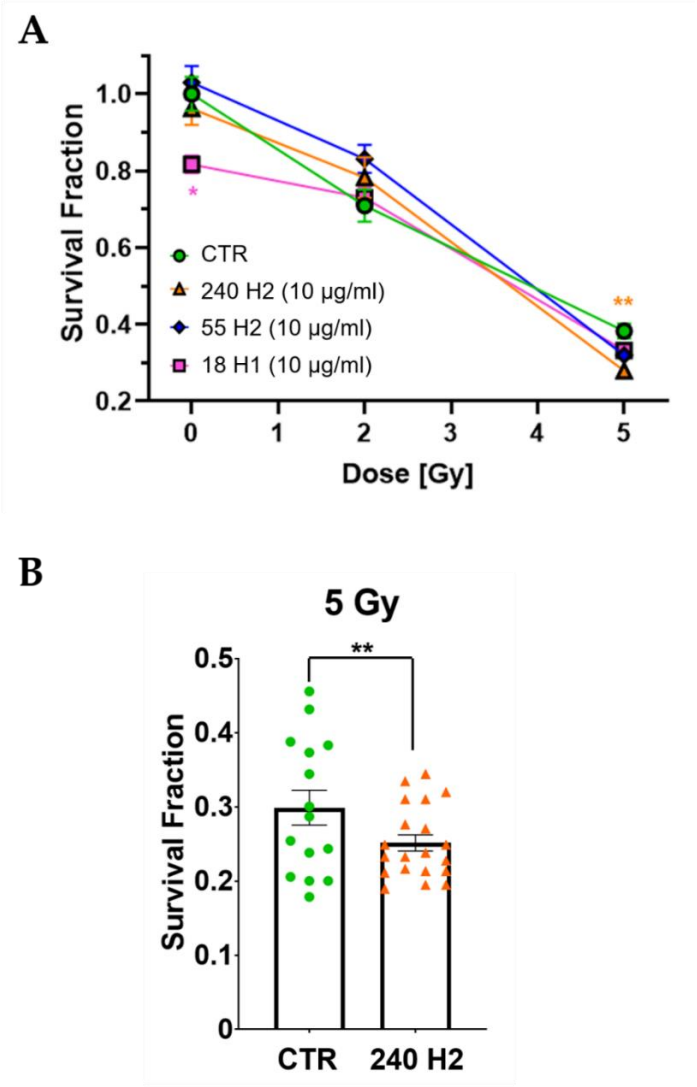


*Figure 55. Effect of combined H-ND and 1.25 MeV γ-ray treatment on DAOY cells (adapted from [201]). (**A**) Clonogenic assay mean survival relative to parental untreated cells and standard error of the mean are shown. All experiments were performed on at least 10 replicates. (**B**) Histogram plot highlighting the differences between cells irradiated with 5 Gy pre-treated with 240 H2-NDs (orange triangles) or untreated (CTR, green dots). Two-Way ANOVA tests with the Greenhouse-Geisser correction and Tukey's multiple comparison tests were performed vs. the CTR for each dose. The* p*-values ≤ 0.05 (*) and ≤ 0.01 (**) were considered as statistically significant.*

As for the experiments in PBS solutions (paragraph 3.3.3), the H-ND radiosensitizing effect could be explained by the negative electron affinity of H-NDs, promoting the transfer doping of electrons from the valence band to the redox species in the cytoplasm. The high reactivity of these emitted electrons with radical species can, in turn, increase the indirect radiation damage, for example towards the DNA molecule. Then, considering the key role that water molecules at the NP interface could play in the production of radicals, a difference in water disposition could also be responsible for the behaviour of H-NDs under irradiation [203].

### 3.4.4 DNA damage after combined treatment of NDs and γ-rays

In order to assess if the toxic effect of the combined treatment (H-NDs and γ-rays) was due to an increase in DNA damage, flow cytometry was used to evaluate the phosphorylation of histone H2AX (γ-H2AX), a double-strand breaks (DSBs) marker, 30 min and 24 h after irradiation with 2 Gy and 5 Gy. While irradiation with 2 Gy did not produce any increase in γ-H2AX over the unirradiated cell level at 30 min post-irradiation, a general significant γ-H2AX increase after irradiation with 5 Gy is reported (Figure 56A).

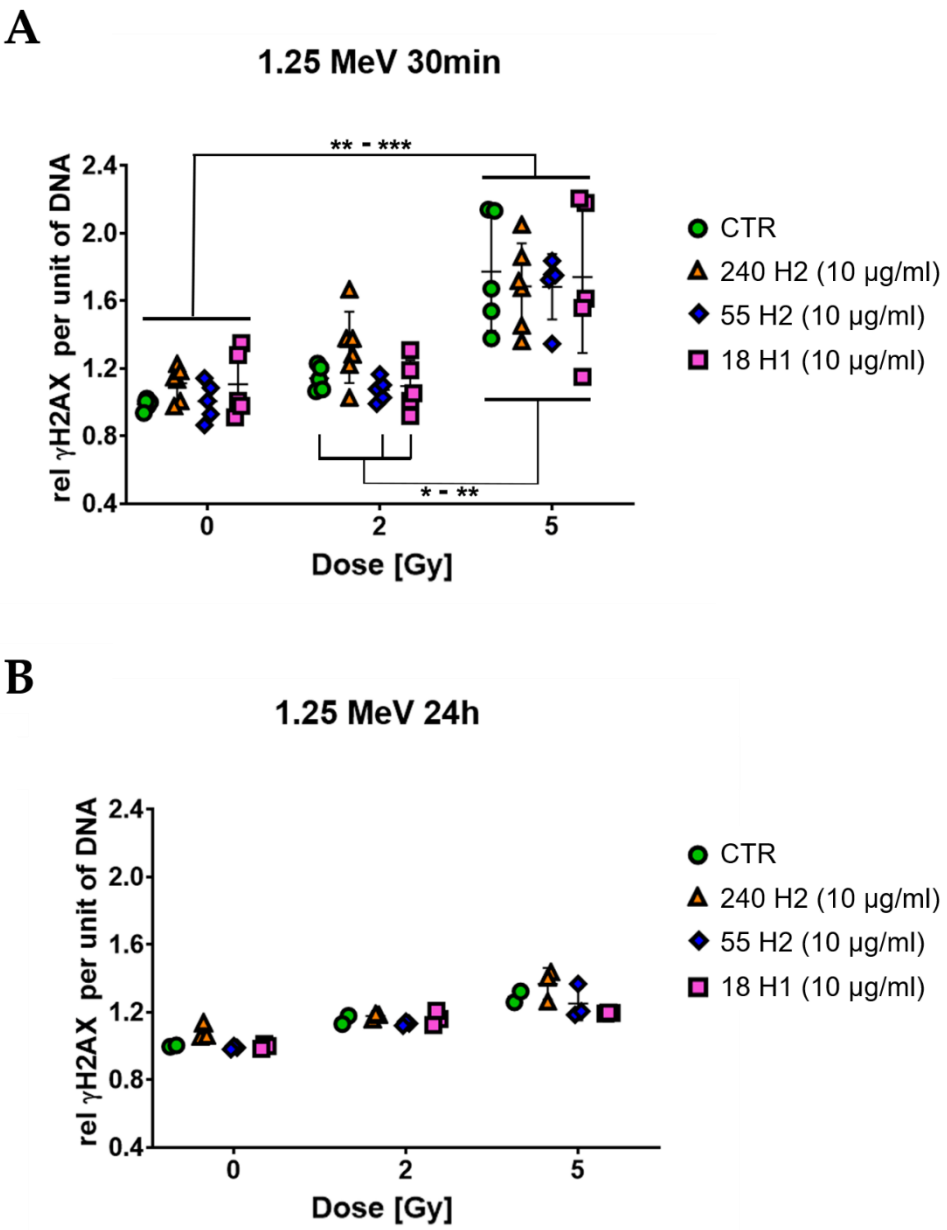


*Figure 56. Effect of combined H-ND and 1.25 MeV γ-ray treatment on DAOY cells (adapted from [201]). (**A**) γ-H2AX flow cytometry assay at 30 min after irradiation (*p-values: CTR-0 Gy vs. all 5 Gy samples ***; 240 H2-0 Gy vs. all 5 Gy samples **; 55 H2-0 Gy vs. all 5 Gy samples ***; 18 H1-0 Gy vs. all 5 Gy samples **; CTR-2 Gy vs. all 5 Gy samples *; 55 H2-2 Gy vs. all 5 Gy samples **; 18 H1-2 Gy vs. all 5 Gy samples **). (**B**) γ-H2AX flow cytometry assay at 24 h after irradiation. Data are represented as the mean florescence intensity per unit of DNA normalized on the sham-irradiated untreated controls (mean ± SEM). Two-way ANOVA tests with the Greenhouse-Geisser correction and Tukey's multiple comparison tests have been executed. The p-values ≤ 0.05 (*) and ≤ 0.01 (**) were considered as statistically significant; the p-values ≤ 0.001 (***) was considered as highly statistically significant.*

Significant differences were also observed between 2 Gy and 5 Gy irradiated cells for nearly all the treatments (Figure 56A), with the exception of the 240 H2-ND samples. No differences in γ-H2AX were observed within each dose group (unirradiated samples, and 2 Gy and 5 Gy irradiated samples), indicating that treatment with H-NDs does not affect the induction of DSBs. Furthermore, the expression of γ-H2AX at 24 h post-irradiation is restored to the basal level for all treatments, excluding the possibility of a higher complexity of DNA damage for H-NDs (Figure 56B).

### 3.4.5 Bax and Caspase-3 analysis following 240 nm H-ND/γ-ray combined treatment

The last step was the investigation into the nature of H-ND-radiation biological interactions and the molecular mechanisms underlying the H-ND-induced radiosensitization.

In paragraph 3.4.3, the combined treatment of DAOY cells with 240 H2-NDs and 5 Gy γ-ray irradiation (1.25 MeV) significantly increased cell killing. However, DNA damage is not involved in radiosensitization, since radiation-induced γ-H2AX phosphorylation is not significantly enhanced by treatment with H-NDs of any size. Additionally, the DNA damages are completely restored after 24 h, confirming the absence of slowly repairable clustered damages (Figure 56). Therefore, the protein content for pro-apoptotic markers Bax and cleaved-Caspase-3 was further assessed at 3 h post-irradiation (Figure 57).

Although all 240 H2-ND combined treatments show a trend toward a dose-dependent increase in cleaved-Caspase-3 expression, only the 5 Gy γ-ray one reaches significant variation in the expression of the targeted protein in comparison with both the untreated controls and 240 nm OX-ND-treated samples (Figure 57B). This is in accordance with the clonogenic survival results. Instead, Bax is unmodulated in all the treatment conditions at both the protein (Figure 57C) and transcript expression levels (Figure 57D). These

results indicate the absence of significant Bax modulation even at transcript expression level of a Caspase-3 activation in increasing cell killing for the 240 H2-ND/γ-ray combined treatment.

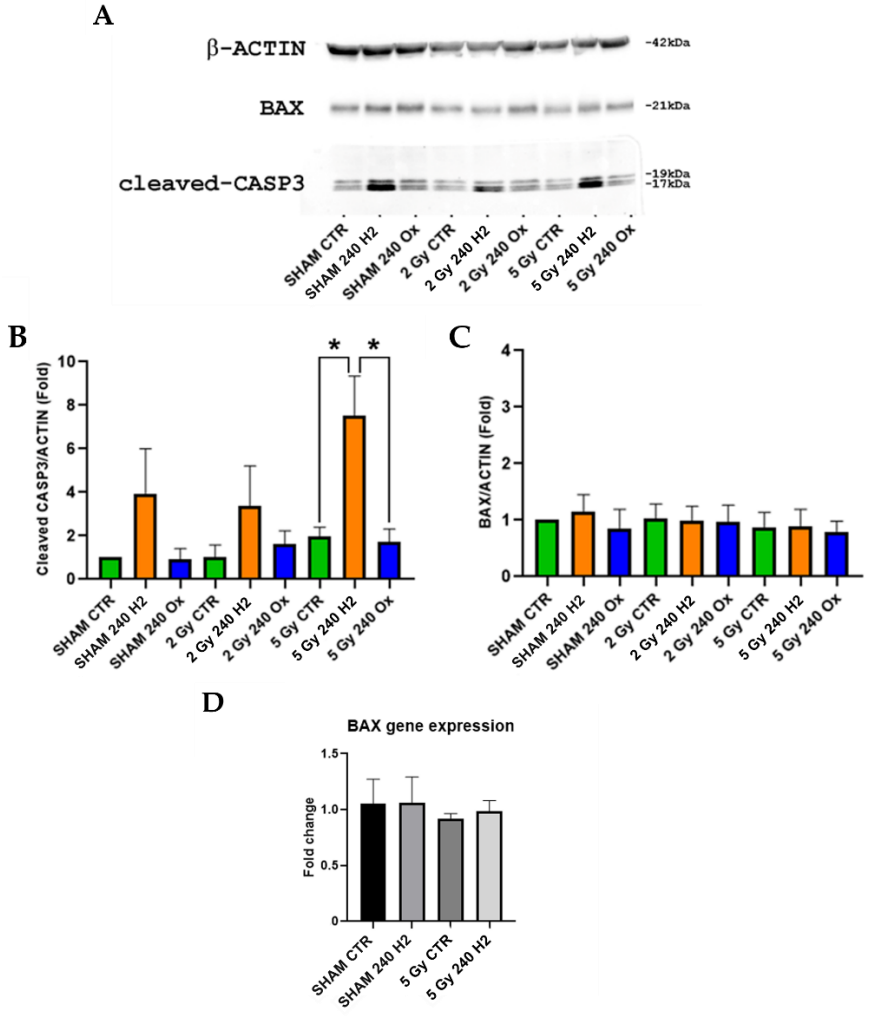


*Figure 57. Western blot analyses showing representative images of Caspase-3, Bax and β-actin protein expression in DAOY cells from the CTR, 240 H2-NDs, and 240 OX-NDs exposed to 0 Gy (sham), 2 Gy and 5 Gy (3 replicates) at 3 h post-irradiation with 1.25 Mev γ-rays. Band signals of target genes are normalized to those of β-actin (adapted from [201]). (**A**) The expression of the large cleavage form (17 kDa) of Caspase-3 increases significantly in DAOY cells treated with H-NDs and exposed to 5 Gy γ-rays. Bax is not modulated. (**B**,**C**) Quantification of Caspase-3 and Bax protein levels, showing fold changes vs. the sham controls. Student's* t *test was performed. The* p*-values < 0.05 (*) were considered as statistically significant. (**D**) Bax gene expression analysis: Bax mRNA level was measured by quantitative real-time PCR (qPCR). Results are shown as fold change (normalized for GAPDH). Values are represented as mean ± SEM.*

Many studies employing NPs as radiosensitizers suggest that nuclear DNA is the main target of NP-mediated radiosensitization and that this effect correlates the increase in cell killing with higher induction of DNA DSBs in irradiated cells pre-incubated with different types of NPs [211, 212]. Especially, the *in vitro* studies by Grall *et al.* reported increased DSBs and cell senescence in several radioresistant cancer cell lines treated with H-NDs and γ-radiation ($^{137}$Cs, 4 Gy) [87].

On the other hand, consistently with the results presented in this thesis, many reports have failed to demonstrate an increase in NP-mediated DSBs in irradiated cells, although a significant radiosensitizing effect had occurred [213]. The discrepancy also exists for NPs with very similar chemical/physical parameters [81, 213]. Actually, the molecular mechanism of the radiosensitizing effect of NPs is still unknown and represents a subject of intensive controversy due to the fact that the results on the involvement of nuclear DNA in this mechanism are contradictory.

In the presented experimental setup, the application of 240 nm H-NDs in conjunction with a 5 Gy dose of γ-rays at 1.25 MeV to the radioresistant DAOY cell line resulted in a substantial increase in Caspase-3 cleavage, which closely correlates with the reduction in cell viability seen following the same treatment. From a mechanistic perspective, the data provided solid evidence supporting the role of terminal apoptosis in the process of radiosensitization by NDs. Outstandingly, terminal apoptosis is unrelated to the induction of DNA damage, as indicated by the absence of any significant modulation of γ-H2AX and Bax. It is worth mentioning that while Bax is not a direct DNA damage marker its presence suggests an apoptotic response triggered by DNA damage.

Even though nuclear DNA is considered the main target for ionizing radiation [213, 214], this work findings show that NDs localized in the cytoplasm and did not penetrate the cell nucleus. Therefore, although the possibility that the NP-radiation interaction might produce secondary

electrons/radicals occasionally reaching the nucleus and damaging DNA may not be completely ruled out, it is unlikely that this damage can account for the increase in radiation-induced cell death by NPs. Indeed, the reactive radicals and secondary electrons produced by irradiated NPs are short-lived and can only act in a limited spatial range. Therefore, these damaging agents can only concentrate at high levels in tight shells around NP clusters. As suggested by an activation of the Bax-independent Caspase-3 signalling pathway, alternative targets for NP-mediated radiosensitization may exist, and these should be sought based on the localization of intracellular NP hotspots.

Apoptosis can be activated by both exogenous stimuli and signalling (extrinsic pathway) and endogenous unrepairable damage, clustered DNA damage, organelles and, above all, mitochondrial damage that is central in the intrinsic pathway (also called mitochondrial apoptosis). DAOY radioresistance, similarly to many radioresistant tumor cells, is associated with a p53-dependent impairment in the intrinsic pathway; thus, H-ND mediated apoptosis should be activated downstream of the p53-Bax axis [215, 216, 217]. Direct mitochondrial outer-membrane permeabilization is one of the main effectors in radiation-induced cell death in tumor cells [218], but other molecular targets in the intrinsic or extrinsic pathway are likely to be involved in the radiosensitizing action of H-NDs in RT (Figure 58).

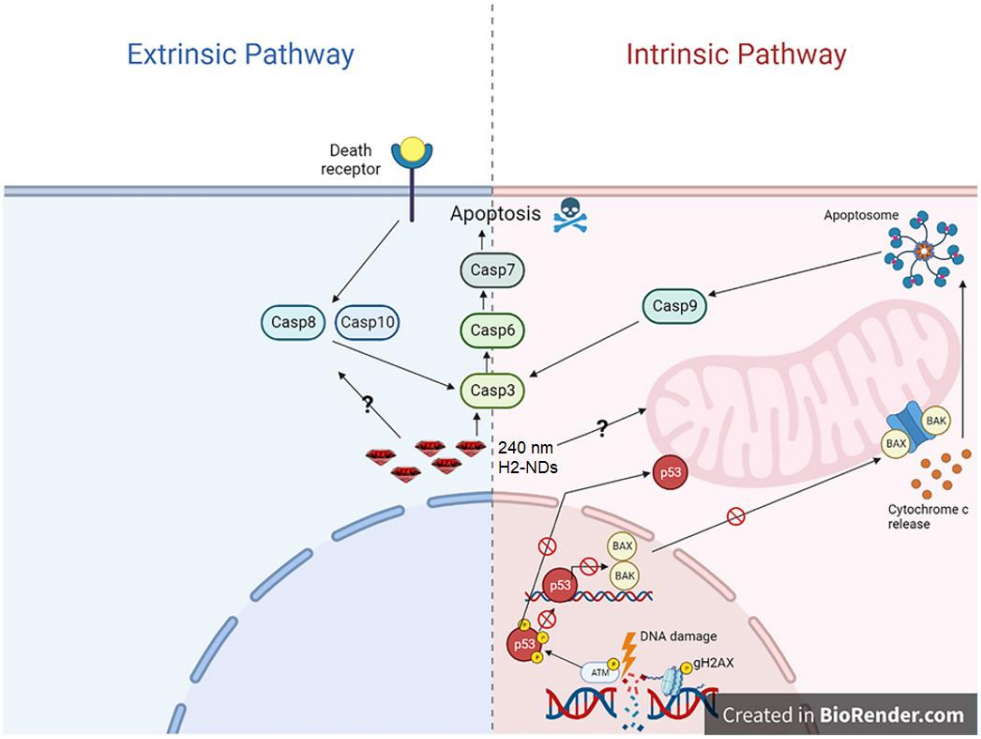


*Figure 58. Schematic representation of extrinsic and intrinsic apoptosis pathways created with BioRender.com (accessed on 24 July 2023). 240 nm H-NDs (red) are localized in the perinuclear area. Possible interactions with molecular targets are shown (adapted from [201]).*

# Conclusions

Radiotherapy (RT) represents a powerful technique that plays a critical role in the management of many tumor types. However, it is affected by substantial side effects ascribable to the perturbation of healthy cells surrounding the tumor volume. In medulloblastoma (MB) treatment, RT is typically performed after surgery, in combination with chemotherapy. Indeed, the combination of different therapeutic strategies may enhance the efficacy and reduce the toxicity observed in high-dose RT. The purpose of the research activity of this work was to characterize the radiosensitizing effect of thermally processed nanodiamonds (NDs), considered as a new class of physical agents among carbon nanoparticles (NPs), with a focus on their promising application in the biomedical context in assisting RT for the brain tumor treatment.

The modifications induced to NDs of different median diameter (18 nm, 55 nm and 240 nm) by thermal treatments were studied, focusing on hydrogenation and oxidation processes and ND chemical/physical properties were analysed. In particular, Diffuse Reflectance Infrared Fourier-Transform (DRIFT) spectroscopy, Raman spectroscopy and photoluminescence spectroscopy and Dynamic Light Scattering (DLS) analysis were employed.

DRIFT spectroscopy enabled the identification of ND surface moieties. The marked enhancement of C-H bands shows the success of hydrogenation processes. The strong reduction of water signature, together with the absence of signals referring to the C=O stretching in carboxylic groups, evidences the hydrophobic character of hydrogenated-NDs (H-NDs), contrary to oxidized-NDs (OX-NDs), characterized by a high water-affinity, as a consequence of their COOH-rich surface.

Raman spectroscopy confirmed that oxidation and hydrogenation treatments did not undermine the NP diamond core, while ND fluorescence detected through photoluminescence spectroscopy revealed that the spectrum intensity is directly correlated to ND size.

DLS analysis showed that H-NDs are affected by aggregation problems in aqueous solution, due to their hydrophobic behaviour. In addition, the aggregation trend appears inversely proportional to the average diameter of the particles, being more severe in the smaller NDs. The aggregation also depends on the intensity of the hydrogenation treatment. On the contrary, OX-NDs are well dispersed in water as a result of their hydrophilic nature.

After ND characterization, the creation of hydroxyl radicals (•OH) in aqueous solutions under X-ray irradiation (130 kVp) was explored for differently sized and treated NDs, to verify their radiosensitizing properties. The •OH radical is particularly relevant because it is a very dangerous compound to the organism and is considered the most damaging radical species [10], that cannot be eliminated by an enzymatic reaction. In particular, the evaluation of the •OH radical production from irradiated NDs aimed at assessing the possibility to use H-NDs as radiosensitizers. Based on their physical characteristics, H-NDs present several advantageous features for radioenhancement. They benefit from their semiconductor behaviour and negative electron affinity [10], that favour H-ND direct photo-induced emission of low-energy secondary electrons from their surface into the surrounding medium (electrons can escape once excited in the conduction band). These properties ensure high H-ND reactivity with oxygen species in an aqueous environment as the cellular one, acting as a potential source of reactive oxygen species (ROS) when activated via ionizing radiation.

The identification of •OH radicals, as specific ROS considered in this thesis, was carried out using a custom fluorometry setup, built up by the candidate, and exploiting the hydroxylation reaction of terephthalic acid (TPA) to yield the fluorescent 2-hydroxyterephthalic acid (HTPA). In the case

of 240 nm H-NDs, HTPA fluorescence and consequently •OH concentration was statistically significant vs. the only-TPA solutions. This finding opened the pathway for further studies devoted to verify the radiosensitizing effect of H-NDs following *in vitro* irradiation, also changing the irradiation conditions.

First, applying fluorescence and Raman microscopy and flow cytometry, the good internalization and cytoplasm localization of all the ND variants considered (18 nm, 55 nm and 240 nm H- and OX-NDs) in a human radioresistant medulloblastoma (MB) cell line (DAOY HTB-186) was verified.

Then, focusing on the effect of H-NDs, differences in cell survival dependent on the intensity of the employed beam energy were investigated. While at low energies (250 kVp) a synergic consequence of the combined treatment ND/irradiation was generally not seen, with 1.25 MeV γ-rays a significant decrease in cell survival at the 5 Gy dose co-treating with 240 nm H-NDs was found. Therefore, it has been demonstrated that also radiation energy is a key factor for the radiosensitizing effects of NDs.

Notably, beams ranging from 1 to 25 MV are by far the most commonly used for the treatment of deep-seated tumors (> 2 cm deep), such as brain tumors, making H-NDs an interesting opportunity for combined treatment. Furthermore, most studies in recent decades have widely focused on the radiosensitization induced by metal-NPs, in particular gold-NPs, combined with photon irradiation. In this case, the high atomic number (Z) of the metallic-NPs gives them a significantly higher X-ray mass energy-absorption coefficient compared to biological tissues [46]. These effects are maximized after exposure to radiation in the range of kilovoltage photon energy [47], where the predominant physical interaction between photons and NPs is the photoelectric effect. In our study, where 240 nm H-NDs were able to radiosensitize cells in combination with 5 Gy of γ-rays at 1.25 MeV, the Compton effect is predominant in driving the photon radiation-matter interaction. By this way, H-NDs could be proposed to increase the efficacy of

radiation, supporting the idea of using NPs not necessarily composed of high-Z atoms to improve high-energy RT treatments [87].

Nonetheless, a considerable influence of ND chemical/physical attributes, including their surface modification (H or OX), size and concentration, was highlighted on their toxicity (generally NDs have been shown to be non-toxic or only mildly toxic) and radiosensitising capacity. While this poses a challenge for research into ND effects, it also presents an opportunity, as manipulating ND surface properties holds the potential to purposefully modify their behaviour in biological contexts.

Moreover, this research work has established that in DAOY MB tumor cells the radiosensitising impact of H-NDs operates through a Caspase-3-dependent mechanism that is independent from DNA damage. However, there is a requirement for more comprehensive investigations to fully grasp these molecular mechanisms involving the activation of Bax-independent Caspase-3 and the nature of specific targets of the biological interactions involving NDs.

In conclusion, H-NDs revealed as potent radiosensitizers, but there is still prospective for optimizing their efficacy in combination with RT through further refinement of surface modification protocols, such as increasing hydrogenation. Additionally, a correlation between the H-ND radiosensitising effects and increased radiation energy has been documented. Supplementary research is necessary to unravel the complexity of ND effects and clarify the molecular mechanisms of ND biological interactions before their clinical application in RT. On the whole, the candidate investigations suggest that potential lies in discovering the ideal synergy between ND characteristics and radiation energy, which could represent a promising therapeutic approach for addressing radioresistant cancers through the utilization of high-energy radiation alongside H-NDs.

# Appendix A

## Nanodiamond quantum sensing revealing free radicals

Another possible application of nanodiamonds (NDs), as mentioned in the main text (paragraph 1.3.4), consists in their employment in magnetic resonance imaging (MRI). In particular, the paramagnetic nitrogen-vacancy (NV) defects make NDs outstanding contrast agents for MRI based on T1 relaxation time. Indeed, the peculiar electronic level structure of the $NV^-$ center of NDs can be perturbed by magnetic field and, through the relaxometry technique, nanoscale MRI measurements are performable with subcellular spatial resolution and extreme sensitivity, providing appealing perspectives for the investigation of biological samples. The defect changes its optical properties based on its magnetic surroundings, allowing, for example, the detection of locally generated free radicals. Therefore, this powerful method can provide a better understanding of the underlying mechanisms of an oxidative stress response.

In this context, during a research period at the University Medical Center of Groningen (The Netherlands) under the supervision of Prof. Romana Schirhagl, the candidate conducted some preliminary experiments employing T1 relaxometry technique by using NDs. These trials aimed to elucidate the antioxidant action of a natural enriched triterpene extract (OBE100) obtained from *Eucalyptus tereticornis* leaves, for the potential treatment of type 2 diabetes mellitus [219]. To get an insight into the OBE100 action mechanism, the free radical quantity was evaluated *in vitro* using NDs (5 μg/ml) and T1

magnetometry. Human liver hepatocellular carcinoma HepG2 cells were used.

The magnetometry setup was a custom confocal microscope with an acoustooptical modulator for detection [220]. Using pulse sequences, relaxometry was performed and the decay velocity was related to magnetic noise, which in this case stems from free radicals. More specifically, the NV centers were excited with a train of green laser pulses (532 nm). The relaxometry curves showed the relaxation from the bright spin state to a darker equilibrium after different dark times. The time needed to reach the equilibrium condition was linked to the presence of free radicals.

The preliminary results show an increase in the number of radicals (decreasing in the T1 value) following the administration of 0.5 mM of fatty acids (FA, sodium oleate/palmitic acid 2:1) to the samples, with respect to the T1 basal level (baseline), due to oxidative stress (Figure 59). From this situation, the subsequent administration of the OBE100 extract (100 μg/ml) causes a recovery of the T1 level, and in turn a reduction in the radical concentration, that returns to the basal level 12 h after administration. These preliminary findings are really promising in the assessing of the OBE100 natural extract as biologically effective and potentially useful in the treatment for type 2 diabetes mellitus.

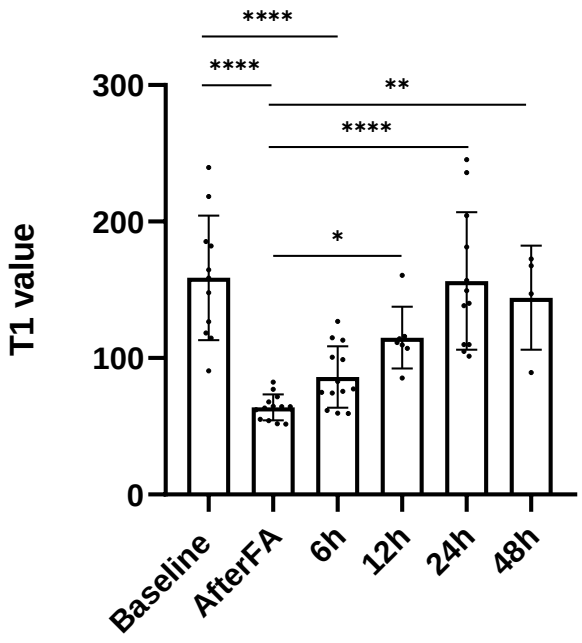


*Figure 59. T1 relaxation time values in HepG2 cell cultures with 5 μg/ml NDs (baseline), after the addition of 0.5 mM fatty acids (afterFA) and respectively 6 h, 12 h, 24 h and 48 h after the OBE100 extract administration (100 μg/ml). The measurements were executed on at least 7 replicates. Values are represented as mean ± SEM (standard error of the mean). One-Way ANOVA tests with the Tukey's multiple comparison tests were performed between the different samples and the baseline. The* p-*values ≤ 0.05 (*) and ≤ 0.01 (**) were considered as statistically significant;* p-*values ≤ 0.001 (***) and ≤ 0.0001 (****) were considered as highly statistically significant.*

# Appendix B

## Diamond biosensors for *in vitro* radiobiology

The investigation of secondary effects induced by ionizing radiation represents an ever-growing research field in radiobiology. This unsolved question requires novel technologies to achieve significant progress. In this framework, the candidate collaborated in the development and characterization of innovative artificial diamond-based biosensors (Figure 60), capable of simultaneous real-time detection schemes of the biological effects and irradiation dose on cells with a high temporal and spatial resolution. In particular, in the former case, the secretory activity from a cell network was investigated [221].

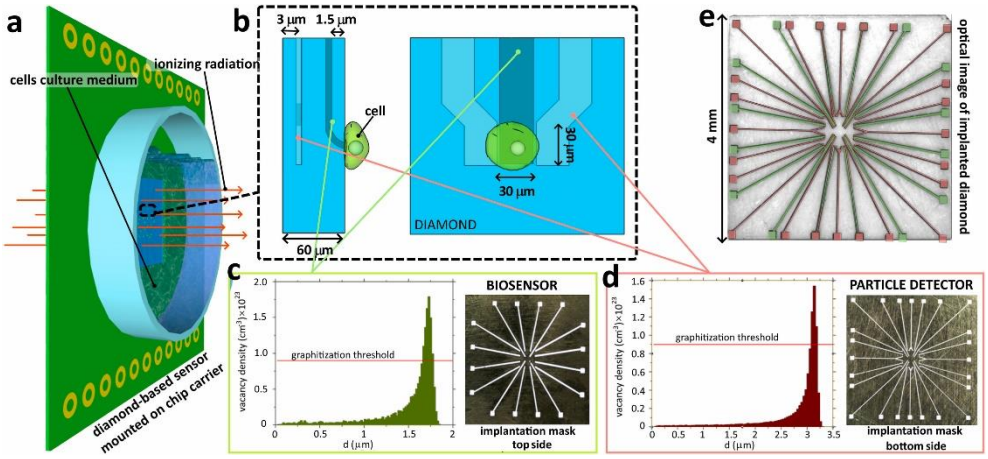


*Figure 60. (**a**) Schematic representation of the diamond sensor mounted on the chip carriers. (**b**) Schematic of the active region of one of the 16 channels. (**c**) Ion beam implantation conditions for the fabrication of the biosensing electrodes. (**d**) Ion beam implantation condition for the fabrication of the dosimetric electrodes. (**e**) Optical micrograph of the diamond substrate of the two implantation processes. The different types of graphitic electrodes are colour-highlighted to distinguish the biosensing (green) and the dosimetric (red) ones [221].*

The devices were functionally characterized by testing the amperometric measurements of neurotransmitter release from excitable cells (such as dopamine or adrenaline) and the dosimetric evaluation using different ionizing particles (alpha particle and X-ray photons). In addition, the sensors were employed to investigate the effects induced by X-rays on the exocytotic activity of PC12 neuroendocrine cells (a cell line derived from pheochromocytoma of the rat adrenal medulla), studying the neuronal secretion and expressly monitoring the modulation of the dopamine release, as shown in Figure 61.

The graphitic channels implanted into the diamond sensors through the Ion Beam Lithography technique act as electrodes for the detection of the molecules secreted from single cells as well as for the collection of the signals induced by ionizing radiation. The applicability of these devices for *in vitro* experiments was proved and the modulation of dopamine release from PC12 cells triggered by X-rays was observed. Further investigations combining these sensors with pharmacological treatments (inhibition or stimulation of spontaneous exocytosis) can clarify the biological pathways activated by

ionizing radiation that could have an impact on the understanding of undesired and still unknown secondary effects observed during brain radiotherapy treatments.

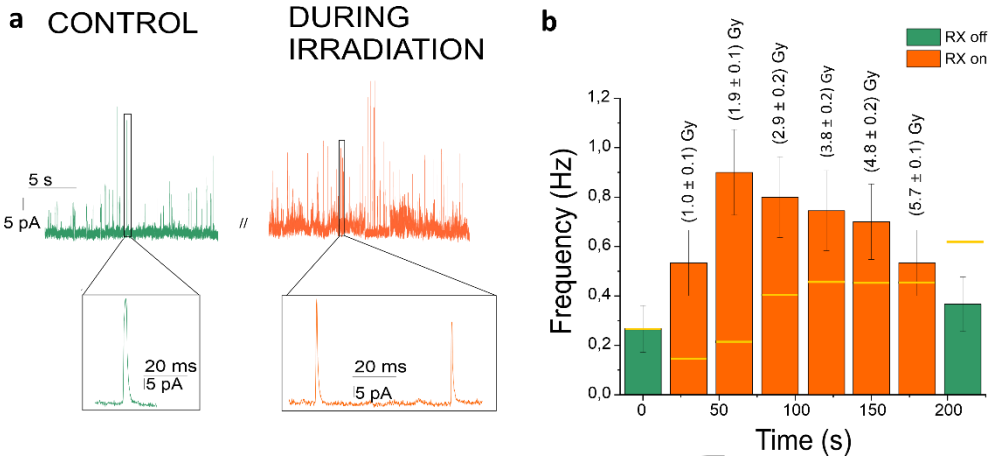


*Figure 61. (**a**) Representative electrode chronoamperogram of the spontaneous exocytotic activity of a PC12 cell before (control) and during X-ray irradiation. The insets report the magnification of a small portion of the amperometric recording showing the characteristic shape of the exocytotic peaks. (**b**) Frequency distribution of the exocytotic events: red bars are associated with the signal recorded during the exposure of the cell to the X-rays with reported the cumulated dose [221].*

# Appendix C

## Combining diamond biosensors with Amperometric Peak Analysis (APE) code

As briefly described in Appendix B, artificial diamond-based multi-electrode array with micrographitc channels can be successfully employed to reveal, in real-time, quantal exocytotic events occurring from many individual neurosecretory cells or from many neurons within a network. These electrochemical sensors present a high signal-to-noise ratio [222], and a good temporal resolution (< ms) that allow the detection of fast exocytotic events. Due to the 16 sensing microelectrodes that characterize these devices, each recording large amounts of data relating to the exocytotic activity, an adequate, fast and effective analysis software to speed up the signal detection will present a significant improvement in the study of quantal secretory events. Therefore, it is mandatory to improve the automated routine for signal sorting and parameter evaluation, as performed by the Amperometric Peak Analysis (APE) code [223].

During the research activity, the candidate had the opportunity to collaborate to the implementation of the APE automated analysis code, developed with Matlab R2022a software, that provides easy and accurate detection of amperometric spike parameters. The analysed data were acquired from cultured PC12 cells (see Appendix B), collecting the events during spontaneous exocytotic activity or after L-DOPA incubation.

The data demonstrate that the developed biosensors provide an excellent multi-electrode tool that, combined with the APE code, guarantees a standardized and rapid analysis of the exocytosis.

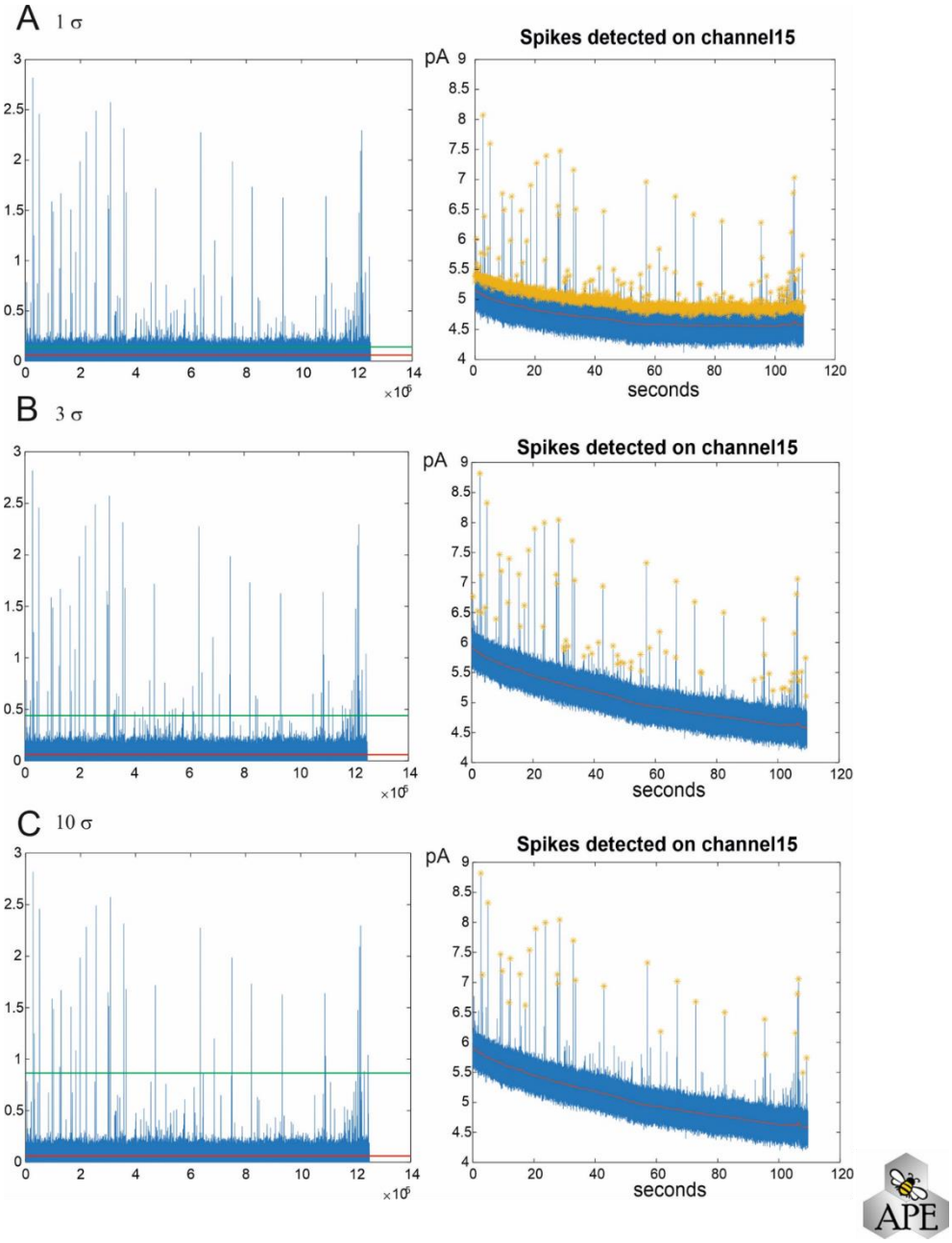


*Figure 62. Signal identification in three different configurations (adapted from [223]): 1 σ (**A**), 3 σ (**B**), and 10 σ (**C**). (**Left**): signals filtered. The red line indicates the subtraction of the filtered background. The green line represents the threshold above which the amperometric spikes are identified. (**Right**): chronoamperograms of the spikes detected by a representative channel. The yellow stars indicate the detected spikes, while the red line is the background.*

# Bibliography


[1] R. Peris-Bonet, C. Martínez-García, B. Lacour, S. Petrovich, B. Giner-Ripoll, A. Navajas and E. Steliarova-Foucher, "Childhood central nervous system tumours–incidence and survival in Europe (1978–1997): report from Automated Childhood Cancer Information System project," *Eur J Cancer*, vol. 42, no. 13, pp. 2064-2080, 2006.

[2] M. Karajannis, J. Allen and E. Newcomb, "Treatment of pediatric brain tumors," *J Cell Physiol*, vol. 217, pp. 584-589, 2008.

[3] R. Baskar, K. Lee, R. Yeo and K. Yeoh, "Cancer and radiation therapy: Current advances and future directions," *Int J Med Sci*, vol. 9, p. 193–199, 2012.

[4] X.-D. Zhang, H. Wang, A. Antaris, L. Li, S. Diao, R. Ma, A. Nguyen, G. Hong, Z. Ma, J. Wang, S. Zhu, J. Castellano, T. Wyss-Coray, Y. Liang, J. Luo and H. Dai, "Traumatic brain injury imaging in the second near-infrared window with a molecular fluorophore," *Adv Mater*, vol. 28, no. 32, p. 6872–6879, 2016.

[5] X. Song, Z. Sun, L. Li and L. Zhou, "Application of nanomedicine in radiotherapy sensitization," *Frontiers in Oncology*, vol. 13, p. 1088878, 2023.

[6] P. Agarwalla, T. Royce, M. Koch, J. Daartz and J. Loeffler, "Application of Current Radiation Delivery Systems and Radiobiology," in *Principles of Neurological Surgery*, Elsevier Inc, 2018, pp. 714-726.e2.

[7] U. Amaldi and G. Kraft, "Radiotherapy with beams of carbon ions," *Reports Prog Phys*, vol. 68, pp. 1861-1882, 2005.

[8] A. Giulietti, "Laser-driven particle acceleration for radiobiology and radiotherapy: where we are and where we are going," in *Proceedings of the SPIE 10239*, 2017.

[9] R. Imai, T. Kamada and N. Araki, "Carbon ion radiation therapy for unresectable sacral chordoma: an analysis of 188 cases," *Int J Radiat Oncol Biol Phys*, vol. 95, no. 1, p. 322–327, 2016.

[10] L. Shirley, Biomolecular Action of Ionizing Radiation, Taylor & Francis, 2007.

[11] https://www.arpansa.gov.au/understanding-radiation/what-is-radiation/ionising-radiation/gamma-radiation (accessed in December 2023).

[12] Radiation. IARC Monographs on the Evaluation of Carcinogenic Risk to Humans Volume 100D, International Agency for Research on Cancer (IARC), 2012.

[13] https://collaborations.fz-juelich.de/ikp/cgswhp/cgswhp18/program/talks/23.08/ParSession8/Beka_Bochorishvili_GGSWBS18_23_08_2018.pdf (accessed in December 2023).

[14] E. Podgorsak, Radiation physics for medical physicists, Springer Science & Business Media, 2010.

[15] J. Turner, "Interaction of Ionizing Radiation with Matter," *Health Phys,* vol. 86, p. 228–252, 2004.

[16] A. Bielajew, Fundamentals of Radiation Dosimetry and Radiological Physics, 2005.

[17] https://epos.myesr.org/posterimage/esr/ecr2018/143546/mediagallery/764967 (accessed in January 2024).

[18] H. Hirayama, Lecture note on photon interactions and cross sections, 2000.

[19] Z. Kuncic and S. Lacombe, "Nanoparticle radio-enhancement: principles, progress and application to cancer treatment," *Phys Med Biol,* vol. 63, no. 2, p. 02TR01, 2018.

[20] "The 2007 Recommendations of the International Commission on Radiological Protection," ICRP Publication 103. Ann. ICRP 37 (2-4), 2007.

[21] G. Hine and G. Brownell, Radiation dosimetry, Elsevier, 2013.

[22] E. Hall and A. Giaccia, Radiobiology for the Radiologist, Lippincott Williams & Wilkins, 2006.

[23] H. Wang, X. Mu, H. He and X. Zhang, "Cancer Radiosensitizers," *Trends Pharmacol Sci,* vol. 39, p. 24–48, 2018.

[24] M. Nechifor, T.-M. Neagu and G. Manda, "Reactive oxygen species, cancer and anti-cancer therapies," *Current Chemical Biology,* vol. 3, no. 1, p. 22–46, 2009.

[25] L. He, H. Lai and T. Chen, "Dual-function nanosystem for synergetic cancer chemo-/radiotherapy through ROS-mediated signalling pathways," *Biomaterials,* vol. 51, p. 30–42, 2015.

[26] S. Her, D. Jaffray and C. Allen, "Gold nanoparticles for applications in cancer radiotherapy: mechanisms and recent advancements," *Adv Drug Deliv Rev,* vol. 109, p. 84–101, 2017.

[27] T. Henriksen and D. Maillie, Radiation and health, CRC Press, 2003.

[28] R. Packer, L. Sutton, R. Elterman, B. Lange, J. Goldwein, S. Nicholson, L. Mulne, J. Boyett, G. D'Angio, K. Wechsler-Jentzsch, G. Reaman, B. Cohen, D. Bruce, L. Rorke, P. Molloy, J. Ryan, D. LaFond, A. Evans and l. Schut, "Outcome for children with medulloblastoma treated with radiation and cisplatin, CCNU, and vincristine chemotherapy," *J Neurosurg,* vol. 81, no. 5, pp. 690-698, 1994.

[29] L. Mendez, Y. Weiss, D. D'Souza, A. Ravi, L. Barbera and E. Leung, "Three-dimensional-guided perineal-based interstitial brachytherapy in cervical cancer: A systematic review of technique, local control and toxicities," *Radiother Oncol,* vol. 123, no. 2, p. 312–318, 2017.

[30] H. Buckley, C. Wilson and T. Ajithkumar, "High-Dose-Rate brachytherapy in the Management of Operable Rectal Cancer: A Systematic Review," *Int J Radiat Oncol Biol Phys,* vol. 99, no. 1, p. 111–127, 2017.

[31] F. Kong, H. Ying, R. Zhai, C. Du, S. Huang, J. Zhou, X. He, C. Hu, Z. Wang, T. Sun and Q. Ji, "Clinical outcome of intensity modulated radiotherapy for carcinoma showing thymus-like differentiation," *Oncotarget,* vol. 7, p. 81899–81905, 2016.

[32] M. Reis Ferreira, A. Khan, K. Thomas, L. Truelove, H. McNair, A. Gao, C. Parker, R. Huddart, M. Bidmead, R. Eeles, V. Khoo, N. van As, V. Hansen and D. Dearnaley, "Phase 1/2 dose-escalation study of the use of intensity modulated radiation therapy to treat the prostate and pelvic nodes in patients with prostate cancer," *Int J Radiat Oncol Biol Phys,* vol. 99, no. 5, p. 1234–1242, 2017.

[33] T. Bird, F. De Felice, A. Michaelidou, S. Thavaraj, J.-P. Jeannon, A. Lyons, R. Oakley, R. Simo, M. Lei and T. Guerrero Urbano, "Outcomes of intensity-modulated radiotherapy as primary treatment for oropharyngeal squamous cell carcinoma – a European single institution analysis," *Clin Otolaryngol,* vol. 42, no. 1, p. 115–122, 2017.

[34] S. Acharya, B. Fischer-Valuck, R. Kashani, P. Parikh, D. Yang, T. Zhao, O. Green, O. Wooten, H. Li, Y. Hu, V. Rodriguez, L. Olsen, C. Robinson, J. Michalski, S. Mutic and J. Olsen, "Online Magnetic Resonance Image Guided Adaptive Radiation Therapy: First Clinical Applications," *Int J Radiat Oncol Biol Phys,* vol. 94, no. 2, p. 394–403, 2016.

[35] H. Raziee, F. Moraes, J. Murgic, M. Chua, M. Pintilie, P. Chung, C. Ménard, A. Bayley, M. Gospodarowicz, P. Warde, T. Craig, C. Catton, R. Bristow, D. Jaffray and A. Berlin, "Improved outcomes with dose escalation in localized prostate cancer treated with precision image-guided radiotherapy," *Radiother Oncol,* vol. 123, no. 3, p. 459–465, 2017.

[36] R. Jimenez, B. Alexander, A. Mahadevan, A. Niemierko, S. Rajakesari, N. Arvold, S. Floyd, K. Oh, J. Loeffler and H. Shih, "The impact of different stereotactic radiation therapy regimens for brain metastases on local control and toxicity," *Adv Radiat Oncol,* vol. 2, no. 3, p. 391–397, 2017.

[37] H. Chen, A. Louie, R. Boldt, G. Rodrigues, D. Palma and S. Senan, "Quality of Life After Stereotactic Ablative Radiotherapy for Early-Stage Lung Cancer: A Systematic Review," *Clin Lung Cancer,* vol. 17, no. 5, p. 141–149, 2016.

[38] F. Tonissi, L. Lattanzio, V. Astesana, F. Cavicchioli, A. Ghiglia, M. Monteverde, D. Vivenza, L. Gianello, E. Russi, M. Merlano and C. Lo Nigro, "Reoxygenation Reverses Hypoxia-related Radioresistance in Head and Neck Cancer Cell Lines," *Anticancer Res,* vol. 36, no. 5, p. 2211–2215, 2016.

[39] S. Okamoto, T. Shiga, K. Yasuda, S. Watanabe, K. Hirata, K. Nishijima, M. K., K. Kasai, R. Onimaru, K. Tuchiya, Y. Kuge, H. Shirato and N. Tamaki, "The reoxygenation of hypoxia and the reduction of glucose metabolism in head and neck cancer by fractionated radiotherapy with intensity-modulated radiation therapy," *Eur J Nucl Med Mol Imaging,* vol. 43, no. 12, p. 2147–2154, 2016.

[40] J. Brown, D. Carlson and D. Brenner, "The tumor radiobiology of SRS and SBRT: are more than the 5 Rs involved?," *Int J Radiat Oncol Biol Phys,* vol. 88, no. 2, p. 254–262, 2014.

[41] C. Carrie, X. Muracciole, F. Gomez, J. Habrand, M. Benhassel, M. Mege, M. Mahé, P. Quetin, J. Maire, F. Soum, M. Baron, P. Clavere, S. Chapet, Z. Gaci, H. Kolodie, P. Maingon, B. Vie, V. Bernier, C. Alapetite, S. Hoffstetter, J. Grill and F. Lafay, "Conformal radiotherapy, reduced boost volume, hyperfractionated radiotherapy, and online quality control in standard-risk medulloblastoma without chemotherapy: results of the French M-SFOP 98 protocol," *J Radiat Oncol Biol Phys,* vol. 63, no. 3, pp. 711-716, 2005.

[42] B. Eaton, G. Fong, L. Ingerski, M. Pulsifer, S. Goyal, C. Zhang, E. Weyman, N. Esiashvili, J. Klosky, T. MacDonald, D. Ebb, S. MacDonald, N. Tarbell and T. Yock, "Intellectual functioning among case-matched cohorts of children treated with proton or photon radiation for standard-risk medulloblastoma," *Cancer,* vol. 127, no. 20, pp. 3840-3846, 2021.

[43] A. Paulino, E. Ludmir, D. Grosshans, J. Su, S. McGovern, M. Okcu, M. McAleer, P. Baxter, A. Mahajan and M. Chintagumpala, "Overall survival and secondary malignant neoplasms in children receiving passively scattered proton or photon craniospinal irradiation for medulloblastoma," *Cancer,* vol. 127, no. 20, pp. 3865-3871, 2021.

[44] V. Pokropivny, R. Lohmus, I. Hussainova, A. Pokropivny and S. Vlassov, Introduction to nanomaterials and nanotechnology, University of Tartu, 2007.

[45] Z. Abdullaeva, "Classification of Nanomaterials," in *Nano- and Biomaterials: Compounds, Properties, Characterization, and Applications*, Wiley-VCH Verlag GmbH & Co. KGaA, 2017, p. 27–56.

[46] M. Kebede and T. Imae, "Low-Dimensional Nanomaterials," in *Advanced Supramolecular Nanoarchitectonics*, William Andrew Publishing, 2019, p. 3–16.

[47] Paras, K. Yadav, P. Kumar, D. Teja, S. Chakraborty, M. Chakraborty, S. Mohapatra, A. Sahoo, M. Chou, C.-T. Liang and D.-R. Hang, "A Review on Low-Dimensional Nanomaterials: Nanofabrication, Characterization and Applications," *Nanomaterials,* vol. 13, no. 1, p. 160, 2023.

[48] R. Freitas, Nanomedicine, Volume I: Basic Capabilities, vol. 1, Austin, TX, U.S.A.: Landes Bioscience, 1999.

[49] U. Prabhakar, H. Maeda, R. Jain, E. Sevick-Muraca, W. Zamboni, O. Farokhzad, S. Barry, A. Gabizon, P. Grodzinski and D. Blakey, "Challenges and key considerations of the enhanced permeability and retention effect for nanomedicine drug delivery in oncology," *Cancer Res,* vol. 73, no. 8, pp. 2412-2417, 2013.

[50] A. MaHam, Z. Tang, H. Wu, J. Wang and Y. Lin, "Protein-based nanomedicine platforms for drug delivery," *Small,* vol. 5, no. 15, pp. 1706-1721, 2009.

[51] J. Leary and J. Key, "Nanoparticles for multimodal in vivo imaging in nanomedicine," *Int J Nanomed,* vol. 9, p. 711, 2014.

[52] Z. Peng, X. Han, S. Li, A. Al-Youbi, A. Bashammakh, M. El-Shahawi and R. Leblanc, "Carbon dots: biomacromolecule interaction, bioimaging and nanomedicine," *Coord Chem Rev,* vol. 343, pp. 256-277, 2017.

[53] Z. Haidar, "Bio-inspired/-functional colloidal core-shell polymeric-based nanosystems: technology promise in tissue engineering," *Bioimag NanoMed Polym,* vol. 2, pp. 323-352, 2010.

[54] G. Yang, C. Zhu, D. Du, J. Zhu and Y. Lin, "Graphene-like two-dimensional layered nanomaterials: applications in biosensors and nanomedicine," *Nanoscale,* vol. 7, p. 14217–14231, 2015.

[55] J. Chan and C. Xu, Perspectives in Micro- and Nanotechnology for Biomedical Applications, Covent Garden, London: Imperial College Press, 2016.

[56] Y. Mi, Z. Shao, J. Vang, O. Kaidar-Person and A. Wang, “Application of nanotechnology to cancer radiotherapy,” *Cancer Nano,* vol. 7, p. 11, 2016.

[57] X. Song, Z. Sun, L. Li, L. Zhou and S. Yuan, “Application of nanomedicine in radiotherapy sensitization,” *Front Oncol,* vol. 13, p. 1088878, 2023.

[58] S. Lee and B.-H. Jun, “Silver nanoparticles: synthesis and application for nanomedicine,” *Int J Mol Sci,* vol. 20, p. 865, 2019.

[59] E. Boisselier and D. Astruc, “Gold nanoparticles in nanomedicine: preparations, imaging, diagnostics, therapies and toxicity,” *Chem Soc Rev,* vol. 38, p. 1759, 2009.

[60] Z. Ren, S. Sun, R. Sun, G. Cui, L. Hong, B. Rao, A. Li, Z. Yu, Q. Kan and Z. Mao, “A metal–polyphenol-coordinated nanomedicine for synergistic cascade cancer chemotherapy and chemodynamic therapy,” *Adv Mater,* vol. 32, p. 1906024, 2020.

[61] Y. Wang and L. Chen, “Quantum dots, lighting up the research and development of nanomedicine,” *Nanomed-Nanotechnol,* vol. 7, no. 4, p. 385–402, 2011.

[62] R. Zhang, F. Yan and Y. Chen, “Exogenous physical irradiation on titania semiconductors: materials chemistry and tumor-specific nanomedicine,” *Adv Sci,* vol. 5, p. 1801175, 2018.

[63] A. Rafieerad, W. Yan, A. Amiri and S. Dhingra, “Bioactive and trackable MXene quantum dots for subcellular nanomedicine applications,” *Mater Des,* vol. 196, p. 109091, 2020.

[64] E. Cabane, X. Zhang, K. Langowska, C. Palivan and W. Meier, “Stimuli-responsive polymers and their applications in nanomedicine,” *Biointerphases,* vol. 7, p. 9, 2012.

[65] J. Khandare, M. Calderón, N. Dagia and R. Haag, “Multifunctional dendritic polymers in nanomedicine: opportunities and challenges,” *Chem Soc Rev,* vol. 41, p. 2824–2848, 2012.

[66] A. Wagner, D. Spencer and N. Peppas, “Advanced architectures in the design of responsive polymers for cancer nanomedicine,” *J Appl Polym Sci,* vol. 135, p. 46154, 2018.

[67] S. Suresh, “Elastic clues in cancer detection,” *Nat Nanotechnol,* vol. 2, no. 12, p. 748–749, 2007.

[68] B. Godin, J. Sakamoto, R. Serda, A. Grattoni, A. Bouamrani and M. Ferrari, “Emerging applications of nanomedicine for the diagnosis and treatment of

cardiovascular diseases," *Trends Pharmacol Sci,* vol. 31, no. 5, p. 199–205, 2010.

[69] A. Kabanov and H. Gendelman, "Nanomedicine in the diagnosis and therapy of neurodegenerative disorders," *Prog Polym Sci,* vol. 32, no. 8-9, p. 1054–1082, 2007.

[70] M. Muthu, L. Mei and S.-S. Feng, "Nanotheranostics: advanced nanomedicine for the integration of diagnosis and therapy," *Nanomedicine,* vol. 9, p. 1277–1280, 2014.

[71] Y. Shi, R. van der Meel, X. Chen and T. Lammers, "The EPR effect and beyond: Strategies to improve tumor targeting and cancer nanomedicine treatment efficacy," *Theranostics,* vol. 10, p. 7921–7924, 2020.

[72] A. Vodyashkin, M. Rizk, P. Kezimana, A. Kirichuk and Y. Stanishevskiy, "Application of Gold Nanoparticle-Based Materials in Cancer Therapy and Diagnostics," *ChemEngineering,* vol. 5, p. 69, 2021.

[73] https://www.wichlab.com/nanometer-scale-comparison-nanoparticle-size-comparison-nanotechnology-chart-ruler-2/ (accessed in January 2024).

[74] P. Retif, S. Pinel, M. Toussaint, C. Frochot, R. Chouikrat, T. Bastogne and M. Barberi-Heyob, "Nanoparticles for Radiation Therapy Enhancement: the Key Parameters," *Theranostics,* vol. 5, no. 9, pp. 1030-1044, 2015.

[75] M. Falk, "Nanodiamonds and nanoparticles as tumor cell radiosensitizers-promising results but an obscure mechanism of action," *Ann Transl Med,* vol. 5, no. 1, p. 18, 2017.

[76] R. Evans, The Atomic Nucleus, New York: McGraw-Hill, 1995.

[77] I. Tremi, S. Havaki, S. Georgitsopoulou, G. Terzoudi, I. Lykakis, G. Iliakis, V. Georgakilas, V. Gorgoulis and A. Georgakilas, "Biological Response of Human Cancer Cells to Ionizing Radiation in Combination with Gold Nanoparticles," *Cancers,* vol. 14, p. 5086, 2022.

[78] A. Sani, C. Cao and D. Cui, "Toxicity of gold nanoparticles (AuNPs): A review," *Biochemistry and Biophysics Reports,* vol. 26, p. 100991, 2021.

[79] C. Goodman, C. McCusker, T. Yilmaz and V. Rotello, "Toxicity of gold nanoparticles functionalized with cationic and anionic side chains," *Bioconjug Chem,* vol. 15, p. 897–900, 2004.

[80] M. Stefan, V. Melnig, D. Pricop, A. Neagu, M. Mihasan, L. Tartau and L. Hritcu, "Attenuated effects of chitosan-capped gold nanoparticles on LPS-induced toxicity in laboratory rats," *Mater Sci Eng C,* vol. 33, p. 550–556, 2013.

[81] E. Porcel, S. Liehn, H. Remita, N. Usami, K. Kobayashi, Y. Furusawa, C. Le Sech and S. Lacombe, "Platinum nanoparticles: a promising material for future cancer therapy?," *Nanotechnology,* vol. 21, no. 8, p. 085103, 2010.

[82] E. Porcel, S. Li, N. Usami, H. Remita, Y. Furusawa, K. Kobayashi, C. Le Sech and S. Lacombe, "Nano-sensitization under gamma rays and fast ion irradiation," *J Phys: Conf Ser,* vol. 373, p. 012006, 2012.

[83] L. Maggiorella, G. Barouch, C. Devaux, A. Pottier, E. Deutsch, J. Bourhis, E. Borghi and L. Levy, "Nanoscale radiotherapy with hafnium oxide nanoparticles," *Future Oncol,* vol. 8, no. 9, pp. 1167-1181, 2012.

[84] S.-J. Yu, M.-W. Kang, H.-C. Chang, K.-M. Chen and Y.-C. Yu, "Bright Fluorescent Nanodiamonds: No Photobleaching and Low Cytotoxicity," *J Am Chem Soc,* vol. 127, no. 50, pp. 17604-17605, 2005.

[85] Y. Chang, H. Lee, K. Chen, C. Chang, D. Tsai, C. Fu, T. Lim, Y. Tzeng, C. Fang, C. Han, H. Chang and W. Fann, "Mass production and dynamic imaging of fluorescent nanodiamonds," *Nature Nanotech,* vol. 3, no. 5, pp. 284-288, 2008.

[86] K. van der Laan, M. Hasani, T. Zheng and R. Schirhagl, "Nanodiamonds for In Vivo Applications," *Small,* vol. 14, no. 19, p. 1703838, 2018.

[87] R. Grall, H. Girard, L. Saad, T. Petit, C. Gesset, M. Combis-Schlumberger, V. Paget, J. Delic, J.-C. Arnault and S. Chevillard, "Impairing the radioresistance of cancer cells by hydrogenated nanodiamonds," *Biomaterials,* vol. 61, pp. 290-298, 2015.

[88] L. Tang, C. Tsai, W. Gerberich, L. Kruckeberg and D. Kania, "Biocompatibility of chemical-vapour-deposited diamond," *Biomaterials,* vol. 16, p. 483–488, 1995.

[89] G. Petrini, E. Moreva, E. Bernardi, P. Traina, G. Tomagra, V. Carabelli, I. Degiovanni and M. Genovese, "Is a Quantum Biosensing Revolution Approaching? Perspectives in NV-Assisted Current and Thermal Biosensing in Living Cells," *Adv Quantum Technol,* vol. 3, p. 2000066, 2020.

[90] J. Forneris, S. Ditalia Tchernij, P. Traina, E. Moreva, N. Skukan, M. Jakšić, V. Grilj, F. Bosia, E. Enrico, G. Amato, I. Degiovanni, B. Naydenov, F. Jelezko, M. Genovese and P. Olivero, "Mapping the Local Spatial Charge in Defective Diamond by Means of N-V Sensors—A Self-Diagnostic Concept," *Phys Rev Appl,* vol. 10, p. 014024, 2018.

[91] R. Sharmin, T. Hamoh, A. Sigaeva, A. Mzyk, V. Damle, A. Morita, T. Vedelaar and R. Schirhagl, "Fluorescent Nanodiamonds for Detecting Free-

Radical Generation in Real Time during Shear Stress in Human Umbilical Vein Endothelial Cells," *ACS Sensors*, vol. 6, pp. 4349-4359, 2021.

[92] L. Guarina, C. Calorio, D. Gavello, E. Moreva, P. Traina, A. Battiato, S. Tchernij, J. Forneris, M. Gai, F. Picollo, P. Olivero, M. Genovese, E. Carbone, A. Marcantoni and V. Carabelli, "Nanodiamonds-induced effects on neuronal firing of mouse hippocampal microcircuits," *Sci Rep*, vol. 8, p. 2221, 2018.

[93] G. Prestopino, M. Marinelli, E. Milani, C. Verona, G. Verona-Rinati, P. Traina, E. Moreva, I. Degiovanni, M. Genovese, S. Ditalia Tchernij, F. Picollo, P. Olivero and J. Forneris, "Photo-physical properties of He-related color centers in diamond," *Appl Phys Lett*, vol. 111, p. 111105, 2017.

[94] M. Nahra, D. Alshamaa, R. Deturche, V. Davydov, L. Kulikova, V. Agafonov and C. Couteau, "Single germanium vacancy centers in nanodiamonds with bulk-like spectral stability," *AVS Quantum Sci*, vol. 3, p. 012001, 2021.

[95] H. Pierson, in *Handbook of Carbon, Graphite, Diamond and Fullerenes. Processing, Properties and Applications*, Noyes Publications, 1994, p. 25–69.

[96] R. Nor, S. Abu Bakar, T. Thandavan and M. Rusop, "Diamond: Synthesis, Characterisation and Applications," in *Advanced Structured Materials*, vol. 5, Berlin Heidelberg, Springer-Verlag, 2010, p. 195–217.

[97] http://www.hk-phy.org/atomic_world/carbon/carbon01_e.html (accessed in January 2024).

[98] https://tex.stackexchange.com/questions/141363/draw-realistic-3d-crystal-structures-diamond (accessed in January 2024).

[99] https://qph.cf2.quoracdn.net/main-qimg-0a3f90f16e86d39b4db5a6bd8e35c708 (accessed in February 2024).

[100] J. Zazula, "On Graphite Transformations at High Temperature and Pressure Induced by Absorption of the LHC Beam," *LHC Project Note*, no. 78, 1997.

[101] M. Manutchehr-Danai, "Mohs' scale of hardness," in *Dictionary of Gems and Gemology*, Berlin Heidelberg, Springer, 2009, p. 578.

[102] C. Kittel, Introduzione alla fisica dello stato solido, Casa Editrice Ambrosiana, 2008.

[103] O. Auciello and D. Aslam, "Review on advances in microcrystalline, nanocrystalline and ultrananocrystalline diamond films-based micro/nano-

electromechanical systems technologies," *J Mater Sci,* vol. 56, p. 7171–7230, 2021.

[104] A. Zaitsev, Optical Properties of Diamond, Berlin Heidelberg: Springer, 2001.

[105] V. Danilenko, "On the history of the discovery of nanodiamond synthesis," *Phys Solid State,* vol. 46, p. 595–599, 2004.

[106] J.-P. Boudou, P. Curmi, F. Jelezko, J. Wrachtrup, P. Aubert, M. Sennour, G. Balasubramanian, R. Reuter, A. Thorel and E. Gaffet, "High yield fabrication of fluorescent nanodiamonds," *Nanotechnology,* vol. 20, p. 235602, 2009.

[107] V. Mochalin, O. Shenderova, D. Ho and Y. Gogotsi, "The properties and applications of nanodiamonds," *Nat Nanotechnol,* vol. 7, p. 11–23, 2012.

[108] J. Butler and H. Windischmann, "Developments in CVD-Diamond Synthesis During the Past Decade," *MRS Bull,* vol. 23, pp. 22-27, 1998.

[109] A. Datta, M. Kirca, Y. Fu and A. To, "Surface structure and properties of functionalized nanodiamonds: a first-principles study," *Nanotechnology,* vol. 22, p. 065706, 2011.

[110] K. Holt, "Diamond at the nanoscale: Applications of diamond nanoparticles from cellular biomarkers to quantum computing," *Philos Trans A Math Phys Eng Sci,* vol. 365, p. 2845–2861, 2007.

[111] M. Alkahtani, F. Alghannam, L. Jiang, A. Almethen, A. Rampersaud, R. Brick, C. Gomes, M. Scully and P. Hemmer, "Fluorescent nanodiamonds: past, present, and future," *Nanophotonics,* vol. 7, p. 1423–1453, 2018.

[112] I. Vlasov, A. Shiryaev, T. Rendler, S. Steinert, S.-Y. Lee, D. Antonov, M. Vörös, F. Jelezko, A. Fisenko, L. Semjonova, J. Biskupek, U. Kaiser, O. Lebedev, I. Sildos, P. Hemmer, V. Konov, A. Gali and J. Wrachtrup, "Molecular-sized fluorescent nanodiamonds," *Nat Nanotechnol,* vol. 9, no. 1, p. 54–58, 2014.

[113] A. Nagl, S. Hemelaar and R. Schirhagl, "Improving surface and defect center chemistry of fluorescent nanodiamonds for imaging purposes—a review," *Anal Bioanal Chem,* vol. 407, no. 25, p. 7521–7536, 2015.

[114] L. McGuinness, Y. Yan, A. Stacey, D. Simpson, L. Hall, D. Maclaurin, S. Prawer, P. Mulvaney, J. Wrachtrup, F. Caruso, R. Scholten and L. Hollenberg, "Quantum measurement and orientation tracking of fluorescent nanodiamonds inside living cells," *Nat Nanotechnol,* vol. 6, p. 358–363, 2011.

[115] Y. Hui, C.-L. Cheng and H.-C. Chang, “Nanodiamonds for optical bioimaging,” *J Phys D Appl Phys,* vol. 43, p. 374021, 2010.

[116] M. Chipaux, K. van der Laan, S. Hemelaar, M. Hasani, T. Zheng and R. Schirhagl, “Nanodiamonds and Their Applications in Cells,” *Small,* vol. 14, p. 1704263, 2018.

[117] F. Jelezko and J. Wrachtrup, “Single defect centres in diamond: A review,” *Phys Status Solidi Appl Mater Sci,* vol. 203, p. 3207–3225, 2006.

[118] J. Becker and E. Neu, “The silicon vacancy center in diamond,” in *Semiconductors and Semimetals*, Elsevier, 2020, p. 201–235.

[119] T. Iwasaki, F. Ishibashi, Y. Miyamoto, Y. Doi, S. Kobayashi, T. Miyazaki, K. Tahara, K. Jahnke, L. Rogers, B. Naydenov, F. Jelezko, S. Yamasaki, S. Nagamachi, T. Inubushi, N. Mizuochi and M. Hatano, “Germanium-Vacancy Single Color Centers in Diamond,” *Sci Rep*, vol. 5, p. 12882, 2015.

[120] T. Iwasaki, Y. Miyamoto, T. Taniguchi, P. Siyushev, M. Metsch, F. Jelezko and M. Hatano, “Tin-Vacancy Quantum Emitters in Diamond,” *Phys Rev Lett,* vol. 119, p. 253601, 2017.

[121] S. Ditalia Tchernij, T. Lühmann, T. Herzig, J. Küpper, A. Damin, S. Santonocito, M. Signorile, P. Traina, E. Moreva, F. Celegato, S. Pezzagna, I. Degiovanni, P. Olivero, M. Jakšić, J. Meijer, P. Genovese and J. Forneris, “Single-Photon Emitters in Lead-Implanted Single-Crystal Diamond,” *ACS Photonics,* vol. 5, no. 12, p. 4864–4871, 2018.

[122] F. Waldermann, P. Olivero, J. Nunn, K. Surmacz, Z. Wang, D. Jaksch, R. Taylor, I. Walmsley, M. Draganski, P. Reichart, A. Greentree, D. Jamieson and S. Prawer, “Creating diamond color centers for quantum optical applications,” *Diam Relat Mater,* vol. 16, no. 11, p. 1887–1895, 2007.

[123] M. Doherty, N. Manson, P. Delaney, F. Jelezko, J. Wrachtrup and L. Hollenberg, “The nitrogen-vacancy colour centre in diamond,” *Phys Rep*, vol. 528, pp. 1-45, 2013.

[124] J. Wrachtrup and F. Jelezko, “Processing quantum information in diamond,” *J Phys: Condens Matter,* vol. 18, no. 21, p. S807, 2006.

[125] S. Hemelaar, P. De Boer, M. Chipaux, W. Zuidema, T. Hamoh, F. Martinez, A. Nagl, J. Hoogenboom, B. Giepmans and R. Schirhagl, “Nanodiamonds as multi-purpose labels for microscopy,” *Sci Rep,* vol. 7, p. 720, 2017.

[126] R. Kaur and I. Badea, “Nanodiamonds as novel nanomaterials for biomedical applications: Drug delivery and imaging systems,” *Int J Nanomedicine,* vol. 8, p. 203–220, 2013.

[127] G. Petrini, G. Tomagra, E. Bernardi, E. Moreva, P. Traina, A. Marcantoni, F. Picollo, K. Kvaková, P. Cígler, I. Degiovanni, V. Carabelli and M. Genovese, "Nanodiamond–Quantum Sensors Reveal Temperature Variation Associated to Hippocampal Neurons Firing," *Adv Sci,* vol. 9, no. 28, p. 2202014, 2022.

[128] H. Jung and K. Neuman, "Surface Modification of Fluorescent Nanodiamonds for Biological Applications," *Nanomaterials,* vol. 11, p. 153, 2021.

[129] X. Zhang, J. Yin, C. Kang, J. Li, Y. Zhu, W. Li, Q. Huang and Z. Zhu, "Biodistribution and toxicity of nanodiamonds in mice after intratracheal instillation," *Toxicol Lett,* vol. 198, no. 2, p. 237–243, 2010.

[130] Y. Yuan, X. Wang, G. Jia, J.-H. Liu, T. Wang, Y. Gu, S.-T. Yang, S. Zhen, H. Wang and Y. Liu, "Pulmonary toxicity and translocation of nanodiamonds in mice," *Diam.Relat Mater,* vol. 19, no. 4, p. 291–299, 2010.

[131] X. Li, J. Shao, Y. Qin, C. Shao, T. Zheng and L. Ye, "TAT-conjugated nanodiamond for the enhanced delivery of doxorubicin," *J Mater Chem,* vol. 21, p. 7966–7973, 2011.

[132] V. Mochalin, A. Pentecost, X.-M. Li, I. Neitzel, M. Nelson, C. Wei, T. He, F. Guo and Y. Gogotsi, "Adsorption of drugs on nanodiamond: toward development of a drug delivery platform," *Mol Pharm,* vol. 10, p. 3728–3735, 2013.

[133] S. Chauhan, N. Jain and U. Nagaich, "Nanodiamonds with powerful ability for drug delivery and biomedical applications: recent updates on in vivo study and patents," *J Pharm Anal,* vol. 10, p. 1–12, 2020.

[134] J. Giammarco, V. Mochalin, J. Haeckel and Y. Gogotsi, "The adsorption of tetracycline and vancomycin onto nanodiamond with controlled release," *J Colloid Interface Sci,* vol. 468, p. 253–261, 2016.

[135] J. Nunes-Pereira, A. Silva, C. Ribeiro, S. Carabineiro, J. Buijnsters and S. Lanceros-Méndez, "Nanodia-monds/poly(vinylidene fluoride) composites for tissue engineering applications," *Compos Part B Eng,* vol. 111, p. 37–44, 2017.

[136] N. Prabhakar and J. Rosenholm, "Nanodiamonds for advanced optical bioimaging and beyond," *Curr Opin Colloid Interface Sci,* vol. 39, p. 220–231, 2019.

[137] M. Torelli, N. Nunn and O. Shenderova, "A perspective on fluorescent nanodiamond bioimaging," *Small,* vol. 15, p. 1902151, 2019.

[138] T. Huang, Y. Tzeng, Y. Liu, Y. Chen, K. Walker, R. Guntupalli and C. Liu, "Immobilization of antibodies and bacterial binding on nanodiamond and carbon nanotubes for biosensor applications," *Diam Relat Mater,* vol. 13, no. 4-8, pp. 1098-1102, 2004.

[139] F. Picollo, L. Mino, A. Battiato, S. Ditalia Tchernij, J. Forneris, K. Martina, M. Sacco, S. Tagliapietra, E. Vittone, P. Olivero and A. Barge, "Synthesis and characterization of porphyrin functionalized nanodiamonds," *Diam Relat Mater,* vol. 91, pp. 22-28, 2019.

[140] I. Chang, K. Hwang, J.-A. Ho, C.-C. Lin, R.-R. Hwu and J.-C. Horng, "Facile surface functionalization of nanodiamonds," *Langmuir,* vol. 26, no. 5, p. 3685–3689, 2010.

[141] V. Vaijayanthimala and H.-C. Chang, "Functionalized fluorescent nanodiamonds for biomedical applications," *Nanomedicine,* vol. 4, no. 1, p. 47–55, 2009.

[142] J. Garrido, "Bifunctionalization of Diamond Surfaces: Fundamentals and Applications," in *CVD Diamond for Electronic Devices and Sensors*, New York, Ricardo S. Sussmann, 2009, pp. 399-437.

[143] P.-H. Chung, E. Perevedentseva, J.-S. Tu, C. Chang and C.-L. Cheng, "Spectroscopic study of bio-functionalized nanodiamonds," *Diam Relat Mater,* vol. 15, p. 622–625, 2006.

[144] V. Merz, J. Lenhart, Y. Vonhausen, M. Ortiz-Soto, J. Seibel and A. Krueger, "Zwitterion-Functionalized Detonation Nanodiamond with Superior Protein Repulsion and Colloidal Stability in Physiological Media," *Small,* vol. 15, p. 1901551, 2019.

[145] T. Meinhardt, D. Lang, H. Dill and A. Krueger, "Pushing the Functionality of Diamond Nanoparticles to New Horizons: Orthogonally Functionalized Nanodiamond Using Click Chemistry," *Adv Funct Mater,* vol. 21, p. 494–500, 2011.

[146] P. Aprà, J. Ripoll-Sau, J. Manzano-Santamaría, C. Munuera, J. Forneris, S. Ditalia Tchernij, P. Olivero, F. Picollo, E. Vittone and M.-D. Ynsa, "Structural characterization of 8 MeV 11B implanted diamond," *Diamond and Related Materials,* vol. 104, no. 174, p. 107770, 2020.

[147] S. Sturari, V. Varzi, P. Aprà, A. Britel, N.-H. Amine, G. Andrini, E. Corte, G. Tomagra, L. Mino, P. Olivero and F. Picollo, "A comprehensive study of the effect of thermally induced surface terminations on nanodiamonds electrical properties," *Surf Interfaces,* vol. 38, p. 102831, 2023.

[148] J. Chen, S. Deng, J. Chen, Z. Yu and N. Xu, “Graphitization of nanodiamond powder annealed in argon ambient,” *Appl Phys Lett*, vol. 74, p. 3651–3653, 1999.

[149] A. Krueger and D. Lang, “Functionality is key: Recent progress in the surface modification of nanodiamond,” *Adv Funct Mater*, vol. 22, p. 890–906, 2012.

[150] S. Pezzagna, D. Rogalla, D. Wildanger, J. Meijer and A. Zaitsev, “Creation and nature of optical centres in diamond for single-photon emission—overview and critical remarks,” *New J Phys*, vol. 13, p. 035024, 2011.

[151] S. Osswald, G. Yushin, V. Mochalin, S. Kucheyev and Y. Gogotsi, “Control of sp 2 /sp 3 Carbon Ratio and Surface Chemistry of Nanodiamond Powders by Selective Oxidation in Air,” *J Am Chem Soc*, vol. 128, p. 11635–11642, 2006.

[152] O. Shenderova, A. Koscheev, N. Zaripov, I. Petrov, Y. Skryabin, P. Detkov, S. Turner and G. Van Tendeloo, “Surface Chemistry and Properties of Ozone-Purified Detonation Nanodiamonds,” *J Phys Chem C*, vol. 115, p. 9827–9837, 2011.

[153] S. Stehlik, M. Varga, M. Ledinsky, V. Jirasek, A. Artemenko, H. Kozak, L. Ondic, V. Skakalova, G. Argentero, T. Pennycook, J. Meyer, A. Fejfar, A. Kromka and B. Rezek, “Size and Purity Control of HPHT Nanodiamonds down to 1 nm,” *J Phys Chem C*, vol. 119, no. 49, p. 27708–27720, 2015.

[154] G. Jarre, S. Heyer, E. Memmel, T. Meinhardt and A. Krueger, “Synthesis of nanodiamond derivatives carrying amino functions and quantification by a modified Kaiser test,” *Beilstein J Org Chem*, vol. 10, p. 2729–2737, 2014.

[155] N. Xu, J. Chen and S. Deng, “Effect of heat treatment on the properties of nano-diamond under oxygen and argon ambient,” *Diam Relat Mater*, vol. 11, p. 249–256, 2002.

[156] A. Krueger, “New Carbon Materials: Biological Applications of Functionalized Nanodiamond Materials,” *Chem - A Eur J*, vol. 14, p. 1382–1390, 2008.

[157] L. Ginés, S. Mandal, Ashek-I-Ahmed, C.-L. Cheng, M. Sowc and O. Williams, “Positive zeta potential of nanodiamonds,” *Nanoscale*, vol. 9, no. 34, p. 12549–12555, 2017.

[158] T. Kondo, I. Neitzel, V. Mochalin, J. Urai, M. Yuasa and Y. Gogotsi, “Electrical conductivity of thermally hydrogenated nanodiamond powders,” *J Appl Phys*, vol. 113, no. 21, p. 214307, 2013.

[159] O. Williams, J. Hees, C. Dieker, W. Jäger, L. Kirste and C. Nebel, "Size-dependent reactivity of diamond nanoparticles," *ACS Nano,* vol. 4, no. 8, pp. 4824-4830, 2010.

[160] S. Stehlik, T. Glatzel, V. Pichot, R. Pawlak, E. Meyer, D. Spitzer and B. Rezek, "Water interaction with hydrogenated and oxidized detonation nanodiamonds-Microscopic and spectroscopic analyses," *Diam Relat Mater,* vol. 63, p. 97–102, 2016.

[161] L. Ostrovskaya, V. Perevertailo, V. Ralchenko, A. Dementjev and O. Loginova, "Wettability and surface energy of oxidized and hydrogen plasma-treated diamond films," *Diam Relat Mater,* vol. 11, p. 845–850, 2002.

[162] F. Maier, J. Ristein and L. Ley, "Electron affinity of plasma-hydrogenated and chemically oxidized diamond (100) surfaces," *Phys Rev B - Condens Matter Mater Phys,* vol. 64, pp. 1-7, 2001.

[163] J. Ristein, "Diamond surfaces: Familiar and amazing," *Appl Phys A Mater Sci Process,* vol. 82, p. 377–384, 2006.

[164] J. Ristein, "The Physics of Hydrogen-Terminated Diamond Surfaces," *AIP Conf. Proc.,* vol. 772, no. 1, p. 377–380, 2005.

[165] F. Maier, M. Riedel, B. Mantel, J. Ristein and L. Ley, "Origin of Surface Conductivity in Diamond," *Phys Rev Lett,* vol. 85, p. 3472–3475, 2000.

[166] V. Seshan, D. Ullien, A. Castellanos-Gomez, S. Sachdeva, D. Murthy, T. Savenije, H. Ahmad, T. Nunney, S. Janssens, K. Haenen, M. Nesládek, H. van der Zant, E. Sudhölter and L. de Smet, "Hydrogen termination of CVD diamond films by high-temperature annealing at atmospheric pressure," *J Chem Phys,* vol. 138, no. 23, p. 234707, 2013.

[167] T. Petit, H. Girard, M. Combis-Schlumberger, R. Grall, J. Delic, S. Morel-Altmeyer, P. Bergonzo, S. Chevillard and J. Arnault, "Nanodiamond as a multimodal platform for drug delivery and radiosensitization of tumor cells," in *Proceedings of the 13th IEEE Conference on Nanotechnology*, pp. 174–178; Beijing, China, 2013.

[168] M. Kurzyp, H. Girard, Y. Cheref, E. Brun, C. Sicard-Roselli, S. Saada and J. Arnault, "Hydroxyl radical production induced by plasma hydrogenated nanodiamonds under X-ray irradiation," *Chem Commun,* vol. 53, p. 1237–1240, 2017.

[169] P. Aprà, L. Mino, A. Battiato, P. Olivero, S. Sturari, M. Valsania, V. Varzi and F. Picollo, "Interaction of Nanodiamonds with Water: Impact of Surface Chemistry on Hydrophilicity, Aggregation and Electrical Properties," *Nanomaterials,* vol. 11, p. 2740, 2021.

[170] L. Mino, E. Borfecchia, A. Agostino, C. Lamberti and M. Truccato, "Oxygen doping tuning in superconducting oxides by thermal annealing and hard X-ray irradiation," *J Electron Spectros Relat Phenom,* vol. 220, pp. 69-75, 2017.

[171] A. Tyurnina, I. Apolonskaya, I. Kulakova, P. Kopylov and A. Obraztsov, "Thermal purification of detonation diamond," *J Surf Investig X-ray, Synchrotron Neutron Tech,* vol. 4, p. 458–463, 2010.

[172] S. Stelmakh, K. Skrobas, S. Gierlotka and B. Palosz, "Atomic structure of nanodiamond and its evolution upon annealing up to 1200 °C: Real space neutron diffraction analysis supported by MD simulations," *Diam Relat Mater,* vol. 93, p. 139–149, 2019.

[173] D. Titus, E. James Jebaseelan Samuel and S. Roopan, "Nanoparticle characterization techniques," in *Green Synthesis, Characterization and Applications of Nanoparticles,* Elsevier, 2019, p. 303–319.

[174] "Optical Characterization," in *Semiconductor Material and Device Characterization,* John Wiley & Sons, Inc., 2005, p. 563–626.

[175] A. Cantarero, "Raman Scattering Applied to Materials Science," *Procedia Mater Sci,* vol. 9, p. 113–122, 2015.

[176] J. Smit, "Theory of Raman Scattering in Solids," *Phys Rev B,* vol. 3, p. 4330–4337, 1971.

[177] D. Wolverson, "Raman Spectroscopy," in *An Introduction to Laser Spectroscopy,* Springer US, 1995, p. 91–114.

[178] https://warwick.ac.uk/fac/cross_fac/sciencecity/programmes/internal/themes/am2/booking/particlesize/intro_to_dls.pdf (accessed in February 2024).

[179] W. Goldburg, "Dynamic light scattering," *Am J Phys,* vol. 67, p. 1152–1160, 1999.

[180] R. Pecora, "Dynamic Light Scattering Measurement of Nanometer Particles in Liquids," *J Nanoparticle Res,* vol. 2, p. 123–131, 2000.

[181] https://creativecommons.org/licenses/by-sa/3.0/ (accessed in February 2024).

[182] H.-A. Kim, J.-K. Seo, T. Kim and B.-T. Lee, "Nanometrology and its perspectives in environmental research," *Environ Health Toxicol,* vol. 29, 2014.

[183] R. Smith, K. Baker and P. Dustan, “Fluorometric techniques for the measurement of oceanic chlorophyll in the support of remote sensing,” *Scripps Institution of Oceanography,* 1981.

[184] J. Lakowicz, Principles of fluorescence spectroscopy, Springer Science & Business Media, 2013.

[185] P. So and C. Dong, “Fluorescence spectrophotometry,” *eLS,* 2002.

[186] S. Page, W. Arnold and K. McNeill, “Terephthalate as a probe for photochemically generated hydroxyl radical,” *J Environ Monit,* vol. 12, no. 9, p. 1658–1665, 2010.

[187] I. Šnyrychová and É. Hideg, “The first application of terephthalate fluorescence for highly selective detection of hydroxyl radicals in thylakoid membranes,” *Functional Plant Biology,* vol. 34, no. 12, p. 1105–1111, 2008.

[188] W. Freinbichler, L. Bianchi, M. Colivicchi, C. Ballini, K. Tipton, W. Linert and L. Della Corte, “The detection of hydroxyl radicals in vivo,” *J Inorg Biochem,* vol. 102, no. 5-6, pp. 1329-1333, 2008.

[189] https://elearning.unipd.it/flowinlab/mod/page/view.php?id=12 (accessed in January 2024).

[190] J. Wang, Y. Zhan, N. Bao and C. Lu, “Quantitative measurement of quantum dot uptake at the cell population level using microfluidic evanescent-wave-based flow cytometry,” *Lab Chip,* vol. 12, p. 1441–1445, 2012.

[191] J. Kim, C. Åberg, A. Salvati and K. Dawson, “Role of cell cycle on the cellular uptake and dilution of nanoparticles in a cell population,” *Nat Nanotechnol,* vol. 7, p. 62–68, 2012.

[192] T.-L. Wee, Y.-W. Mau, C.-Y. Fang, H.-L. Hsu, C.-C. Han and H.-C. Chang, “Preparation and characterization of green fluorescent nanodiamonds for biological applications,” *Diam Relat Mater,* vol. 18, p. 567–573, 2009.

[193] Z. Lien, T. Hsu, K. Liu, W. Liao, K. Hwang and J. Chao, “Cancer cell labeling and tracking using fluorescent and magnetic nanodiamond,” *Biomaterials,* vol. 33, p. 6172–6185, 2012.

[194] S. Baccaro, A. Cemmi, I. Di Sarcina and G. Ferrara, “Gamma Irradiation Calliope Facility at ENEA - Casaccia Research Centre: Rome, Italy,” in *ENEA Technical Report; RT/2019/4/ENEA; Fusion and Technology for Nuclear Safety and Security Department Casaccia Research Centre: Rome, Italy; ISSN 0393-3016,* 2019.

[195] T. Mahmood and P.-C. Yang, “Western Blot: Technique, Theory, and Trouble Shooting,” *N Am J Med Sci,* vol. 4, no. 9, pp. 429-434, 2012.

[196] I. Artika, Y. Dewi, I. Nainggolan, J. Siregar and U. Antonjaya, “Real-Time Polymerase Chain Reaction: Current Techniques, Applications, and Role in COVID-19 Diagnosis,” *Genes (Basel),* vol. 13, no. 12, p. 2387, 2022.

[197] T. Petit and L. Puskar, “FTIR spectroscopy of nanodiamonds: Methods and interpretation,” *Diam Relat Mater,* vol. 89, p. 52–66, 2018.

[198] S. Ji, T. Jiang, K. Xu and S. Li, “FTIR study of the adsorption of water on ultradispersed diamond powder surface,” *Appl Surf Sci,* vol. 133, p. 231–238, 1998.

[199] L. Mino, C. Negri, A. Zecchina and G. Spoto, “Photodegradation of Organic Pollutants on TiO2 P25 Surfaces Investigated by Transmission FTIR Spectroscopy Under In Situ UV-Vis Irradiation,” *Zeitschrift für Phys Chemie,* vol. 230, 2016.

[200] M. Acik, G. Lee, C. Mattevi, A. Pirkle, R. Wallace, M. Chhowalla, K. Cho and Y. Chabal, “The Role of Oxygen during Thermal Reduction of Graphene Oxide Studied by Infrared Absorption Spectroscopy,” *J Phys Chem C,* vol. 115, p. 19761–19781, 2011.

[201] V. Varzi, E. Fratini, M. Falconieri, D. Giovannini, A. Cemmi, J. Scifo, I. Di Sarcina, P. Aprà, S. Sturari, L. Mino, G. Tomagra, E. Infusino, V. Landoni, C. Marino, M. Mancuso, F. Picollo and S. Pazzaglia, “Nanodiamond Effects on Cancer Cell Radiosensitivity: The Interplay between Their Chemical/Physical Characteristics and the Irradiation Energy,” *Int J Mol Sci,* vol. 24, p. 16622, 2023.

[203] E. Brun, H. Girard, J.-C. Arnault, M. Mermoux and C. Sicard-Roselli, “Hydrogen plasma treated nanodiamonds lead to an overproduction of hydroxil radicals and solvayed electronsinsolution under ionizing radiation,” *Carbon,* vol. 162, pp. 510-518, 2020.

[204] T. Petit, H. Girard, A. Trouvé, I. Batonneau-Gener, P. Bergonzo and J.-C. Arnault, “Surface transfer doping can mediate both colloidal stability and self-assembly of nanodiamonds,” *Nanoscale,* vol. 5, p. 8958–8962, 2013.

[205] T. Petit, L. Puskar, T. Dolenko, S. Choudhury, E. Ritter, S. Burikov, K. Laptinskiy, Q. Brzustowski, U. Schade, H. Yuzawa, M. Nagasaka, N. Kosugi, M. Kurzyp, A. Venerosy, H. Girard, J.-C. Arnault, E. Osawa, N. Nunn, O. Shenderova and E. Aziz, “Unusual water hydrogen bond network around hydrogenated nanodiamonds,” *J Phys Chem C,* vol. 121, p. 5185–5194, 2017.

[206] C. Fu, H. Lee, K. Chen, T. Lim, H. Wu, P. Lin, P. Wei, P. Tsao, H. Chang and W. Fann, "Characterization and application of single fluorescent nanodiamonds as cellular biomarkers," *Proc. Natl. Acad. Sci. USA,* vol. 104, p. 727–732, 2007.

[207] B. Wójcik, K. Zawadzka, S. Jaworski, M. Kutwin, M. Sosnowska, A. Ostrowska, M. Grodzik, A. Małolepszy, M. Mazurkiewicz-Pawlicka and M. Wierzbicki, "Dependence of diamond nanoparticle cytotoxicity on physicochemical parameters: Comparative studies of glioblastoma, breast cancer, and hepatocellular carcinoma cell lines.," *Nanotoxicology,* vol. 17, p. 310–337, 2023.

[208] R. Popescu, D. Savu, I. Dorobantu, B. Vasile, H. Hosser, A. Boldeiu, M. Temelie, M. Straticiuc, D. Iancu, E. Andronescu, F. Wenz, F. Giordano, C. Herskind and M. Veldwijk, "Efficient uptake and retention of iron oxide-based nanoparticles in HeLa cells leads to an effective intracellular delivery of doxorubicin," *Sci Rep,* vol. 10, p. 10530, 2020.

[209] D. Chithrani, S. Jelveh, F. Jalali, M. van Prooijen, C. Allen, R. Bristow, R. Hill and D. Jaffray, "Gold Nanoparticles as Radiation Sensitizers in Cancer Therapy," *Radiat. Res.,* vol. 173, p. 719–728, 2010.

[210] J. Jeevanandam, A. Barhoum, Y. Chan, A. Dufresne and M. Danquah, "Review on Nanoparticles and Nanostructured Materials: History, Sources, Toxicity and Regulations," *Beilstein J. Nanotechnol.,* vol. 9, p. 1050–1074, 2018.

[211] P. Mowat, A. Mignot, W. Rima, F. Lux, O. Tillement, C. Roulin, M. Dutreix, D. Bechet, S. Huger, L. Humbert, M. Barberi-Heyob, M. Aloy, E. Armandy, C. Rodriguez-Lafrasse, G. Le Duc, S. Roux and P. Perriat, "In vitro radiosensitizing effects of ultrasmall gadolinium based particles on tumour cells," *J. Nanosci. Nanotechnol.,* vol. 11, pp. 7833-7839, 2011.

[212] I. Miladi, M. Aloy, E. Armandy, P. Mowat, D. Kryza, N. Magné, O. Tillement, F. Lux, C. Billotey, M. Janier and C. Rodriguez-Lafrasse, "Combining ultrasmall gadolinium-based nanoparticles with photon irradiation overcomes radioresistance of head and neck squamous cell carcinoma," *Nanomedicine,* vol. 11, pp. 247-257, 2015.

[213] L. Štefančíková, S. Lacombe, D. Salado, E. Porcel, E. Pagáčová, O. Tillement, F. Lux, D. Depeš, S. Kozubek and M. Falk, "Effect of gadolinium-based nanoparticles on nuclear DNA damage and repair in glioblastoma tumor cells," *J. Nanobiotechnology,* vol. 14, p. 63, 2016.

[214] X. Chen, H. Wang, H. Wang, Y. Fu, J. Liu and R. Liu, "The Radiosensitizing Effect of Nanodiamonds (NDs) on HeLa Cells Under X-Ray Irradiation," *Phys. Status Solidi A,* vol. 215, p. 1700715, 2018.

[215] X. Huang, Y. Zhang, Y. Tang, N. Butler, J. Kim, F. Guessous, D. Schiff, J. Mandell and R. Abounader, "A novel PTEN/mutant p53/c-Myc/Bcl-XL axis mediates context-dependent oncogenic effects of PTEN with implications for cancer prognosis and therapy," *Neoplasia,* vol. 15, pp. 952-965, 2013.

[216] X. Kong, D. Yu, Z. Wang and S. Li, "Relationship between p53 status and the bioeffect of ionizing radiation," *Oncol Lett,* vol. 22, p. 661, 2021.

[217] H.-K. Shu, M. Kim, P. Chen, F. Furman, C. Julin and M. Israel, "The intrinsic radioresistance of glioblastoma-derived cell lines is associated with a failure of p53 to induce p21BAX expression," *Proc Natl Acad Sci USA,* vol. 95, p. 14453–14458, 1998.

[218] X. Cao, P. Wen, Y. Fu, Y. Gao, X. Qi, B. Chen, Y. Tao, L. Wu, A. Xu, H. Lu and G. Zhao, "Radiation induced apoptosis through the intrinsic pathway in mammalian cells," *Cell Signal,* vol. 62, p. 109337, 2019.

[219] E. Escobar-Chaves, S. Acin, D. Muñoz, M. Fernández, A. Echeverri, F. Echeverri, J. Orozco and N. Balcázar, "Polymeric nanoformulation prototype based on a natural extract for the potential treatment of type 2 diabetes mellitus," *Journal of Drug Delivery Science and Technology,* vol. 81, p. 104264, 2023.

[220] S. Fan, L. Nie, Y. Zhang, E. Ustyantseva, W. Woudstra, H. Kampinga and R. Schirhagl, "Diamond Quantum Sensing Revealing the Relation between Free Radicals and Huntington's Disease," *ACS Cent Sci,* vol. 9, no. 7, pp. 1427-1436, 2023.

[221] G. Tomagra, G. Peroni, P. Aprà, V. Bonino, M. Campostrini, V. Carabelli, C. Collà Ruvolo, A. Lo Giudice, L. Guidorzi, L. Mino, P. Olivero, L. Pacher, F. Picariello, A. Re, V. Rigato, M. Truccato, V. Varzi, E. Vittone and F. Picollo, "Diamond-based sensors for in vitro cellular radiobiology: Simultaneous detection of cell exocytic activity and ionizing radiation," *Biosensors and Bioelectronics,* vol. 220, p. 114876, 2023.

[222] G. Tomagra, C. Franchino, A. Pasquarelli, E. Carbone, P. Olivero, V. Carabelli and F. Picollo, "Simultaneous multisite detection of quantal release from PC12 cells using micro graphitic-diamond multi electrode arrays," *Biophys Chem,* vol. 253, p. 106241, 2019.

[223] G. Tomagra, A. Re, V. Varzi, P. Aprà, A. Britel, C. Franchino, S. Sturari, N.-H. Amine, R. Westerink, V. Carabelli and F. Picollo, "Enhancing the Study of Quantal Exocytotic Events: Combining Diamond Multi-Electrode Arrays with Amperometric Peak Analysis (APE) an Automated Analysis Code," *Biosensors,* vol. 13, p. 1033, 2023.

# Publications

**ISI publications**

- P. Aprà, L. Mino, A. Battiato, P. Olivero, S. Sturari, MC. Valsania, V. Varzi, F. Picollo. "Interaction of Nanodiamonds with Water: Impact of Surface Chemistry on Hydrophilicity, Aggregation and Electrical Properties", Nanomaterials (2021), 11(10):2740.
- G. Tomagra, G. Peroni, P. Aprà, V. Bonino, M. Campostrini, V. Carabelli, C. Collà Ruvolo, A. Lo Giudice, L. Guidorzi, L. Mino, P. Olivero, L. Pacher, F. Picariello, A. Re, V. Rigato, M. Truccato, V. Varzi, E. Vittone, F. Picollo. "Diamond-based sensors for in vitro cellular radiobiology: Simultaneous detection of cell exocytic activity and ionizing radiation", Biosensors and Bioelectronics (2023), 220, 114876.
- S. Sturari, V. Varzi, P. Aprà, A. Britel, N.-H. Amine, E. Corte, G. Tomagra, L. Mino, P. Olivero, F. Picollo. "A comprehensive study of the effect of thermally induced surface terminations on nanodiamonds electrical properties", Surfaces and Interfaces (2023), 38, 102831.
- V. Varzi, E. Fratini, M. Falconieri, D. Giovannini, A. Cemmi, J. Scifo, I. Di Sarcina, P. Aprà, S. Sturari, L. Mino, G. Tomagra, E. Infusino, V. Landoni, C. Marino, M. Mancuso, F. Picollo, S. Pazzaglia. "Nanodiamonds Effects on Cancer Cell Radiosensitivity: The Interplay between Their Chemical/Physical Characteristics and the Irradiation Energy", Int. J. Mol. Sci. (2023), 24, 16622.
- G. Tomagra, A. Re, V. Varzi, P. Aprà, A. Britel, C. Franchino, S. Sturari, N.-H. Amine, R.H.S. Westerink, V. Carabelli, F. Picollo. "Enhancing the Study of Quantal Exocytotic Events: Combining

Diamond Multi-Electrode Arrays with Amperometric Peak Analysis (APE) an Automated Analysis Code", Biosensors (2023), 13, 1033.

- A. Britel, G. Tomagra, P. Aprà, V. Varzi, S. Sturari, N.-H. Amine, P. Olivero, F. Picollo. "3D Printing in Microfluidics: Experimental Optimization of Droplet Size and Generation Time through Flow Focusing, Phase, and Geometry Variation", RSC Advances (2024), 14, 7770.

**Other publications**

- S. Ditalia Tchernij, G. Andrini, P. Aprà, M. Campostrini, D. Carlucci, E. Corte, I. Degiovanni, M. Genovese, L. La Torre, C. Marinelli, E. Moreva, V. Prestopino, V. Rigato, P. Traina, V. Varzi, G. Verona, C. Verona Rinati, P. Olivero, J. Forneris, F. Picollo. "Ion Beam Fabrication of Graphitic Structures in Single-Crystal Diamond for Electrically-Stimulated Luminescence", LNL Annual Report 2020 (2021), 79.
- G. Zannelli, G. Andrini, P. Aprà, A. Britel, M. Campostrini, D. Carlucci, E. Corte, I. Degiovanni, M. Genovese, L. La Torre, E. Moreva, E. Nieto Hernàndez, V. Rigato, S. Sturari, P. Traina, V. Varzi, P. Olivero, J. Forneris, F. Picollo, S. Ditalia Tchernij. "Optical characterization of MeV He-implanted SiC upon laser annealing treatment", LNL Annual Report 2021 (2022), 74.
- S. Sturari, V. Varzi, P. Aprà, G. Tomagra, V. Monti, V. Bincoletto, B. Zurletti, E.A. Durisi, S. Arpicco, C. Riganti, P. Olivero, F. Picollo. "Functionalization of nanodiamonds with hyaluronic acid: a study for their potential applications in radiosensitization and selective tumor detection", European Journal of Histochemistry 2023 (Proceedings of the workshop NANO23@uniVR, 2023), 67(s1), 17.

# Ringraziamenti / Acknowledgments

Vorrei ringraziare tutte le persone che hanno condiviso con me questi anni.

Ringrazio sinceramente tutti i membri del gruppo di Fisica dello Stato Solido dell'Università di Torino e in particolare il mio tutor neo-Prof. Federico Picollo, che ha avuto la pazienza di motivare e supportare il mio percorso di crescita in ambito accademico (e penso anche come persona) a partire dalla tesi magistrale fino ad oggi, nonostante le difficoltà di alcuni periodi dell'attività di ricerca. Un grazie speciale alla Dott.ssa Giulia Tomagra, al Dott. Pietro Aprà e alla Dott.ssa Sofia Sturari per il loro prezioso e instancabile aiuto, dal punto di vista scientifico e morale, dimostrato in un profondo clima di amicizia. Ringrazio anche il Dott. Lorenzo Mino per la sua utilissima assistenza e i preziosi consigli. Insieme formiamo davvero un team che Fa Brillare la Ricerca!

I want to thank Dr. Adam Britel and Dr. Nour-Hanne Amine for enriching the group, bringing new skills and research topics to work on.

Ringrazio la mia tutor Dott.ssa Simonetta Pazzaglia per avermi seguito con grande pazienza e disponibilità, guidandomi passo dopo passo nella comprensione e nello sviluppo della parte legata agli esperimenti biologici del lavoro. Grazie per gli utilissimi consigli, lavorativi e non, e per la capacità di spronarmi a fare sempre del mio meglio. Ringrazio davvero di cuore tutte le persone che ho conosciuto presso il laboratorio ENEA Casaccia TEB e più in generale la divisione TECS, in primis la Dott.ssa Mariateresa Mancuso. Mi avete fatto sempre sentire come a casa. Vorrei nominarvi tutti, ma dato che la lista sarebbe molto lunga, vi porto sempre nei miei pensieri e qui cito in

particolare chi ha lavorato più a stretto contatto con me. Un grazie sincero al Dott. Emiliano Fratini per avermi insegnato tanto sul mondo degli esperimenti *in vitro* e per aver risposto sempre alle mie domande, mettendomi costantemente e pazientemente a disposizione le sue conoscenze. Grazie alla Dott. Daniela Giovannini per tutto il tempo speso in spiegazioni e confronti, grazie ai dubbi comuni sono riuscita a capire più a fondo le cose.

Grazie alla Dott.ssa Carmela Marino che ha creduto in questo progetto di collaborazione ENEA-UNITO e a Marina Funari per il modo sempre gentile di offrire aiuto per le questioni burocratiche.

Grazie al laboratorio ENEA TECFIS, con il Dott. Mauro Falconieri, la Dott.ssa Serena Gagliardi e la Dott.ssa Flaminia Rondino, per tutto l'aiuto e il supporto per le misure Raman, nonostante le numerose avversità implicite dell'attività sperimentale.

Grazie a tutta la facility ENEA Calliope e alla Dott.ssa Valeria Landoni e alla Dott.ssa Erminia Infusino per il supporto negli esperimenti di irraggiamento e la grande disponibilità dimostrata.

I thank Prof. Romana Schirhagl for the hospitality at her laboratories and in particular Dr. Elkin Escobar-Chaves who followed me during the period at the University Medical Center of Groningen.

I am really grateful for the opportunity I had in these years to work in different places and with so many people, I sincerely think that this made me a better scientist and most of all a better person, improving my spirit of adaptation. All contributed to increase the confidence in myself and in my work.

I want to acknowledge Prof. Martin Falk and Dr. Andrea Candini for having red and evaluated my thesis work.

Infine, un enorme grazie alla mia famiglia, che mi ha aiutato e incoraggiato continuamente da sempre. Mamma, papà, nonni, zie e cugini tutti.

Un grazie anche agli amici.

Grazie Luisa, perché anche se non è sempre facile sentirsi e stare dietro a tutto, trovi comunque tempo per me e i miei problemi, ma soprattutto per condividere i momenti belli insieme.

Grazie Erika, Giulia, Miky e Raffa, perché anche se distanti non ci siamo perse mai di vista e perché mi incoraggiate sempre con la vostra positività e i vostri complimenti.

Grazie agli amici di Occimiano e dintorni che con le uscite nei weekend portano sempre un po' di spensieratezza nei giorni difficili.

Grazie Ary per la tua sincerità e i momenti di confronto che ci hanno fatto crescere insieme.

Grazie Pino e Rosella, con voi al mio fianco la lontananza da casa è stata molto più lieve da sopportare e sono davvero felice del rapporto di sincera amicizia che si è creato.

Grazie Noemi e Gabriele, il vostro aiuto e la vostra vicinanza sono stati fondamentali, con tanti buoni consigli e la vostra disponibilità, non vedo l'ora di farmi di nuovo una bella camminata ad Anguillara con voi, questa volta anche con Daniele.

Ultimo, ma per scelta (dulcis in fundo), grazie Dani. Mi hai conosciuto in uno dei momenti più difficili per me, fatto di scelte, dubbi e indecisioni. So che non sarà l'ultimo di questi momenti perché, come mi insegni, la vita è fatta di scelte. Nonostante tutto però non mi hai mai lasciata allontanare, anzi mi hai letteralmente seguito per mezzo mondo. Siamo cresciuti e stiamo crescendo insieme. "Menomale" che ci sei, sempre.